

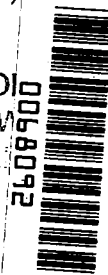
**NASA TECHNICAL  
REPORT**



**NASA TR R-165**

**NASA TR R-165**

C.1  
LOAN CO  
AFW  
KIRTLA



TECH LIBRARY KAFB, NM

URN TO  
SUL  
EX

**WALL-PRESSURE FLUCTUATIONS AND  
PRESSURE-VELOCITY CORRELATIONS  
IN A TURBULENT BOUNDARY LAYER**

*by John S. Serafini*

*Lewis Research Center*

*Cleveland, Ohio*



**WALL-PRESSURE FLUCTUATIONS AND PRESSURE-VELOCITY  
CORRELATIONS IN A TURBULENT BOUNDARY LAYER**

**By John S. Serafini**

**Lewis Research Center  
Cleveland, Ohio**

**NATIONAL AERONAUTICS AND SPACE ADMINISTRATION**

---

**For sale by the Office of Technical Services, Department of Commerce,  
Washington, D.C. 20230 -- Price \$2.00**

WALL-PRESSURE FLUCTUATIONS AND PRESSURE-VELOCITY  
CORRELATIONS IN A TURBULENT BOUNDARY LAYER<sup>1</sup>

by John S. Serafini

Lewis Research Center

SUMMARY

Pressure fluctuations of a turbulent layer along a plane boundary have been investigated experimentally. All measurements were made at a nominal free-stream Mach number of 0.6 and an average Reynolds number per foot of  $3.45 \times 10^6$  in a wind-tunnel facility specially designed for the purpose. The pressure fluctuations were measured with miniature pressure transducers and the velocity fluctuations with hot-wire anemometers.

The root-mean-square magnitudes of the wall-pressure fluctuations agree with the Lilley-Hodgson theoretical results, whereas the mean-square spectra do not agree except over a small range of frequencies. Space-time correlations of the wall-pressure fluctuations generally agree with Willmarth's experimental results for longitudinal separation distances. Measurements of lateral space-time correlations indicated that the ratio of the longitudinal to lateral length-scale is approximately 7.4. The convection velocity of the fluctuations is found to increase with increasing separation distances and its significance is explained.

Measurements of the correlations of the wall-pressure fluctuations with the longitudinal component of the velocity fluctuations indicate that the contributions to the wall-pressure fluctuations are from two regions, an inner region near the wall and an outer region linked with the intermittency.

INTRODUCTION

In the past, research on turbulent flows has been mainly concerned with the description of velocity fields of particular turbulent flows. Only in recent years has some interest been shown in determining the characteristics of pressure fluctuations associated with turbulence. This increased interest in the characteristics of fluctuating pressures resulted from major engineering problems

---

<sup>1</sup>Information presented herein was offered as a thesis in partial fulfillment of the requirements for the degree of Doctor of Philosophy to Case Institute of Technology, Cleveland, Ohio, June 1962.

created by high levels of aerodynamic noise from powerful jet engines and high-speed aircraft. Even though the research aim has been the phenomenological description of turbulent flows to calculate the radiated noise, the study of the pressure fluctuations and their relation to the turbulent velocities is fundamental. Such is the case for turbulent flow fields exhibiting a mean shear and exposed to bounding surfaces, for example, the turbulent plane wall boundary layer.

The first definitive works on the general problem of aerodynamic noise generated by a fluctuating velocity field without confining boundaries are the two classical theoretical papers by Lighthill (refs. 1 and 2). In the first of these papers the problem was formulated in terms of a nonhomogeneous wave equation for the noise in which the nonhomogeneous term was approximated by a fluctuating stress tensor having nonzero values within the confines of the disturbed flow field. The work by Lighthill stimulated a series of papers based on his theory that studied the aerodynamic noise generated by particular turbulent flows (refs. 3 to 11). All these papers are concerned with the aerodynamic noise radiated from a turbulent region of flow.

The determination of pressure fluctuations intrinsic to a turbulent field requires only that the basic equations of motion and continuity be satisfied for a fluid assumed to be incompressible and Stokesian. Heisenberg (ref. 12) and Batchelor (ref. 13) considered the pressure fluctuations from homogeneous, isotropic turbulence. Kraichnan (ref. 14) determined the fluctuating pressure field within homogeneous anisotropic turbulence. The first attempt to determine the wall-pressure fluctuations for a turbulent-boundary-layer flow over a plane boundary was by Kraichnan (ref. 15). A mirror flow model about the plane boundary was used, and Fourier transform techniques were applied to obtain a solution of the Poisson's equation for the pressure fluctuations at the specified boundary. While the idealized boundary-layer flow does not correspond to the characteristics of an actual turbulent boundary layer, the analysis along with dimensional arguments gives results for the mean-square pressure-fluctuation magnitude and spectrum. In particular, Kraichnan showed that  $\sqrt{p_w^2}/q_\infty \approx \beta c_f$  where  $\beta$  is a factor between 2 and 12. (Symbols are defined in appendix A.)

Lilley and Hodgson (ref. 16) used an analysis similar in method to that of Kraichnan (ref. 15) but depending on a slightly different model. An approximate theory is presented for the wall-pressure fluctuations for a turbulent boundary layer. In a subsequent paper Lilley (ref. 17) presents a more exact analysis resulting in  $\sqrt{p_w^2}/q_\infty \approx 3.1 c_f$ .

The experimental work on the characteristics of pressure fluctuations in turbulent flows has been limited to measurements at the surface of pipe walls or wind-tunnel walls. Measurements were obtained in reference 18 of the magnitude and spectral density of the wall-pressure fluctuations at velocities between 50 and 200 feet per second. Although this work was limited as to the ambient noise level in the wind-tunnel facility and type of pressure transducer used, a value of 0.8 was determined for the effective convective velocity of the pressure fluctuations divided by the free-stream velocity.

Willmarth (ref. 19) has made measurements with an improved pressure transducer of the wall-pressure fluctuations associated with turbulent boundary layers within a pipe. The results include the magnitude and spectra of the wall-pressure fluctuations presented in dimensionless form. The space-time correlations confirmed the existence of the convective pattern of the pressure fluctuations.

Reference 20 presents wall-pressure fluctuation measurements along with aerodynamic noise measurements made in a water tunnel for smooth and rough surfaces. In reference 21 some measurements were made of the correlations over narrow frequency bands at low velocities. Reference 22 presents some measurements of the longitudinal space-time correlations of wall-pressure fluctuations in turbulent pipe flow.

The previously mentioned theoretical papers (refs. 14 to 17) and experimental papers (refs. 18 to 22) have indeed resulted in considerable contributions toward determining the behavior of the wall-pressure fluctuations. However, in the case of the experimental work, much of the data was taken in flows not properly simulating the desired turbulent flow and with pressure transducers somewhat limited in performance. It was felt that a need existed for additional experimental data taken for a plane wall turbulent boundary layer under carefully controlled flow conditions, and that measurements should be taken which attempt to relate the wall-pressure fluctuations to at least some of the characteristics of turbulence within the turbulent layer itself.

The present work is primarily an experimental study of the wall-pressure fluctuations of a turbulent boundary layer and of their relation to the turbulent velocities within the layer. Theoretical considerations are only presented where necessary to allow interpretation of the experimental data in terms of the applicable physical theory.

The magnitude and frequency spectral distributions of the wall-pressure fluctuations have been measured with three pressure transducers. These transducers have different effective sensitive areas and include two different types - piezoelectric ceramic and capacitive diaphragm. The results are compared with other reported measurements.

Extensive space-time correlations of the wall-pressure fluctuations have been made with the use of piezoelectric ceramic transducers. Data were obtained with the line connecting the transducers making an angle of  $0^\circ$ ,  $45^\circ$ , and  $90^\circ$  with respect to the free-stream velocity. These measurements are analyzed with the intent of relating them to the velocity characteristics of the layer.

In an attempt to relate more precisely the wall-pressure fluctuations to the velocity fluctuations of the layer, correlations of the wall-pressure transducer signals and hot-wire signals are presented and discussed. Since this type of measurement is new, its possibilities and limitations are completely discussed both from the view of physical significance and measurement technique.

Acknowledgement is made to Dr. Gustav Kuerti of Case Institute of Technology for his interest and advice in the preparation of this work.

## APPARATUS AND PROCEDURE

All the measurements were made of the turbulent boundary layers on one inside wall of the test section of a continuous-suction nonreturn wind tunnel specially designed for this investigation (fig. 1). The airflow was drawn from a very large room (with access to outside air) through a set of filters at the inlet and through a contraction section into the test section. The test section had porous inner walls on three sides to remove some of the low-energy boundary-layer air all along the side opposite the measured boundary layer and to remove it partially on the two sides adjacent to the measured boundary layer. The net result was that the longitudinal static-pressure gradient could be adjusted to be zero or even adverse.

At the exit of the test section was a vibration-isolation section after which the airflow was choked by an area-constricting section which is designated as a control block. It controls the mean flow in the test section and prevents any undesirable noises that may occur in the piping to the exhausting machinery from being propagated acoustically upstream into the test section. For further details on the wind-tunnel facility refer to appendix B, which describes it more fully.

The mean Mach number in the wind tunnel was set at 0.6. The suction flow through the porous walls was controlled to give a slightly favorable longitudinal static-pressure gradient for most of the experiments. The stagnation conditions at the inlet were atmospheric pressure and temperature. For the entire set of experiments the stagnation pressure and temperature ranged from 28.98 to 29.54 inches of mercury, and from 35° to 87° F, respectively. During any given experiment the maximum variation in stagnation pressure and temperature was  $\pm 0.04$  inch of mercury and  $\pm 7^\circ$  F, respectively. The exhaust pressure was maintained at approximately 10 inches of mercury absolute.

The mean velocity profiles of the turbulent boundary layer adjacent to the solid wall were computed from measurements made at stations along the test section with an automatically activated total-pressure probe. The mouth of the probe was flattened such that its total height was 0.015 inch, the wall thickness was 0.0025 inch, and the internal height was 0.010 inch. Contact with the wall was determined electrically. A pressure transducer (0-5 lb/sq in.) measured the differences of the boundary-layer total pressure and free-stream stagnation pressure as electrical signals. The probe travel was measured from an electrical signal from the electric probe actuator. These measurements were used to calculate the boundary-layer parameters such as  $\delta^*$ ,  $\theta$ ,  $H$ ,  $Re_\theta$ , and  $c_f$ , which was calculated from the Ludwig-Tillman equation (ref. 23).

The pressure fluctuations were measured with two types of pressure transducers. A detailed description of both types of these transducers and their calibration is given in appendix C and figure 2. Table I presents a description of the pressure transducers used along with alphabetic designations. Their spectral-amplitude response calibrations are given in figure 3.

The mean-square wall-pressure fluctuations were measured at various points along the wall with two transducers - piezoelectric transducer ZR and condenser

transducer CA. For the space-time correlations of wall-pressure fluctuations, matched pairs of 0.125-inch-diameter piezoelectric pressure transducers were used. The method of construction is the same as that for the smaller transducer ZR used to measure the magnitude and spectra. The minimum transducer separation distance was 0.181 inch, and the maximum was 6.235 inches. The 8-inch-diameter port in which the pairs were mounted could be rotated in the plane of the wall. Measurements were made at angles of  $0^\circ$ ,  $45^\circ$ , and  $90^\circ$  to the stream velocity.

In the case of the correlations of velocity and wall-pressure fluctuations, both transducers ZS and CB were used. The method of installation was similar to that for measurement of the mean-square pressure fluctuations and is indicated in figure 4.

The velocity fluctuations were measured with the use of a constant-temperature hot-wire anemometer system described in references 24, 25, and 26. A description of the method of obtaining and evaluating the hot-wire data obtained herein is given in appendix D along with some general comments on the use of the hot-wire anemometer. The stream component of the fluctuating velocity in the boundary layer was measured at several stations along the test section to establish the development of the turbulent boundary layer.

The most important use of the hot-wire probes was in obtaining the correlations of the wall-pressure and velocity fluctuations. In this case several hot-wire probes of slightly different distances from prong tips to probe centerline (see fig. 4) were used. This made it possible to make measurements of the correlation between the wall-pressure and velocity fluctuations where the hot-wire and the pressure transducer were separated by several streamwise distances  $\xi$  as measured in the plane of the wall and noted in figure 4. Separation distances  $\eta$ , where  $\eta$  is measured normal to the stream velocity vector and in the plane of the wall (fig. 4(b)), were obtained by first rotating the hot-wire probe to get the desired separation  $\eta$  and then rotating the 8-inch-diameter port within which both the pressure transducer and hot-wire probe were installed until the axis of the hot-wire probe was again parallel to the stream velocity vector, that is, the test-section longitudinal centerline.

The relative position of the hot-wire and pressure transducer in the plane of the wall was viewed and photographed by means of a specially built camera setup that allowed optical magnifications by a factor of 10 or more. Not only was adjustment of the separation distance possible with the use of this camera setup, but also a good measurement of it was made from the photographic negatives, which showed the pressure transducer and hot-wire probe with precision steel scales, having 0.01-inch markings, aligned in appropriate directions and visible in the photograph. These position photographs were taken prior to and after each survey as part of the standard data-taking procedure. Considerable attention was given to this measurement of separation distances, as preliminary experiments indicated this to be a critical point in these experiments.

For all the various types of measurements after first establishing steady-state flow conditions in the wind tunnel, the total temperature and pressure and static pressures were recorded and subsequently monitored during the entire survey. The instrumentation for obtaining and analyzing the data on the velocity

and pressure fluctuations (appendixes C and D) is indicated by the schematic diagrams in figure 5. The electrical voltages resulting from these fluctuations were measured on true rms voltmeters, recorded on a 1/10 decade spectrum analyzer and level recorder, and also recorded on a dual-channel tape recorder. In the case of the hot-wire probes, the d-c component of bridge voltage and the amount of bridge unbalance were also noted.

The spectrum analyzer and level recorder automatically scanned a set of filters centered on frequencies of 16 to 32,000 cps. Each filter set gave a one-tenth-decade band pass. The spectrum analyzer was used not only to measure the spectrum of the fluctuating velocities and wall pressures for the purpose of presenting them herein but also to monitor the functioning of all the transducers during the tape recording of the fluctuating signals to be used for correlations.

Appendix E describes the instrumentation and procedure for obtaining the correlations of the wall-pressure fluctuations and those of the wall-pressure fluctuations with the velocity fluctuations.

## RESULTS AND DISCUSSION

The mean free-stream Mach number  $M_\infty$  in the wind tunnel for the entire set of experiments was 0.6. The static pressure exhibited slight variations since for a given Mach number its value naturally depended on the total or atmospheric pressure. A typical variation of  $M_\infty$  and static pressure with longitudinal distance in the test section is presented in figure 6. It should be noted that, although the static-pressure gradient is slightly favorable throughout the test section, there is a small decrease of total pressure at large downstream positions. The Mach number does not continue to increase slightly with  $x$  but levels out and then slightly decreases with  $x$ . The mean Reynolds number per foot was  $3.45 \times 10^6$  referred to the free-stream velocity.

The decision to conduct the experiments at a nominal  $M_\infty = 0.6$  was a compromise. The low sensitivities of the pressure transducers suggested that the experiments be performed at as high an  $M_\infty$  as possible to obtain large magnitudes of pressure fluctuations. On the other hand, the problems associated with using hot wires and taking measurements in a wind tunnel increase significantly as  $M_\infty$  approaches 1. The results obtained indicate the choice of 0.6 for the nominal  $M_\infty$  to be a reasonable one.

Since no significant differences were noticed in the pressure fluctuations for the static-pressure gradient being zero or slightly favorable, all the reported results are only for the latter case.

### Velocity Characteristics of Measured Boundary Layer

Typical velocity profiles throughout the boundary layer obtained with a pitot tube are given in figure 7. Figure 7(a) shows profiles for  $z$  plotted against  $M$  for two stations at which measurements were later made of the



magnitude and spectra of the wall-pressure fluctuations, but which were upstream of the station used for correlation measurements. In figure 7(b) these two velocity profiles along with two other velocity profiles further downstream are given in terms of the dimensionless quantities  $z/\delta$  against  $U/U_\infty$ . The dimensionless profiles are plotted in figure 7(b) to compare roughly the state of development at the various stations, and it is seen that no appreciable change in the dimensionless profile occurs downstream of the second station,  $x = 9.75$  feet.

The variation of  $\delta^*$  as a function of the station  $x$  is given in figure 8. Since the data exhibit some scatter, in subsequent calculations to nondimensionalize the magnitudes and frequencies of the pressure-fluctuation measurements, the values from the faired curve were used. Local skin-friction coefficients calculated from measured values of  $\delta^*$ ,  $\theta$ ,  $H$ , and  $Re_\theta$  by means of the Ludwig-Tillman equation (ref. 23) are given in figure 9 as a function of  $Re_x$ . Also shown in the figure is the curve of the Prandtl-Schlichting equation (footnote on p. 438 of ref. 27).

Figures 10 to 12 present measurements of the longitudinal turbulent intensity. A single typical boundary-layer profile of the longitudinal turbulent intensity is presented in figure 10 to indicate that it was possible to obtain a well-defined profile if a sufficient number of points were taken with reasonable care near the point of maximum intensity. A comparison of the profiles at several  $x$ -stations is presented in figure 11. Figure 12 shows the maximum turbulent intensity of the profiles in figure 11 along with six others given as a function of the Reynolds number based on the distance along the wall or  $Re_x$ . It is interesting to note that, although small in magnitude, there is an increase in the maximum turbulent intensity with  $Re_x$ . Also shown in figure 12 is the value of turbulent intensity for the largest values of  $z$  possible with the available probe actuator (approx. 3.8 in. from the solid wall, thus close to the centerline of the tunnel). This centerline value exhibits a very slight increase similar to the maximum turbulent intensity data and a second increase in the downstream portion of the test section.

The measurements of the mean-flow profiles (fig. 7) and  $u$ -fluctuation profiles (figs. 11 and 12) indicate that a typical turbulent boundary layer is obtained. Although figure 7 shows that its development is not entirely complete for the station  $x = 2.75$  feet and is complete by  $x = 9.75$  feet, figure 12 indicates a high level of maximum turbulent intensity even at these upstream stations. At  $x = 2.75$  feet ( $Re_x = 10 \times 10^6$ ) the turbulent intensity  $\sqrt{u^2}/U_\infty$  is 0.069 as compared with 0.080 for the downstream stations. The value of 0.08 for the maximum turbulent intensity is less than that reported by Klebanoff (ref. 28), who gives 0.11. Klebanoff's measurements were made with a  $U_\infty$  of 50 feet per second in the present experiments. It is possible that in the present experiments the maximum turbulent intensity obtainable near the wall is smaller because of the increased Reynolds numbers. This could not be verified, as no reported results could be found on measurements of turbulent intensities for the high subsonic Mach number range.

As is seen in figure 13, the spectral density of the u-fluctuations exhibits good agreement with the measurements of Klebanoff. Figures 13(a) and (b) compare spectra for the inner and outer regions, respectively. In both cases the values of  $z/\delta^*$  for the pair of Klebanoff curves bracket the  $z/\delta^*$  value for the present data. None of the u-fluctuation spectral-density curves presented in figure 13 possesses a well-defined peak for the reported wave numbers.

In figure 12, the upstream level of free-stream turbulence, 0.012, while high (compared with low-turbulence wind tunnels), is not of concern to the present experiments. The increase in the stream turbulence to about 0.02 at the downstream stations is considered to be a result of the merging of the boundary layers on opposite walls of the wind tunnel. Thus, no correlation measurements and only a limited number of measurements of turbulent intensity and wall-pressure fluctuations were made in this downstream region since measurements were to be representative of a turbulent boundary layer developing along a plane wall.

### Magnitude and Spectra of Wall-Pressure Fluctuations

The wall-pressure fluctuations were measured with the aid of three different transducers. The value of  $\delta^*$  varied from 0.047 to 0.321 inch for the measurements. Figure 14 gives the  $\sqrt{p_w^2}$  divided by  $q_\infty$  plotted against  $d/\delta^*$  for transducers ZR ( $d = 0.0625$  in.) and CA ( $d = 0.43$  in.). Table I lists all the pressure transducers used along with their alphabetic designations. The  $\sqrt{p_w^2}$  were obtained from integrating the spectral values that had been corrected for amplitude response of the transducer. Both sets of data show increases in  $\sqrt{p_w^2}/q_\infty$  with decreasing  $d/\delta^*$ ; however, that for the transducer ZR ( $d = 0.0625$  in.) is within the scatter of the data. Although results are desirable for very small values of  $d/\delta^*$ , the data taken with the larger transducer serve many useful functions as will be presently seen. Two different types of pressure transducers were used to determine if any of the results were a function of the transducer type.

If the magnitudes of the wall-pressure fluctuations expressed as  $\sqrt{p_w^2}/q_\infty$  presented in figure 14 are plotted with Willmarth's data (ref. 19), the result is figure 15. In this figure the abscissa  $d/\delta^*$  is plotted on a log scale to allow the data taken with the smaller transducer ZR to be compared properly not only with Willmarth's data, but also with those of the larger transducer CA. Through Willmarth's data is the line with which he extrapolated to  $d/\delta^* = 0$  (on a linear  $d/\delta^*$  scale) to obtain his result of  $\sqrt{p_w^2}/q_\infty = 0.006$ . Two significant points can be readily made from the figure: (1) The present data do not agree with the Willmarth data in magnitude. (2) The results with the two different types of transducers behave with regard to their variation with  $d/\delta^*$  almost as if they had been taken with one transducer. If the data for downstream stations  $x$  where  $\delta^* > 0.251$  inch (tailed symbols) are disregarded for reasons previously discussed in the section on velocity characteristics of the boundary layer, then the scatter of the data is considerably reduced. The remaining

values of  $\sqrt{p_w^2/q_\infty}$  extrapolated to  $d/\delta^* = 0$  (again, on a linear scale) yield a value of 0.0075. It is of interest to note that for a turbulent pipe flow reference 22 obtained a value of 0.008 corrected to zero transducer size by a method described in reference 29. Lilley and Hodgson (ref. 16) quote in their text a value of 0.008 for  $d/\delta^* = 0.59$  from their measurement of the boundary layer on the wall of a wind tunnel.

In figures 16 and 17 the spectra of the wall-pressure fluctuations over the range of  $\delta^*$  from 0.047 to 0.251 inch are plotted in terms of the dimensionless parameters used by Willmarth (and in ref. 18). The dimensionless mean-square spectra are plotted against the dimensionless frequency, a parameter of the character of a Strouhal number if a discrete eddy of a certain size is associated with a given frequency. In figure 16(a) the data taken with transducer ZR almost completely coincide for different  $\delta^*$ . In figure 16(b) for transducer CA a similar degree of coincidence exists at the lowest and middle frequencies as in figure 16(a); but, in addition, at the high-frequency end an effect of the parameter  $d/\delta^*$  exists that spreads out the data. Figure 17 is a case where the results are given for a particular value of  $\delta^* = 0.127$  inch for transducers ZR, ZS, and ZT. The results for the 0.25-inch transducer are limited to frequencies below 10,000 cps.

In figures 16 and 17 each spectrum exhibits a maximum (designated as the relative peak of the spectrum) for values of  $(\omega\delta^*)/U_\infty$  between 0.1 and 1.0. However, as smaller values of  $(\omega\delta^*)/U_\infty$  are approached, the spectrum again increases to the limit of the available data (this maximum is designated as the absolute peak). Initially it was assumed that, despite the care with which the measurements were made, the existence of the absolute peak was due to some sources of error possibly being overlooked.

The first possibility that quickly suggests itself is that the control block did not successfully perform its function to prevent extraneous noises from propagating upstream into the test section. The results of figure 18 clearly indicate that this did not occur. Figure 18 gives the results of wall-pressure-fluctuation measurements, at one station, used for determining the effect of varying the longitudinal static-pressure gradient and also the flow conditions at the control block. There is evidence of rather large amplitudes at the low frequencies only when the flow across the control block was allowed to become definitely unchoked. In this case, there is a rather large increase in the spectral value, the maximum increase occurring at a frequency of 40 cps and being from 0.013 to about 0.52 (a factor of 4).

The possibility that fairly large amplitude low-frequency noises were propagating into the test-section from the flow entering the inlet can be ascertained by looking at the results of figure 19, in which the spectra of the wall-pressure fluctuations (taken with transducer CA) are compared with the external-noise-level spectra just upstream of the wind-tunnel inlet. In the figure the pressure fluctuations are given in terms of decibels of SPL (sound pressure level, defined as equal to  $20 \log_{10} \left( \sqrt{p^2/p_0} \right)$  where  $p_0$  is a reference pressure, usually  $2 \times 10^{-4}$  dyne/sq cm).

There is no evidence here also that the inlet noise is a problem. In fact, at any given frequency the inlet noise levels are 15 decibels or more below the spectra levels of the wall-pressure fluctuations.

In looking at the measured spectra in figure 16(a) some trend as a function of  $\delta^*$  (or station  $x$ ) is observed for the magnitude of the relative peak (occurring at the larger value of frequency). In figure 20, the spectral value that occurs at the midfrequency of the relative peak is given against  $x$ , and the trend in terms of  $F(f)$  is seen to be a very slight increase in the magnitude of the relative peak as the boundary layer thickens. Thus, as  $\delta^*$  increases, the increase in the value of  $\sqrt{p_w^2(f)}$  at the relative peak is greater than the increase of  $\sqrt{p_w^2}$ , the root-mean-square magnitude of the pressure fluctuations over the entire frequency range since  $F(f)$  is equal to  $\sqrt{p_w^2(f)}$ , the root-mean-square pressure fluctuations per unit bandwidth divided by  $\sqrt{p_w^2}$ , the root-mean-square magnitude. Plotting the frequency at which the relative peak spectra value (of fig. 20) on a log scale and  $x$  on a linear scale gives the results of figure 21. The decrease of this frequency with  $x$  (or with a thickening boundary layer) can be attributed to the increase in scale associated with increasing  $\delta^*$ . The abrupt leveling-off for the downstream portion was not anticipated and is, perhaps, due to either (1) a lack of similarity of the boundary layer for the downstream stations ( $x > 20$  ft) or (2) a lack of precision needed to determine this frequency properly.

In figure 17 the results of the dimensionless spectra plot for three different-size piezoelectric transducers definitely show the transducer-size effect on the spectra for the same value of  $\delta^*$  at constant  $Re_x$ . This is not the case in the rest of the present data and in Willmarth's data (ref. 19).

In figure 22 the dimensionless mean-square spectra of the present measurements with transducer ZR are compared with the data of Willmarth (ref. 19). The data of Willmarth show the effect of transducer size on the measured spectra. This behavior is similar to that seen in figure 16(b) for the larger diameter transducer CA. However, for the Willmarth data the rate of decrease of the spectra with increasing  $\omega\delta^*/U_\infty$  at the higher frequency end is greater than that obtained in the present experiments. This may be seen by noting that the Willmarth curve for  $d/\delta^* = 1.1$  in figure 22 agrees with the present data curve for  $d/\delta^* = 1.7$  in figure 16(b).

At the lower frequency end of the spectrum, Willmarth does not present any data below  $\omega\delta^*/U_\infty = 0.1$ . Figure 23, which is a replot of his data as SPL against frequency in cycles per second, shows that in his only dimensionless spectra plot Willmarth included no points for frequencies lower than 1000 cps. The reason for this limitation is not understood since he reported that his pressure transducer had a flat response from 5 to 50,000 cps. Furthermore, no mention was made of any problems with extraneous noises that might have interfered with the measurements of the wall-pressure fluctuations.

## Theory and Experiment Compared

A statement of the pertinent equations of the theory is now presented to aid in the comparison between the experimental data and theoretical results. If the divergence is taken of the complete equations of motion for an incompressible fluid and the equation of continuity is inserted (ref. 30), the resulting equation for the pressure field is

$$\nabla^2 \mathcal{P} = -\rho \frac{\partial^2}{\partial x_i \partial x_j} \left[ (U_i + u_i)(U_j + u_j) \right] \quad (1)$$

where  $\mathcal{P} = P(\underline{x}) + p(\underline{x}, t)$ , the sum of the time mean pressure and the fluctuating pressure. (Cartesian tensor notation is used here with subscripts  $i$  and  $j$  having values 1, 2, and 3.)

The details of the different methods of solution used by Kraichnan (ref. 15), Lilley and Hodgson (ref. 16), and Lilley (ref. 17) are not needed here. For the present purposes it is sufficient to write the solution as

$$\mathcal{P}(\underline{x}, t) = \frac{-\rho}{4\pi} \int \frac{1}{|\underline{r}'|} \frac{\partial^2}{\partial x'_i \partial x'_j} \left[ (U_i + u_i)(U_j + u_j) \right] d^3 \underline{x}' \quad (2)$$

where  $\underline{r}' = \underline{x} - \underline{x}'$  with  $\underline{x}$  being the separation-vector of the field point and the origin and  $\underline{x}'$  being the separation vector of the source point and the origin.

The covariance of the pressure is defined as the time mean of the product of the pressure at two points in space,  $\underline{x}_1$  and  $\underline{x}_2 (= \underline{x}_1 + \underline{\xi})$ , and time  $t$  and at two times  $t + \tau$ , written as

$$\overline{\mathcal{P}(\underline{x}_1, t) \mathcal{P}(\underline{x}_2, t + \tau)} = \frac{\rho^2}{16\pi^2} \iint \frac{1}{|\underline{r}'|} \frac{1}{|\underline{r}''|} \frac{\partial^2}{\partial x'_i \partial x'_j} \left[ (U'_i + u'_i)(U'_j + u'_j) \right] \frac{\partial^2}{\partial x''_k \partial x''_l} \left[ (U''_k + u''_k)(U''_l + u''_l) \right] d^3 \underline{x}' d^3 \underline{x}'' \quad (3)$$

where here

$$\underline{r}' = \underline{x}_1 - \underline{x}'$$

$$\underline{r}'' = \underline{x}_2 - \underline{x}''$$

with  $\underline{x}_1$  and  $\underline{x}_2$  being the separation vectors of the field points and  $\underline{x}'$  and  $\underline{x}''$  being the respective separation vectors of the source points.

The mean-square pressure is obtained by letting  $\tau = 0$  and  $\underline{x}_1 = \underline{x}_2 = \underline{x}$  in equation (3), the left side of which expands to

$$\overline{\mathcal{P}^2(\underline{x}, t)} = P^2(\underline{x}) + \overline{p^2(\underline{x}, t)} \quad (4)$$

The second term on the right side is the mean-square of the fluctuating pressure, while the first term is obtained from the only term that on the right side contains just the  $U_1$  velocities (i.e., the solution for the pressure due to a steady-state velocity field). The theoretical treatments have thus been concerned with describing the second term  $\overline{p^2(x,t)}$  and mean-square pressure covariance  $\overline{p(x_1,t)p(x_2,t+\tau)}$ . Of the separate terms under the bar, the steady-state term was already mentioned in connection with equation (4) and the remaining terms are of three types:

$$(1) \text{ Fourth-order covariances, } \overline{\frac{\partial u_j'}{\partial x_i'} \frac{\partial u_i'}{\partial x_j'} \frac{\partial u_l''}{\partial x_k''} \frac{\partial u_k''}{\partial x_l''}}$$

$$(2) \text{ Third-order covariances, } \overline{\frac{\partial U_1'}{\partial x_j'} \frac{\partial u_j'}{\partial x_i'} \frac{\partial u_l''}{\partial x_k''} \frac{\partial u_k''}{\partial x_l''}}$$

$$(3) \text{ Second-order covariances, } \overline{\frac{\partial U_1'}{\partial x_j'} \frac{\partial U_l''}{\partial x_k''} \frac{\partial u_j'}{\partial x_i'} \frac{\partial u_k''}{\partial x_l''}}$$

The theoretical papers (refs. 15, 16, 17) have all assumed the terms with the third- and fourth-order covariances to be negligible compared with the terms involving second-order covariances. In addition, for turbulent-boundary-layer flows the realistic assumption is made that  $\partial U_1 / \partial x_3$  is much greater than the other mean flow gradients. Consequently, the most significant term under the bar in equation (3) is

$$2 \frac{\partial U_1'}{\partial x_3'} \frac{\partial U_l''}{\partial x_3''} \overline{\frac{\partial u_3'}{\partial x_1'} \frac{\partial u_3''}{\partial x_1''}}$$

Only this term has been used to calculate the spectrum and magnitude of the mean-square pressure fluctuations and also their space-time correlations. In particular, Lilley in his theoretical treatment (ref. 17) assumes that only the portion of the layer nearest the wall contributes to the pressure fluctuations.

The root-mean-square wall-pressure fluctuations may be expressed, as in reference 16, as

$$\frac{\sqrt{p_w^2}}{q_\infty} = \beta c_F \quad (5)$$

where the value of  $\beta$  depends upon the integration indicated in equation (3) over the turbulent field.

Comparison of the present experimental data with the Lilley theory (ref. 17) is given in figure 24 where  $\beta \equiv \sqrt{p_w^2} / (q_\infty c_F)$  is plotted as a function of  $d/\delta^*$  to allow comparison with the two transducers. The Lilley theoretical result

(ref. 17) for the value of  $\beta$  is 3.1 (the revised version of ref. 16 gives 3.0 for the value of  $\beta$ ) and here appears as a straight line of zero slope since his theory does not account for the effect of nonzero transducer size. If the experimental data taken with the transducer ZR can be assumed to be correct, there is a small area of disagreement between the experimental and theoretical results in that the experimental results exhibit nonzero slopes, approximately drawn in the figure. For the very small values of  $d/\delta^*$  where no appreciable transducer-size effect should be expected, the values of  $\beta$  are larger than the theoretical value of 3.1. A replot of the data for the smaller transducer ZR on a linear scale for  $d/\delta^*$  indicates that, as  $d/\delta^* \rightarrow 0$ ,  $\beta$  approaches approximately 3.9. Lilley and Hodgson (ref. 16) also quote in their text a value of  $\beta = 3.6$  following from their own experiments.

These considerations show that a complete comparison of the experimental and theoretical results would in principle require a more accurate theory. Thus, while the agreement between experiment and theory for the value of  $\beta$  is generally good, the greater value of 3.9 for the experimental value as compared with the theoretical value of 3.1 undoubtedly results from some differences between the present experiments and the assumed models for the mean shear and the fluctuating-velocity spectrum and magnitude. As discussed later, the measured-pressure spectrum and correlations of velocity and pressure fluctuations suggest differences from the models assumed in the theoretical treatments.

In certain regions of the turbulent boundary layer or under certain types of external conditions, the terms neglected in equation (3) may become of the same order as the term that is kept in equation (5). An example of this possibility is in the outer or intermittent region where  $|\partial U_1 / \partial x_3|$  is considerably smaller than in the inner region of the layer.

A comparison of the mean-square spectra for the present data with the Lilley-Hodgson theoretical result (ref. 16) is also given in figure 22. The theoretical curve is taken from figure 4 of reference 16 without adjusting the level of the curve. The level of the peak of the theoretical curve is in good agreement with the present experimental data. Very little agreement exists between the present experimental data and this theoretical curve at both ends of the spectrum. This disagreement between the theoretical curve and the experiment should be expected when the velocity spectra upon which they are based are considered. The isotropic form of the velocity correlation function was used in evaluating the theoretical spectrum. Also, an anisotropy factor was used only in evaluating the magnitude of the pressure fluctuations (as previously done by Kraichnan (ref. 15)).

The spectra of wall-pressure fluctuations measured in reference 22 for a turbulent pipe flow also exhibit no fall-off at low frequencies for dimensionless frequencies down to a value of 0.0175, based on the radius of the pipe. However, for the spectra presented there is no indication of the double maximums. The turbulent pipe flow differs from that in the turbulent boundary layer in at least one significant aspect. For pipe flow the absence of a free-stream flow for the region away from the wall precludes the formation of a highly intermittent flow that is brought about by the convection of an irregular sharply defined boundary between the turbulent and the nonturbulent flow (see Corrsin and Kistler, ref. 31).

## Space-Time Correlation of Wall-Pressure Fluctuations

The first bit of information obtained from measurements of the space-time correlations of wall-pressure fluctuations was a curve of the correlation coefficient

$$R(\xi, \eta, \tau) = \frac{\overline{p(x_1, y_1, t) p(x_1 + \xi, y_1 + \eta, t + \tau)}}{\sqrt{\overline{p^2(x_1, y_1, t)}} \sqrt{\overline{p^2(x_1 + \xi, y_1 + \eta, t + \tau)}}} \quad (6)$$

against the time delay  $\tau$  for constant values of  $\xi$  and  $\eta$ . The separation distances are  $\xi = x_2 - x_1$  and  $\eta = y_2 - y_1$ . In equation (6) any point on the curve of  $R(\xi, \eta, \tau)$  against  $\tau$  gives the time-mean value (in coefficient form) of two fluctuating pressures where during the time-averaging the one fluctuating pressure is measured at a constant difference in time equal to  $\tau$  with respect to the other fluctuating pressure. The results of this section are all obtained from these correlation curves. The two-point wall-pressure correlation curves as a function of  $\tau$  are presented in figures 25(a) and (b) for  $\eta = 0$ . The time delay  $\tau$  is defined to be positive for a disturbance propagating downstream from one transducer to another (farther downstream). These curves are actual tracings of faired X-Y plotter curves. Figure 25(c) is for the case where the transducer separation is given by  $\xi = \eta$ . The curves in figure 25(d) are for the correlations with the transducer separation vector normal to the stream direction.

Figure 26 presents autocorrelations of the wall-pressure fluctuations as measured by several typical transducers. Figure 26(a) also shows the good repeatability of the correlation if extreme care is taken to keep all the electronics in specified working order. It should be noted that autocorrelation curves in figures 26(d) and (e) have a halved time-delay scale in comparison with the previous three curves (they look thinner, but actually are not). In obtaining autocorrelations of the played-back signal from a pressure transducer, it was noted that the correlation coefficient at  $\tau = 0$  did not quite go to 1.00 but varied from 0.93 to 0.97. This is evident in the typical autocorrelation curves given in figure 26. This result is consistent with the maximum correlation coefficients obtained for the autocorrelation of sine waves of particular frequencies (see appendix E). In the latter case the maximum measurable correlation coefficient departed from the value of 1.00 as the frequency of the sine wave was increased. The variation in the measured  $R(0, 0, \tau)$  for large  $|\tau|$  is usually within  $\pm 0.02$ , which can be attributed to instrumentation. Consequently, nothing will be inferred from the results of the  $R(\xi, \eta, \tau)$  at large  $\tau$  for any of the space-time correlation curves.

Of interest is the agreement between the spectra of the two transducer signals that were actually recorded and from which the correlation curves,  $R(\xi, \eta, \tau)$  against  $\tau$ , were later obtained. Figure 27 gives a comparison for pairs of transducers of the spectra of the signals taken just prior to recording these signals on the two-channel tape recorder. They are not corrected for amplitude response or altered in any way. The transducer pair spectra shown in figures 26(a) to (d) are typical for all the data on correlations of wall-pressure fluctuation. The fluctuation spectra for the transducer pairs indicate that fairly



good repeatability was obtained. The spectra of the wall-pressure fluctuations are essentially the same (if measured by transducers and associated instrumentation that operate ideally).

Each point of the results shown in figure 28 is obtained by first getting the maximum value of the correlation coefficient as a function of  $\tau$  for fixed separation distance in figure 25 and then plotting this maximum against the appropriate separation distance. This value of  $R$  has been designated by the subscript  $opt$ , standing for optimum in reference 32. The data in figure 28 include all three inclinations of the transducer separation vectors with the free-stream direction ( $\eta = 0$ ,  $\xi = \eta$ , and  $\xi = 0$ ).

In looking at figure 28 it is readily apparent that the longitudinal scale of the wall-pressure fluctuations is much greater than the lateral scale. For example, if scales  $L_{p_x}$  and  $L_{p_y}$  are arbitrarily defined as the value of the particular separation distance when  $R(\xi, 0, \tau_{opt}) = 0.1$  and  $R(0, \eta, \tau_{opt}) = 0.1$ , respectively, the result is

$$\frac{L_{p_x}}{L_{p_y}} = \frac{8.75 \text{ in.}}{1.18 \text{ in.}} \approx 7.4$$

In this result the values of  $\tau_{opt}$  for  $L_{p_x}$  and  $L_{p_y}$  are not the same in magnitude. For  $L_{p_x}$ ,  $\tau_{opt} = 1.33 \times 10^{-3}$  second and, for  $L_{p_y}$ , since no flow convection is involved,  $\tau_{opt} \approx 0$ . Scale  $L_{p_x}$  indicates the scale of the turbulence measured in a reference frame moving at the average convection velocity  $\xi/\tau_{opt}$ . (If the two pressure transducers at the wall were moving in the direction of flow at this convection velocity, the optimum time delay would be close to zero for the  $\xi$ -direction as well as for the  $\eta$ -direction.)

The validity of the empirical relation

$$R_{opt}(\xi, \eta, \tau_{opt_{\xi, \eta}}) = R_{opt}(\xi, 0, \tau_{opt_{\xi}}) R_{opt}(0, \eta, \tau_{opt_{\eta}}) \quad (7)$$

where

$$\tau_{opt_{\xi}} \approx \tau_{opt_{\xi, \eta}}$$

and

$$\tau_{opt_{\eta}} \approx 0$$

is shown in figure 29 where it is checked for  $\xi = \eta$ . This was done by using the curves faired through the data in figures 28(a) and (c) to obtain the calculated curve for the left side of equation (7) and then comparing it with the curve faired through the data of figure 28(b). The agreement between the two curves in figure 29 is quite good. The result should also be valid for  $\xi \neq \eta$ . The result expressed by equation (7) was first implied by the correlation data

on fluctuating velocities in a turbulent boundary layer in reference 32. Equation (7) was later assumed by Corcos, Cuthbert, and Von Winkle (ref. 29) in their calculation on the effects of finite sizes of pressure transducers.

In figure 30 the optimum correlation coefficients in the  $\xi$ -direction are compared with those measured by Willmarth. The values of  $\xi$  are divided by  $\delta^*$  to account for the differing scales in the two sets of data. The agreement between the present data and that of Willmarth is good, particularly for his data for  $M = 0.333$  and  $0.672$ .

The value of  $\tau$  at which  $R \equiv R_{opt}$  is likewise designated as  $\tau_{opt}$ . In figures 25(a) and (b) it is seen that  $\tau_{opt}$  increases as  $\xi$  is increased. The convection velocity of the wall-pressure fluctuations is defined as

$$U_c = \frac{\xi}{\tau_{opt}} \quad (8a)$$

and the ratio of the convection velocity to the free-stream velocity is simply

$$\frac{U_c}{U_\infty} = \frac{\xi}{\tau_{opt} U_\infty} \quad (8b)$$

These values of  $U_c/U_\infty$  were plotted against the appropriate separation distance in figures 31(a) and (b) for  $\eta = 0$  and  $\xi = \eta$ , respectively. For  $\xi < 1.0$  inch in figure 31(a)  $U_c/U_\infty$  increases at smaller rate with increasing  $\xi$ . In figure 31(b) at values of  $\xi > 1.0$  inch the values of  $U_c/U_\infty$  start to fall with increasing  $\xi$ . A check of the  $R$  against  $\tau$  curves for these points shows very small values of  $R_{opt}$  and very flat curves. Consequently, not too much reliance should be put on the data at large  $\xi$ .

The convection velocity results given in figure 31 are quite interesting in that at large values of  $\xi$  they essentially agree with the convection velocity values obtained by Willmarth (ref. 19) (excepting his  $M = 0.672$  data) and Von Winkle (ref. 22). At the smaller values of  $\xi$  the convection velocity ratio  $U_c/U_\infty$  begins to decrease significantly as  $\xi$  is decreased. This result can reasonably be interpreted if one considers the decay and convection of the different size eddies that probably exist in the boundary layer. The smaller scale eddies should have a shorter lifetime compared with the larger scale eddies. Consequently, as the separation distance between the two pressure transducers is increased, the effect of the smaller scale eddies on the correlation of the pressure fluctuations measured by these transducers should decrease with the correlation being affected only by the large-scale eddies in the boundary layer. Finally, the small-scale eddies occur or are concentrated closer to the wall than are the large-scale eddies. Thus, the small-scale eddies are convected at slower velocities than are the large-scale eddies. This simplified picture is proposed to describe the results of figure 31 for small values of  $\xi$ .

This interpretation of the figure 31 data implies that the values of  $U_c/U_\infty$  should decrease with increasing frequency. Correlation of the data in narrow frequency bands was not done with the present data. However, the results of reference 22 for turbulent pipe flow indicate such a trend. Figure 36 of reference 22 shows that, as the frequency increases by a factor of 2.8, the values of  $U_c/U_\infty$  decrease from 0.83 to 0.75.

A comparison of the  $U_c/U_\infty$  data with Willmarth's results is presented in figure 32. To take into account the range in the values of  $U_\infty$  and  $\delta^*$ , the  $U_c/U_\infty$  values are given as a function of  $U_\infty/(\xi/\delta^*)$ . Initially, the dimensional parameter  $U_\infty/\xi$  was considered. Dividing  $\xi$  by  $\delta^*$  does account for the different length scales. A suitable velocity is not available (the acoustic velocity is not appropriate here) with which to make the entire parameter dimensionless. However, this choice of parameters should account for the different velocity and length scales. The comparison of the  $U_c/U_\infty$  data does show that the scatter in the data is nearly the same and the agreement is good. The limited range of the  $U_\infty/(\xi/\delta^*)$  parameter for the Willmarth data as compared with the present data simply results from the smaller range of  $\xi$  for which measurements were made by Willmarth. The abscissa positions of the Willmarth data relative to the present data show why smaller values of  $U_c/U_\infty$  could not be obtained in his experiment. The results in figure 32 indicate that in addition to considering the size of the transducers relative to a boundary-layer scale as noted by Willmarth (ref. 19) it is necessary to consider very small separation distances  $\xi$  (relative to some boundary-layer scale such as  $\delta^*$ ) when convection velocities of pressure fluctuations are to be determined.

Measurements for  $M_\infty$  from 2.0 to 5.0 by Laufer and Kistler (reported in ref. 33) indicate at least a qualitative agreement with the data in figure 31. Measurements are reported for only two values of  $\xi$  (0.25 and 0.50 in.) with the values of  $U_c/U_\infty$  varying between 0.65 and 0.77. At each  $M_\infty$  the value of  $U_c/U_\infty$  for the larger  $\xi$  is greater than that for the smaller  $\xi$  with the average increase being about 7 percent.

The preceding discussion indicates that, as expected, the value of the apparent convection velocity depends on the relative magnitudes of (1) transducer size and separation distance and (2) the sizes of the eddies and their velocities of convection in the layer. Therefore, these results apply only to convection velocities of the wall-pressure fluctuations of turbulent boundary layers along a plane wall under the aforementioned conditions of measurement. They may not apply in general where larger size transducers, larger separation distances, or a different type of turbulent flow is involved.

The correlation results for the limited frequency bandwidth data are presented in figures 33 to 35. The effect of high-pass filtering (which equals rejection of a low-frequency band of the signals) on typical correlations is given in figure 33 for (1) an autocorrelation ( $\xi = \eta = 0$ ), (2)  $\xi = 0.88$  inch and  $\eta = 0$ , and (3)  $\xi = 0$  and  $\eta = 0.325$  inch. The effect of low-pass filtering is presented in figure 34 in a fashion similar to that of figure 33. The effect of the high-pass and low-pass filtering on the optimum correlation coefficients as obtained from figures 33 and 34 is given in figure 35.

With regard to the present experiments, some concern has been expressed that the large magnitudes of the spectrum of the wall-pressure fluctuations at the lower frequencies may have resulted from some as yet undetermined wind-tunnel effect. Since this increase in the magnitudes occurs approximately at frequencies below 400 cps, a comparison of the correlation data for the full bandwidth spectrum with those for which the portion of the spectrum below 400 cps is rejected would indicate how significant is this lower frequency range on the space-time correlations. It is seen in figures 33(b), 33(c), and 35 that rejecting the portion of the spectrum below 400 cps results in optimum correlation coefficients that do not change appreciably from those for the entire spectrum. In particular for the 400-cps high-pass condition, the  $R_{opt}$  are approximately only 10 percent less than those for the full-band-pass results. This change in  $R_{opt}$  is consistent with the rejecting of even larger portions of the lower frequency end of the spectrum, that is, 800 cps, 1600 cps high-pass, and so forth, with the result that the value of  $R_{opt}$  continues to decrease (monotonically).

Except for the autocorrelations in figure 33(a), restricting the portion of the spectrum progressively toward the higher frequency end gives successively smaller values of  $\tau$  for the first zero-crossing of the correlation curves and reduces the value of  $R_{opt}$ . Conversely, restricting progressively the portion toward the lower frequency end gives successively larger values of  $\tau$  for the first zero-crossing of the correlation curves and increases the value of  $R_{opt}$ . In addition, damped oscillations of the curves about the horizontal occur as the rejected band is increased for either the high-pass or low-pass analysis. These damped oscillations are characteristic of correlations of two fluctuating quantities limited to a narrow band of frequencies. Similar results were obtained by Dryden, et al. (ref. 34) in one of the earliest examples of the effect of filtering in frequency bands on the autocorrelation coefficients of velocity fluctuations as a function of separation distances. A final remark on the results of figures 33 to 35 is that they give a good indication of the distortion possible in correlation results obtained with instrumentation possessing insufficient extent of usable frequency bandwidth, particularly at lower frequencies.

### Correlations of Velocity and Wall-Pressure Fluctuations

Investigations on the correlations of pressure with velocity in turbulent flow fields have generally not been attempted either on an experimental or theoretical basis. Reference 35 does give some numerical results for the covariances  $\overline{pu_k^2}$  for isotropic turbulence. The role of the pressure-velocity-gradient covariance  $p \frac{\partial u_k}{\partial x_l}$  is discussed in reference 36. The particular form of the pressure-velocity covariance of interest herein is  $\overline{pu_k}$ . The defining equation for  $\overline{pu_k}$  is given by Batchelor (ref. 37) as (in the present notation)

$$\overline{pu_k''} = \frac{\rho}{4\pi} \int \frac{1}{|r'|} \frac{\partial^2 (U_1' + u_1') (U_j' + u_j') (U_k'' + u_k'')}{\partial x_1' \partial x_j'} d^3 \underline{x}', \quad (9)$$

if an incompressible fluid in an infinite region is assumed. The corresponding correlation coefficient is given by  $\frac{\overline{p u_k''}}{\overline{p u_k''}}$  divided by the product of the root-mean-square wall-pressure and velocity fluctuations.

The purpose behind measuring these correlations is to determine what regions within the boundary layer contribute to the pressure fluctuations at the wall. Measurements of the pressure fluctuations at one point at the wall or their space-time correlations do not yield any detailed information on what regions do contribute. Actually, a study of the correlations with each of the components of the fluctuating velocity would be desirable. In particular, the theoretical considerations of reference 16 indicate the w-component to be the most significant one. However, the measurements of  $v$  or  $w$ , the fluctuating-velocity components normal to the free-stream direction, would require two hot wires in the available experimental setup. (The method requiring the rotation of only one wire could not be used because of the necessity of keeping the hot-wire position fixed relative to the pressure-transducer position for a given measurement, i.e., a single recording on magnetic tape.) Thus, getting a measure of  $\overline{p w}$  or  $\overline{p v}$  would ordinarily require at least three channels on the tape recorder. As noted previously, the tape recorder and playback units available for use had only two channels.

Typical space-time correlation curves obtained for the correlation of the velocity fluctuations with wall-pressure fluctuations are presented in figures 36 and 37. The correlation coefficient used in this section is defined by equation (9) and is obtained as discussed in appendix E. The script  $\mathcal{R}$  for the velocity-pressure correlation is used here to distinguish it from the space-time correlations of the wall-pressure fluctuations. The definition of positive values of  $\tau$  for the pressure-velocity correlations is that a disturbance propagating downstream is first sensed by the wall-pressure transducer and at a later time  $\tau$  is sensed by the hot wire. As for the previous type of correlation measurements, each curve presented in figures 36 and 37 is a direct tracing of a faired curve of the X-Y plotter curve. In some cases the X-Y plotter curve was retraced several times over the original one to allow a better fairing.

The results given in figures 36(a) to (d) are for the correlations measured with transducer ZS and for a separation distance  $\eta$  of approximately zero and for various values of  $\xi$ . Similar characteristics are obtained for the correlation curves in each of figures 36(a) to (d). Peaks in the correlation coefficient generally occur at two values of time delay  $\tau$ . The major peak generally occurs at small positive values of  $\tau$  ranging to +0.3 millisecond; the secondary peak occurs at values of  $\tau$  ranging between -0.7 and -0.8 millisecond. For purposes of identification, values of  $\tau$  and  $\mathcal{R}$  for the major peaks are labeled with the subscript  $opt$  and for the secondary peaks ( $\tau < 0$ ) with the subscript  $s$ .

A typical correlation curve for  $z$  less than 0.3 inch does not have a secondary peak but, for  $\tau < \tau_{opt}$ , generally increases monotonically with increasing  $\tau$  and then decreases monotonically for  $\tau > \tau_{opt}$ . For values of  $z$  greater than 0.3 inch, the emergence of  $\mathcal{R}_s$  caused most of the  $\mathcal{R}$  against  $\tau$  curves to have two rounded peaks of about the same magnitude at the smaller

values of  $z$  and, for  $z$  between 0.72 to 1.52 inches, resulted in  $R_s$  being greater in magnitude than  $R_{opt}$ . In other words, regardless of the value of the separation distance  $\xi$ , for positions of the hot wire close to the wall the  $R_{opt}$  is the greater one, but for positions away from the wall  $R_s$  is of the same order or even slightly greater than  $R_{opt}$ .

The correlations shown in figures 36(e) to (i) were measured with transducer ZS for a separation distance  $\xi$  of approximately zero and for various lateral separation distances  $\eta$ . The results in figures 36(a) and (e) are taken from different experimental surveys, although both are for  $\xi \approx \eta \approx 0$ . The correlation curves for the smaller values of  $\eta$  (figs. 36(e) to (i)) have the same general contours as those of figures 36(a) to (d) for various values of  $\xi$ . Values of  $R_s$  in figures 36(e) to (i) are of a magnitude similar to those of figures 36(a) to (d).

Only one set of correlation curves is presented for the case where the transducer CB is used to measure the wall-pressure fluctuations. In figure 37 the correlation curves are given for  $\xi \approx 0$  and  $\eta = 0.003$  inch. These results confirm the measurements using transducer ZS; however, the peak values are generally somewhat lower in magnitude. In addition, the curves are not as well behaved as those in figures 36(e) to (i) as  $R_{opt}$  is approached from negative values of  $\tau$ .

Significant characteristics of the correlation curves are plotted in figure 38. These curves include results not presented in the preceding figures. Figure 38(a) is based on data obtained using transducer CB. The curves in the figure were faired according to the data of survey 2 before putting in the points for survey 1; the values of  $R_{opt}$ ,  $\tau_{opt}$ ,  $R_s$ , and  $\tau_s$  are given as a function of  $z$ . Considerable scatter is evident in the figures for  $\tau_{opt}$  and  $\tau_s$ . This is to be expected because in the original X-Y plotter curves 0.10 inch of x-scale ( $\tau$ ) is equal to 0.02 millisecond. Even with the most careful reading the scatter cannot be reduced. The general trend in  $\tau_{opt}$  is to increase in value with an increase in  $z$ . In the case of  $\tau_s$  (fig. 38(a)), the faired curve could very easily be replaced by a straight line. However, in most  $\tau_s$  data some non-linearity is indicated. The values of  $R_s$  (fig. 38(a)) show the increase in the outer portion of the boundary layer already referred to in figures 36 and 37.

Figure 38(b) gives the significant characteristics of the correlation curves using transducer ZS, various values of  $\xi$ , and  $\eta \approx 0$ . The  $R_{opt}$  and  $R_s$  data in figure 38(b) do not indicate a steady trend as do counterparts in figures 38(c) and (d). The variation of  $\tau_{opt}$  with  $z$  in figure 38(b) is such that, at any value of  $z$  greater than about 0.1 inch,  $\tau_{opt}$  increases as  $\xi$  is increased. For any value of  $\xi$  the variation of  $\tau_{opt}$  with  $z$  is approximately linear if  $z$  is greater than 0.2 inch. Over most of the range of  $z$  values,  $\tau_s$  also increases (values become less negative) as  $\xi$  is increased (fig. 38(b)).

In figure 38(c) the results are as for their counterparts in figure 38(b) except that here  $\xi \approx 0$  and each figure contains curves for the various values

of  $\eta$ . In figure 38(c) the results of  $R_{opt}$  against  $z$  are indeed a very regularly behaved set of data in contrast to the data of figure 38(b). The maximum values of  $R_{opt}$  for each curve  $\eta = \text{constant}$  are progressively smaller and occur at larger values of  $z$  as  $\eta$  is increased. The curves of  $\tau_{opt}$  as a function of  $z$  in figure 38(c) exhibit a marked change of slope for  $\eta$  greater than about 0.4 inch. For values of  $z$  less than 0.4 inch, a systematic change also occurs in that larger values of  $\tau_{opt}$  appear to be reached for  $\eta$  larger as  $z$  gets smaller. There is only a slight systematic trend in the maximum values of the  $R_s$  against  $z$  curves with  $\eta$ ; the curves of  $\tau_s$  against  $z$  show an overall increase in  $\tau_s$  with increasing  $\eta$ .

In figure 38(d) the results are similar to their counterparts in figure 38(b); here transducer CB is used. Considerable portions of the curves in figure 38(d) are extrapolated (through widely scattered data) as indicated by the dashed lines.

In figures 39 and 40, respectively, are presented some typical turbulent-intensity profiles and spectra obtained during the surveys prior to the correlation measurements of this section. The root-mean-square velocity fluctuation divided by the local mean velocity in the boundary layer is given in figure 39(a). In figure 39(b) the root-mean-square velocity fluctuations are divided by the free-stream velocity. These two figures are presented to show that the measured values of turbulent intensity were fairly consistent from survey to survey with the variation in values at a particular value of  $z$  being no more than  $\pm 4$  percent. The spectra were quite repeatable on each survey as is indicated by figures 40(b) and (c).

Two possibly serious problems must be considered in trying to make meaningful measurements of the correlation of wall-pressure and velocity fluctuations. One is the fact that the velocity-fluctuation transducer (the hot-wire anemometer) and the pressure-fluctuation transducers are probably not perfectly matched transducers with regard to their phase-angle response as a function of frequency. The necessity to consider not only amplitude response but also the phase-angle response of a transducer over the frequency range of interest arises from the fact that, if two transducers have at a particular frequency two considerably different values of phase angles  $\phi_1$  and  $\phi_2$ , at that frequency the correlation will be a function of  $\cos(\phi_2 - \phi_1)$ .

Although these phase-angle characteristics were not measured, it can be stated that for the frequency range of interest, 50 to 15,000 cps, the phase angle as a function of frequency for the piezoelectric transducer shows somewhat less variation than that for the condenser transducer. This remark follows from comparing their amplitude response as a function of frequency (fig. 3). The piezoelectric transducers exhibit less variation over the indicated frequency range than the condenser transducer. Elementary considerations of transducer theory show that this will lead to less variation in the phase-angle characteristic as a function of frequency (ref. 38).

As is seen by comparing figures 36(a) and 37, there is fair agreement between the correlation curves for the two types of transducers. The most

noticeable difference between the two sets of data is that the values of  $R$  are slightly lower for the set where the pressure transducer is of the condenser type. This result is consistent with the preceding remarks on the phase-angle characteristics of the two types of pressure transducers. Thus, for these purposes the piezoelectric transducers are more nearly matched to the hot-wire anemometer than are the condenser transducers. If a phase-angle difference does exist between the velocity and pressure transducers used to obtain the correlations, its effect would be to reduce to a certain extent the magnitudes of the correlation coefficients. This implies that ideally matched transducers might yield even larger values of the correlation coefficient than those measured. Consequently, the magnitudes of the correlation coefficients measured may be regarded as tentative results.

The second major problem encountered in the measurement of the pressure-velocity correlations is the existence of interference between the hot-wire probe and the flow field as indicated in figure 41, which presents the spectra of the wall-pressure fluctuations measured during the correlation experiments. The data in these figures indicate that the shapes of these wall-pressure fluctuation spectra are affected to a certain extent by the proximity of the hot-wire probe. The spectra in figures 41(a) to (d) are taken with transducer ZS for  $\eta \approx 0$  and various values of  $\xi$ . In figure 41(a) with  $\xi = -0.001$  inch, that is, with the hot wire directly above the pressure transducer, the spectral values below 400 cps increase in magnitude as the  $z$  values get smaller, whereas the spectral values for frequencies above approximately 400 cps are decreased.

The effect of moving the hot-wire probe downstream away from the pressure transducer is noted by comparing figures 41(a) to (d) with each other. Virtually no increase in the value of  $F(f)$  is obtained for the frequencies lower than about 400 cps as the values of  $z$  are allowed to decrease. The effect of the proximity of the hot-wire probe on the wall-pressure fluctuations is shown in figures 41(e) to (i), with the displacements in the plane of the wall now being only a direction normal to the free stream. In figure 41(e), with  $\eta$  equal to 0.002 inch, that is, approximately zero, the effect of decreasing the values of  $z$  is the same as that for figure 41(a) (as expected, since for both figures  $\xi \approx \eta \approx 0$ ). The effect of the proximity of the hot-wire probe exists to a slight degree at  $\eta = 0.186$  inch in figure 41(g). It is not evident at  $\eta = 0.390$  inch in the data of figure 41(h); a similar condition exists for  $\eta = 0.671$  inch in figure 41(i).

As shown in figure 42 the autocorrelation curves for the hot-wire signals at positions near the wall for cases where  $\eta$  is approximately zero and  $\xi$  has various values clearly indicate that the hot-wire signals are essentially unaffected by the nearness of the hot-wire probe to the pressure transducer. On the other hand, as seen in figure 43, which presents the autocorrelation curves for the wall-pressure fluctuations (as measured by transducer ZS) with the hot-wire probe positioned at  $z = 0.016 \pm 0.002$  inch,  $\eta \approx 0$ , and various values of  $\xi$ , the proximity of the hot-wire probe affects the wall-pressure fluctuations. Thus, it is noted that for  $\xi$  of 0.200 and 0.307 inch the shapes of the autocorrelation curves approach those produced by the piezoelectric transducers used in the space-time correlations of the wall-pressure fluctuations (cf. fig. 26).



From figures 41 and 43 it is thus noted that only the magnitudes of the lower frequency portion of the spectrum of the wall-pressure fluctuations are increased as  $z$  is allowed to decrease for  $\xi$  and  $\eta$  approximately less than 0.20 inch. Consequently, one may omit from serious consideration those correlations for smaller values of  $z$  ( $<0.20$  in.) when  $\xi$  and  $\eta$  are less than  $\approx 0.20$  inch. On the other hand, all the data may be considered if one observes the effects of filtering out the lower frequency portion of the spectrum, which is apparently most affected by the interference. Figure 44 presents the effect of using only a certain portion of the spectrum in the correlations of the velocity fluctuations with the wall-pressure fluctuations. The correlation curves are the full band pass and 400-, 3000-, and 6000-cps high-pass band ( $\xi \approx \eta \approx 0$ ). It is only in the range of frequencies below 400 cps that the spectra of the wall-pressure fluctuations show any appreciable interference effect from the hot-wire probe. Consequently, the fact of particular interest in figure 44 is the comparison of the peak correlation coefficient for the full band pass with that for the 400-cps high-pass band. The values of  $R_{opt}$  are 0.60 and 0.52 for the full band pass and 400-cps high-pass band, respectively. This indicates that the fluctuations below 400 cps do not contribute appreciably to the correlation coefficients measured. Consequently, this interference effect should not affect the measurements of pressure-velocity correlation. As in the case of the space-time correlations of the wall-pressure fluctuations, the rejection of this lower frequency portion of the spectrum also serves to remove those portions of the spectra that might be affected by wind-tunnel disturbances.

In figure 44 the correlation curve of  $R$  as a function of  $\tau$  was made considerably narrower when the portion of the spectrum below 400 cps was filtered out. In addition to the normal effect of using filters, this narrowing actually might be the result of rejecting those portions of the spectrum affected by interference. In the following only the magnitudes of  $R$  and  $\tau$  at the peaks will be discussed. Considerations of the shapes of the curves will not be particularly stressed.

The results given in figures 36 to 38 indicate that the u-component of the fluctuating velocity does make some contribution to the pressure fluctuations at the wall. This follows from the fact that nonzero values of  $R$  were obtained. The results indicate that there are two regions in the boundary layer where the u-component contributes to the pressure fluctuations at the wall. These are the inner region (close to the wall) and the outer region, which is highly intermittent. While the magnitudes of the  $R$  obtained for the inner region ( $R_{opt}$ ) are higher than those obtained for the outer region ( $R_g$ ), the amount of actual contribution of these two regions will depend on the volumes in each region over which the  $R$  is appreciable.

According to the leading assumptions in the Lilley-Hodgson theory (ref. 16), the wall-pressure fluctuations depend significantly only on the w-component of velocity fluctuations for the inner region of the boundary layer. This implies that, in correlating the wall-pressure fluctuations with the velocity fluctuations, larger magnitudes of the correlation coefficients may be obtained with the w-component of velocity fluctuations than with the other two components. As the other components of velocity fluctuations were not measured and were not correlated with the pressure fluctuations, the results between components cannot be

compared. However, it is to be noted that any given value of  $R$  for the particular  $\xi$ ,  $\eta$ ,  $z$ , and  $\tau$  is the covariance  $\overline{p_w u}$  divided by the product of  $\sqrt{p_w^2}$  and  $\sqrt{u^2}$ . What would be more appropriate is to get a value  $R'$  defined as

$$R' = \frac{\overline{p_w u}}{\sqrt{p_w^2} \sqrt{u^2 + v^2 + w^2}} \quad (10)$$

which is simply

$$R' = R \frac{\sqrt{u^2}}{\sqrt{u^2 + v^2 + w^2}} \quad (11)$$

in terms of  $R$ , the measured correlation coefficient.

Although no measurements were made of  $\overline{v^2}$  and  $\overline{w^2}$ , values of  $R'$  can be computed using the data of Klebanoff (ref. 28). For the inner region of the boundary layer it is seen from figure 38(b) that the measured  $R_{opt}$  as a function of  $z$  has maximum values approximately at  $z = 0.08$  inch, which becomes  $z/\delta^* = 0.45$  with  $\delta^* = 0.178$  inch. For  $z/\delta^* = 0.45$ , Klebanoff's data yield the values  $\sqrt{u^2} = 0.08$ ,  $\sqrt{v^2} = 0.06$ , and  $\sqrt{w^2} = 0.035$ . Thus,

$$\frac{\sqrt{u^2}}{\sqrt{u^2 + v^2 + w^2}} = \frac{0.08}{0.106} = 0.76 \quad (12)$$

For a measured value of  $R = 0.34$  with  $\xi \geq 0.20$  inch and  $\eta \approx 0$ , a value of  $R'$  of 0.26 is obtained. It is now evident that, even for the correlation coefficients based on the root mean square of the entire velocity fluctuations, for the inner region significant nonzero values of correlation are obtained between the wall pressure and u-component of velocity fluctuations. And yet, as previously pointed out, if the theoretical model is correct, the correlations between the pressure and w-component of velocity fluctuations should yield much higher values of correlation coefficients, where  $R$  in this case must be defined as

$$R = \frac{\overline{p_w w}}{\sqrt{p_w^2} \sqrt{w^2}} \quad (13)$$

In the curves of  $R$  against  $\tau$  the peak correlation coefficients designated as  $R_s$  attain maximum values for  $z$  values that are much larger than those for the  $R_{opt}$  values already discussed. (The "secondary" peaks  $R_s$  are those peaks occurring at negative time delays of nearly 1 msec in contrast to the  $R_{opt}$  peaks which occur at positive time delays near zero.) The initial reaction in viewing these  $R_s$  peaks for the preliminary results was that they were erroneous. The entire system of measurement and correlation was thoroughly checked. These peaks were not found to be the result of some problem of instrumentation or measurement such as the interference effect of the hot-wire probe. For this

range of  $z$  the interference effect of the hot-wire probe was negligible for all values of separation distances  $\xi$  and  $\eta$ .

Since this result is limited to the outer region of the boundary layer, the intermittency that also exists in this region is considered to be quite significant. In figure 45 the data of Klebanoff (ref. 28) and Corrsin and Kistler (ref. 31) for the intermittency factor  $\gamma$  are compared with  $R_g$  as a function of  $z/\delta^*$  for several surveys. For the Klebanoff data, originally given as  $\gamma$  as a function of  $z/\delta^*$ , his mean-velocity data were used to calculate  $\delta/\delta^*$  to obtain  $\gamma$  as a function of  $z/\delta^*$ . Because the Corrsin-Kistler experiments used a corrugated wall, the calculation of  $\delta^*$  from the mean-velocity profile was considered unwise in this case. Since both Klebanoff and Corrsin-Kistler gave  $\gamma$  as a function of  $z/\delta$ , the method of converting  $\gamma$  into a function of  $z/\delta^*$  was first to compare the Klebanoff and Corrsin-Kistler data at a particular value of  $z/\delta$  and then to use the Klebanoff  $z/\delta^*$  to plot the value of  $\gamma$  for the Corrsin-Kistler data.

In figure 45 the maximum values of  $R_g$  occur in the intermittent region of the layer as defined by  $\gamma$  as a function of  $z/\delta^*$ . Particularly good agreement seems to exist with the intermittent region as defined by the Corrsin-Kistler data. Their data compared with the Klebanoff data show a stronger penetration of the intermittent fluctuations at distances greater than  $\delta$ . The agreement between  $R_g$  and  $\gamma$  is tempered by the fact that nonzero values of  $R_g$  extend out to larger values of  $z/\delta^*$  than do the nonzero values of  $\gamma$  for either the Klebanoff or Corrsin-Kistler data. While the intermittency factor  $\gamma$  was not measured in the present investigation, the turbulent intensities (fig. 39(b)) for the outer region of the boundary layer are greater and extend further from the wall compared with the Klebanoff or the Corrsin-Kistler data. As previously remarked, the magnitudes of these  $R_g$  values are approximately one-half the  $R_{opt}$  values obtained in the inner region. Furthermore, if again  $R'$  is calculated by using Klebanoff's data, which show that for the outer region  $\sqrt{u^2} \approx \sqrt{v^2} \approx \sqrt{w^2}$ , there is obtained

$$R' = R \frac{\sqrt{u^2}}{\sqrt{u^2 + v^2 + w^2}} = 0.57 R$$

This implies that, although the  $u$ -component fluctuations in the outer region contribute to the wall-pressure fluctuations, the magnitude of the contribution from a particular point is not as great as that from the inner region.

For most of the values of  $\xi$  and  $\eta$ , the time delays  $\tau_{opt}$  generally increase with increasing  $z$ . Attempts at trying to relate the  $\tau_{opt}$  values to the convection velocities measured in the space-time correlations of wall-pressure fluctuations have not been successful using the present data.

The negative values obtained for the time delays denoted as  $\tau_g$  in figures 38(b) and (c) indicate a behavior of the correlation of the velocities with the wall-pressure fluctuations different from that for the inner region ( $R_{opt}$  and  $\tau_{opt}$ ). These negative  $\tau_g$  values require that even for  $\xi \equiv 0$  the velocity

fluctuations that correlate with the wall-pressure fluctuations must occur some distance upstream of the pressure transducer and hot-wire probe. This is interesting in that it agrees with the results of reference 39. This reference shows (in fig. 4 therein) results that indicate that the u-component of the fluctuating velocities does have an effective eddy convection velocity in the z-direction, but that it is considerably less than that for the free-stream direction. These results imply that the large-scale velocity fluctuations in the outer region that eventually affect the pressure at the wall must originate a considerable distance upstream in order for the slower convection in the z-direction to have sufficient time to reach the wall. Rough calculations of  $\tau_s$  based on the results of reference 39 give values from  $-0.45 \times 10^{-3}$  to  $-0.6 \times 10^{-3}$  second, whereas the present results range from  $-0.7 \times 10^{-3}$  to  $-0.8 \times 10^{-3}$  second. However, it is not suggested that this simple concept sufficiently explains the phenomenon.

### CONCLUSIONS

The following conclusions may be drawn from this experimental investigation of the wall-pressure fluctuations in a turbulent boundary layer:

1. The value of the root-mean-square wall-pressure fluctuations approaches  $\sqrt{p^2} = 0.0075 q_\infty$  as  $d/\delta^*$  approaches zero (where  $q_\infty$  is the free-stream mean dynamic pressure,  $d$  is the diameter of the pressure transducer, and  $\delta^*$  is the displacement thickness of the boundary layer).
2. The measured values of  $\beta$  in the relation  $\sqrt{p_w^2}/q_\infty = \beta c_f$  (where  $c_f$  is the local skin-friction coefficient) depend on  $d/\delta^*$ . By extrapolating the measured  $\beta$  to  $d/\delta^* = 0$ , there results  $\beta = 3.9$ , which is in good agreement but slightly higher than the value of 3.1 obtained from the most recent Lilley analysis (ref. 17).
3. As the transducer size is decreased, the dimensionless mean-square spectrum  $[\tilde{p}(\omega)U_\infty]/(q_\infty^2 \delta^*)$  of the wall-pressure fluctuations apparently approaches a universal function of the dimensionless frequency  $\omega \delta^*/U_\infty$  as indicated by Willmarth for the upper range of  $\omega \delta^*/U_\infty$ , but this universal function agrees with the data obtained by Willmarth only for his lowest reported values of  $\omega \delta^*/U_\infty$ .
4. The dimensionless mean-square spectrum of the wall-pressure fluctuations as a function of the dimensionless frequency  $\omega \delta^*/U_\infty$  does not agree with the Lilley-Hodgson theoretical result (ref. 16) except near the peak of the theoretical spectrum (fig. 22).
5. The values of the correlation coefficients  $R_{opt}$  as a function of  $\xi/\delta^*$  (the longitudinal separation distance divided by the boundary-layer displacement thickness) agree with those obtained by Willmarth (fig. 30).
6. Measurements of the correlation coefficients  $R_{opt}$  in the lateral direction  $\eta$  indicate that their scale is  $1/7.4$  of those obtained for the  $R_{opt}$  in the longitudinal direction  $\xi$ .

7. Measurements indicate that for any  $\xi$  and  $\eta$  separation the  $R_{opt}$  can be obtained from the relation  $R_{opt}(\xi, \eta, \tau_{opt}) = R_{opt}(\xi, 0, \tau_{opt})R_{opt}(0, \eta, \tau_{opt})$  (fig. 29).

8. The ratio of the convection velocity to the free-stream velocity  $U_c/U_\infty$  is shown not to be a constant but to increase with increasing separation distance  $\xi$  and for the larger separation distances to agree with the values obtained by Willmarth. This variation in the magnitude of the convection velocity is explained in terms of the relative distances in which the small- and large-scale eddies are coherent (fig. 32).

9. Correlations of the wall-pressure fluctuations with the longitudinal component of the velocity fluctuations indicate that the contributions to the wall-pressure fluctuations are associated with two regions - an inner region near the wall and an outer region linked with the intermittency near the edge of the boundary layer. In the outer region the intensity of the contributions of the velocity fluctuations to the wall-pressure fluctuations as indicated by the magnitude of the correlation coefficients is less than one-half that for the inner region.

#### CONCLUDING REMARKS

In the previous section several definite conclusions have been stated. Some further remarks on the results can be made.

1. To lessen the disagreement between the available theoretical analyses and the available experiments on the spectra of the wall-pressure fluctuations probably requires that less simplified assumptions be used in the theoretical work. Some additional experimental work should be performed to corroborate the results of this investigation, particularly for values of dimensionless frequency  $\omega\delta^*/U_\infty$  smaller than 0.07.

2. The results obtained for the correlations of the u-component of velocity fluctuations with the wall-pressure fluctuations definitely suggest that experiments be performed to study the intensity and extent of the correlations where the other two components of velocity fluctuations are used. Since the theoretical models for the problem suggest that the w-component of the velocity fluctuations is the dominant one in contributing to the wall-pressure fluctuations, correlation coefficients of greater magnitude should be obtained for the correlations with the w-components than those with the u-components. More elaborate facilities than those used herein would be required for these measurements.

3. The successful measurement of the correlations of the wall-pressure fluctuations with any component of the velocity fluctuations has been reported for the first time here. It is suggested that this type of measurement should be considered for use in studying other types of fluctuating fluid flows.

Lewis Research Center

National Aeronautics and Space Administration  
Cleveland, Ohio, September 19, 1962

# APPENDIX A

## SYMBOLS

|                     |  |
|---------------------|--|
| $a$                 | speed of sound, ft/sec   |
| $c_f$               | local skin-friction coefficient defined as local viscous shear stress at wall divided by dynamic pressure evaluated at free-stream conditions, dimensionless       |
| $d$                 | diameter of pressure transducers, in.  |
| $F(f)$              | spectrum function, $\sqrt{p^2(f)}/\sqrt{p^2}$ , (sec) <sup>1/2</sup>   |
| $\mathcal{F}(f)$    | spectral-density function, $\overline{p^2(f)}/p^2$ or $\int_0^\infty \mathcal{F}(f)df = 1$ , sec   |
| $\mathcal{F}(k)$    | $\frac{U}{2\pi} \mathcal{F}(f)$ , cm   |
| $f$                 | frequency, sec <sup>-1</sup>   |
| $H$                 | ratio of $\delta^*$ to the momentum thickness $\theta$ of boundary layer, dimensionless  |
| $k$                 | wave number, $2\pi f/U$ , cm <sup>-1</sup>   |
| $L_{p_x}$           | typical length scale of wall-pressure fluctuations in x-direction, in.   |
| $L_{p_y}$           | typical length scale of wall-pressure fluctuations in y-direction, in.   |
| $M$                 | Mach number, $U/a$ , dimensionless   |
| $P$                 | steady pressure, lb/sq ft  |
| $\mathcal{P}$       | sum of mean and fluctuating static pressures, $P + p(t)$ , lb/sq ft  |
| $p$                 | static-pressure fluctuation about mean value $P$ , lb/sq ft or dynes/sq cm   |
| $\overline{p^2(f)}$ | mean-square pressure fluctuation per unit bandwidth (as defined by $\overline{p^2} = \int_0^\infty \overline{p^2(f)}df$ ), (lb <sup>2</sup> )(sec)/ft <sup>4</sup> |
| $\tilde{p}(\omega)$ | also written as $\overline{p^2(\omega)} = \frac{1}{2\pi} \overline{p^2(f)}$ , abbreviated notation following Willmarth (ref. 19)                                   |
| $q$                 | dynamic pressure, $\frac{1}{2} \rho U^2$ , lb/sq ft  |
| $R$                 | wall-pressure correlation coefficient (see appendix E), dimensionless  |

|                 |   |
|-----------------|---|
| $R$             | pressure-velocity correlation coefficient (see appendix E), dimensionless   |
| $Re_x$          | Reynolds number based on equivalent distance of boundary-layer development ( $x - x_0$ ) with $x_0 = -2.1$ ft (obtained from $\delta^*$ as a function of $x$ ), dimensionless |
| $Re_\theta$     | Reynolds number based on momentum thickness, dimensionless  |
| $r$             | distance between source point and field point in integrals in eqs. (2), (3), and (9), ft  |
| SPL             | $= 20 \log_{10} \left( \sqrt{p^2}/p_0 \right)$ where $p_0$ is a reference pressure equal to $2 \times 10^{-4}$ dyne/sq cm, db   |
| $t$             | time, sec   |
| $U = U_1$       | longitudinal component of mean velocity (i.e., $\overline{U + u} = \bar{U} \equiv U$ ), ft/sec  |
| $U_\delta$      | longitudinal mean velocity defined as equal to $0.99 U_\infty$ , ft/sec   |
| $u = u_1$       | longitudinal component of turbulent or fluctuating velocity, ft/sec   |
| $V = U_2$       | transverse component of mean velocity ( $V$ assumed to be negligible in boundary layer), ft/sec   |
| $v = v_2$       | transverse component of fluctuating velocity, ft/sec  |
| $W = U_3$       | normal (to wall) component of mean velocity ( $W$ assumed to be negligible in boundary layer), ft/sec   |
| $w = u_3$       | normal (to wall) component of fluctuating velocity, ft/sec  |
| $\underline{x}$ | vector in x-y-z coordinate space, ft  |
| $x = x_1$       | longitudinal coordinate (parallel to wind-tunnel centerline and taken as positive in direction of flow and with $x_1 = 0$ at beginning of test section), ft                   |
| $y = x_2$       | transverse coordinate, ft (or in.)  |
| $z = x_3$       | normal (to wall) coordinate, ft (or in.)  |
| $\beta$         | proportionality constant between root-mean-square wall-pressure fluctuations and local skin-friction coefficient (eq. (5)), dimensionless                                     |
| $\gamma$        | intermittency factor defined as average time that signal is turbulent divided by total time, dimensionless  |
| $\delta$        | boundary-layer thickness, in.   |

$\delta^*$  displacement thickness as defined in ref. 31 (p. 291), in.  
 $\zeta$  separation distances in z-direction, in.  
 $\eta$  separation distances in y-direction, in.  
 $\theta$  momentum thickness as defined in ref. 31 (p. 291), in.  
 $\xi$  relative distances in x-direction, in.  
 $\rho$  density of air, slugs/cu ft  
 $\tau$  time delay (i.e., difference between two instants of time), sec or msec  
 $\omega$  frequency,  $2\pi f$ , radians/sec

Subscripts:

$c$  convection  
 $opt$  refers to value of correlation coefficient and time delay associated with peak in correlation curve that occurs nearest  $\tau = 0$   
 $p$  pressure  
 $s$  refers to value of correlation coefficient and time delay for peak in correlation curve that occurs near  $\tau = -1$  msec  
 $w$  wall  
 $\infty$  free-stream condition  
 $(\_)$  vector

Superscript:

$(\overline{\_})$  time averaged,  $\overline{\alpha} = \lim_{T \rightarrow \infty} \left[ \frac{1}{T} \int_0^T \alpha(t) dt \right]$



## APPENDIX B

### WIND-TUNNEL FACILITY

The wind-tunnel facility was specially designed for the purpose of obtaining the best possible means for the measurement of wall-pressure fluctuations associated with a turbulent boundary layer. The objective was to obtain a good approximation to a two-dimensional turbulent boundary layer of fairly large extent resulting from the flow of a fluid of uniform velocity adjacent to a plane rigid wall. Extraneous noises from sources other than the turbulent-boundary-layer fluctuating pressures should be negligible in comparison with these pressure fluctuations.

The facility shown in figure 1 is a nonreturn continuous-suction type of wind tunnel. The inlet section is rectangular in cross section at all stations. The area contraction of 40 to 1 is from an inlet opening of 4 by 10 feet down to an 8- by 18-inch cross section. The length of the inlet is 6 feet 6 inches. The variation of the cross-sectional area with longitudinal distance  $x$  was based on information presented in reference 40. The commercially available filter units used were 3/32-inch-thick Fiberglas elements. The inlet section was fabricated of 1/8-inch steel and externally ribbed for structural rigidity. The inlet section is shock mounted to a bedplate and concrete floor arrangement (as is the entire facility). The interior of the inlet was coated entirely with a nongloss paint to promote the formation of a thick turbulent boundary layer in spite of the longitudinal pressure gradient favorable for most of the inlet.

The test section is 40 feet long. The entire length is divided into 10 sections, 4 feet in length. One side of the test section is solid 1/2-inch steel, and the other three walls are double-walled. The inner walls consist of porous bronze plates  $9\frac{3}{4}$  by  $24\frac{1}{4}$  by  $\frac{3}{8}$  inch. At the time of installation the joints between the porous plates were sealed with a cement that was sufficiently thick to prevent clogging of porous metal. The outer walls of the doubled-walled sides have flanges for bolting to the solid-wall side. All solid-metal joints were sealed by compressing 3/16-inch-outside-diameter by 1/16-inch-inside-diameter Tygon tubing placed in grooves between the mating parts. Particular attention was paid to the problem of effective sealing at the corners. The joints along the solid test wall were faired and mated to within  $\pm 0.0005$  inch at installation. All sections were doweled together after proper mating had been achieved.

The two 8-inch double-walled sides contain seals that can limit the suction to be effective over only a portion of the 8-inch depth (see fig. 1(b)). The seals (in the 8-in. side walls) were adjusted to conform to the approximate thickness of the boundary layer (developing along the solid wall) from the beginning to the end of the test section. The sealing device consisted of a strip of fairly pliant (sponge) rubber placed between two metal bars nearly spanning the width of space between the double walls. A rod that protruded externally and was fitted with a handle permitted (1) the compression of the rubber strip for sealing and (2) setting the sealing device at a desired position within the double wall.

The flow through the porous walls was drawn off to a bleed manifold through bleed pipes made of reinforced rubber construction (to prevent transmission of vibrations to the test section). There were four bleeds on the first upstream section and two on each of the remaining nine sections. The flow through the bleed pipes was controlled by globe valves. The entire bleed flow was further controlled by a 12-inch butterfly valve downstream of the bleed manifold.

The test section was fitted with static taps as shown in figure 1(b). The 10 original solid sides were fitted with eight ports, each  $1\frac{1}{2}$  inch in diameter, spaced 6 inches apart, in two staggered rows. Subsequently, provision was made to use an additional solid-wall section that replaced any particular original solid-wall section (usually number three as it turned out). This additional section contained three 8-inch ports - one at the center of the section and the other two ports 16 inches to either side. All correlation data required the use of this solid-wall section since it was desired to mount the pressure transducers and hot-wire probe within one large port.

Considerable attention was paid to shock mounting the inlet and test-section portions of the wind tunnel. In addition to shock mounting to prevent vibrations from being transmitted through the vertical supporting structure, the test section was isolated from the downstream portion of the tunnel structure. A rubber joint, placed between the test section and the control section, served as an expansion joint and reduced considerably the vibrations that might exist downstream of the test section.

The control section contained a block constricting the area and thus controlling the Mach number in the test section depending on the portion of the area constricted. This control block was placed on the 18-inch porous wall side. Downstream of the control section are the diffuser sections followed by the valve and piping leading to the laboratory exhaust machinery.

The wind-tunnel instrumentation for obtaining the stagnation pressure and temperature consisted of, respectively, a standard aneroid barometer stationed some distance upstream of the inlet and four iron-constantan thermocouples located in a plane just downstream of the filters in the inlet. The static pressures along the test section were obtained from static taps placed in the solid wall of the test section 6 inches apart in two rows, each 3 inches from the longitudinal centerline. The total pressure very near the centerline of the flow was measured with the use of the total-pressure probe and directly read on a U-tube water manometer (referenced to atmospheric pressure). By using static taps the pressure drop across the control block was continuously monitored. The wind-tunnel instrumentation includes for each bleed line a U-tube water manometer that measures and thus allows control of the flow (from the porous wall) in the bleed lines. These 100-inch U-tube manometers are installed in banks of six each at convenient intervals near the porous-bleed globe-valve controls. The pressure difference measured with U-tube manometers was the pressure drop across the porous wall obtained as the difference of the static pressure in the wind tunnel and the static pressure in the space between the double walls. For each U-tube the wind-tunnel static pressure was taken from a static tap at the appropriate station, and the other pressure was obtained from a static tap in the outer (solid) wall of the double-walled sides.

The setup and calibration procedure included (1) the establishment of the optimum settings of the globe valve for maximum suction of the low-velocity air from the porous wall sides and/or optimum control of the average longitudinal static-pressure gradient and (2) the establishment of suitable settings for adjustable seals in both of the 8-inch porous wall sides. A measurement was made of the boundary-layer thickness at the leading edge of the test section. Based on this value, values of boundary-layer thicknesses were estimated for a number of downstream stations. The empirical law used in the calculation was based on the one-seventh power law velocity distribution in the boundary layer. The adjustable seals were then set accordingly as a first approximation.

Subsequently, a trial-and-error procedure was used to obtain the globe-valve settings and 12-inch butterfly valve setting that yielded a zero static-pressure gradient of  $\pm 1$  inch of water for the entire test section. The pressure drops across the porous wall finally used were everywhere less than 35 inches of water. This procedure was done with a control block installed that gave a nominal Mach number of 0.6. Once the globe-valve settings had been made, the valve handles were wired together in position. A slight reduction in total flow through the porous wall (by closing slightly the 12-in. butterfly valve from its position for zero static-pressure longitudinal gradient in the wind tunnel) results in a change in the wind-tunnel static pressures such that the static-pressure variation with the longitudinal distance is very nearly linear and the gradient a favorable one. Conversely, slightly opening the 12-inch valve results in an essentially linear longitudinal pressure distribution with the gradient being adverse. The final values of the porous-wall boundary-layer thicknesses  $\delta$  ranged from 0.3 inch at  $x = 0$  almost linearly to 2.5 inches at  $x = 20$  feet and about 3.8 inches at  $x = 40$  feet. Actually, for the last 4 to 6 feet of test section the two opposing wall boundary layers were considered to be essentially in the process of merging into a channel-type flow.

The last step in determining if the wind tunnel was suitable for making measurements of the type intended was to measure the noise field external to the wind tunnel, particularly in the area of the inlet opening and near the test-section walls. The measurements were made with a condenser microphone. The results of these measurements and their implications are presented in the text.

## APPENDIX C

### DESCRIPTION AND CALIBRATION OF PRESSURE TRANSDUCERS

In the present experiments the commercially available capacity-type transducers (ref. 41) were used, and a series of piezoelectric ceramic transducers suitable for the envisioned tasks was developed. The capacity-type transducers, referred to as condenser transducers in the main text, will be described first.

The surface of the 21BR-150-5 microphone, which admits the pressure fluctuations, is a fine, sintered bronze screen. The diameter of the microphone effective or sensitive to pressure fluctuations has been estimated to be 0.43 inch, although the clamped plate diameter of 0.50 inch could have been used in the  $d/8^*$  experiments without appreciable effect. The surface of the 21BR-150-6 is of polished stainless steel with a single hole of 0.040 inch.

The installation of both condenser transducers into the solid wall was accomplished by inserting the microphone and base into a port as shown in figure 2(d). The design of the port included the requirements of pressure sealing against the pressure difference existing across the wind-tunnel wall and the function of pressure equalization for the transducer. The pressure seals were two O-rings as shown in figure 2(d). The equalization of the pressures between the boundary layer and the vent space was accomplished by drilling into the brass condenser-transducer adapter-port four small holes spaced circumferentially about the condenser transducer (see A in fig. 2(d)). Pressure equalization between the vent space and the interior of the base was also accomplished by drilling four small holes into the aluminum casing of the base. A static tap, 0.0625 inch in diameter, was also drilled downstream of the condenser transducer to measure the mean static pressure very near it. A static tap into the vent space also permitted measurement of the vent pressure during the experiments. In order to use the previously described method of pressure sealing and equalization, it was necessary to modify the base.

To obtain usable piezoelectric pressure transducers, it was believed at the beginning that Willmarth's improved barium titanate pressure transducer (ref. 42) could simply be copied. However, in order to get a much smaller separation distance between two pressure transducers, it was necessary to eliminate from consideration the extended radial dimensions required by the vibration-isolating structure of the pressure transducer. However, from Willmarth's earlier results (ref. 43) it was assumed that, in order to use a transducer with an axially polarized barium titanate ceramic element, it would have to be isolated from vibration to minimize as much as possible the electric signals that occur as a result of the deformation of the vibrating elements. This would have particularly been a problem in the present case because the intent was to use an element of smaller diameter, 0.125 inch or smaller, if possible. The desired smaller diameters would have resulted in a reduced sensitivity to pressure pulses. Consequently, the signal-to-noise ratio for the desired transducer would even be smaller.

Considerable time was spent in experimentation with various shapes and types of piezoelectric ceramic elements and with ways of mounting them without vibration-isolation such that a signal-to-noise (where the noise is defined as those signals due to vibration and/or other extraneous sources that would interfere with measuring the desired signal) ratio of 10 decibels or greater was achieved. The method for checking this was simply to compare the measured spectral distribution of the output from the amplifier with the transducer being subjected to wall-pressure fluctuations with that obtained for the transducer not exposed to wall-pressure fluctuations. This is accomplished by installing the transducer at the same station in blind adapter ports that were constructed such that they were of essentially the same shape and mass, but did not allow the boundary-layer wall-pressure fluctuations to come directly into contact with the piezoelectric transducer. If at any frequency the difference in the two spectral distributions was less than 10 decibels for several tests, the transducer was rejected.

Finally, several piezoelectric transducers of a particular design consistently passed the test just referred to. These and others like this type were used for all the measurements taken with the piezoelectric transducers. The transducers consist of a capped annular piezoelectric element. The design is a modification of one for a high-frequency transducer designed to measure pressure pulses such as those in shock tubes (unpublished NASA data by R. A. Yocke). Sketches giving the details of construction of the transducers are shown in figures 2(a) to (c) with piezoelectric elements of diameters of 0.125, 0.0625, and 0.250 inch, respectively. The piezoelectric ceramic used for these transducers is PZT-5, a polycrystalline modified lead-zirconate-titanate ceramic, developed and manufactured by the Clevite Corporation. The material is considered to be superior to Barium Titanate Ceramic "B" (also manufactured by Clevite Corp.) in that the coupling coefficients and piezoelectric constants are approximately twice as great.

The shape of the piezoelectric elements used is an annular circular cylinder of the radially polarized length expander type. When compressed or expanded axially, a charge is developed on the inner and outer silvered surfaces of the annulus. This charge is proportional to the amount of deformation. The cap on the end of the element greatly increases the area on which forces may act. In the case of wall-pressure fluctuation transducers, an end cap is vital in order not to disturb the boundary-layer flow.

The manner of making the pressure transducer can be illustrated, for example, by referring to figure 2(a). The center copper lead wire is inserted through the Polypenco insulator with a tight fit, and in turn this assembly is inserted with a tight fit into the brass body. A groove, 0.010 inch in depth, is put into the Polypenco, and the PZT-5 element is cemented in place with Cox Number 28 cement. Prior to cementing on the cap of 0.010-inch-thick Polypenco, conductive silver paint was carefully put on top of the Polypenco insulator making good contact with the copper lead wire and the inside surface of the PZT-5 element at its base. The cap was then cemented in place. The outer surface of the PZT-5 element was grounded as near as possible to its base with conductive silver paint. At the other end of the transducer the annular space between the copper wire and brass body was filled up by ceramic beads and Cox Number 28

cement except at the very end. Here, through a side-drilled access hole the copper wire was soft-soldered to a Microdot Connector Number 3103, which was already threaded into the brass body and soldered externally (and thus grounded). The one transducer with a 0.0625-inch-diameter PZT-5 element (fig. 2(b)) was made similar to that with the 0.125-inch-diameter elements (fig. 2(a)). The brass body of the transducer with the 0.250-inch element (fig. 2(c)) differed from the other ones; otherwise the transducer was essentially the same.

The parts of the construction process that were quite critical obviously involved the PZT-5 element, its placement, and electrical contact with other parts of the transducer. Among the several dozen transducers made were some that exhibited erratic behavior and quite low sensitivity to pressure fluctuations (and a resulting surprising response to vibrations). In practically every case it appeared that the PZT-5 element had not been properly positioned in the Polypenco groove, and the conductive silver paint had either been insufficiently applied or excessively so. All the piezoelectric transducers used in the results reported in the text were carefully selected. In the case of the pairs used for correlation of the wall-pressure fluctuations, they were carefully matched. The transducers were calibrated by the methods indicated in appendix D.

The amplifier used in connection with the piezoelectric transducers was a Decade Isolation Amplifier, Model 102B, manufactured by Keithley Instruments, Inc. It has a high input impedance, low output impedance, and very accurate gains in steps of 20 up to 60 decibels, which was the gain setting used. The bandwidth setting used gave usable response from 2 to 150 kcps. The response was often checked from 30 to 50,000 cps and was found to be flat within  $\pm 0.2$  decibels. The transducers were connected to the Keithley amplifiers by means of 18-inch cables with a Microdot Connector Number 3221 on one end and an Amphenol Connector on the other end that was connected to a Keithley 102B-P1 Probe on the input to the amplifier. The cables were made from Microdot Low-Noise Cable Number 50-3804.

The transducers were installed either into the 8-inch port where pairs were used for correlations or into smaller ports,  $1\frac{1}{2}$  inches in diameter. As pointed out previously, no means of vibration isolation was provided since it was not needed. The transducers were held fixed in place by standard hex-head nuts. Pressure sealing was simply achieved by applying a quick-drying paint where the transducer brass body emerged from the ports.

Calibrations of the amplitude response as a function of frequency were made for all the pressure transducers used in the experiments. The same methods were used for the condenser transducers as for the piezoelectric transducers. To cover as broad a range of frequencies as possible, two different types of calibrations were made for each transducer. One type covered the lower frequency range, and the other covered the higher frequency range. These calibrations were performed with the transducer systems set up and operating precisely as in the experiments. The shock-tube calibration of the piezoelectric transducers was not used, as this would yield only an average sensitivity over the broad frequency

range of response and give a value for the corner frequency. In addition, it would not be a particularly suitable method for calibrating the condenser transducers. Reciprocity techniques (ref. 44) for calibration of the transducers were not considered particularly useful because of the lower sensitivities of the piezoelectric system.

Over the lower frequency range, 30 to 10,000 cps, the transducers were pressure calibrated with the use of an Altec-Lansing acoustic calibrator. In the higher frequency range, 2000 to 20,000 cps, the response was obtained from comparison calibrations with a calibrated W.E. 640AA microphone as a standard.

To perform the latter calibration it was necessary to construct an anechoic chamber (5 by 5 by 5 ft) suitable for frequencies greater than 2000 cps. The source used for the sonic and ultrasonic signals was a high-frequency driver powered by a suitable amplifier. The source was extended vertically upward into the chamber along the identical axis of the transducers pointing downward. The functioning of the chamber as an anechoic one was briefly checked along the axis of interest and was found to be satisfactory over the needed range of frequencies. Considerable care was taken to duplicate conditions as precisely as possible for all the calibration tests.

The results of the calibration are presented in figures 3(a) to (e). Figures 3(a) to (c) are for piezoelectric transducers ZR, ZS, and ZT, respectively; figures 3(d) and (e) for the condenser transducers CA and CB, respectively. The calibrations presented in figures 3(a), (d), and (e) are for transducers that were used in the measurements of magnitude and spectral distribution of the wall-pressure fluctuations. The calibrations in figures 3(a) to (c) are for transducers that were used in an experiment to determine the effect of  $d/\delta^*$  (keeping  $\delta^*$  constant) on the magnitude and spectral distribution. The calibration presented in figure 3(b) is for a piezoelectric transducer of the type used in the wall-pressure correlations. The calibrations in figures 3(a) and (e) are for the transducers used to measure wall-pressure fluctuations for the pressure-velocity correlations.

Before and after experimental surveys the level of sensitivity of the entire transducer system was checked with a sound-level calibrator at a frequency of 400 cps, and good agreement was obtained with the values from the calibration curves ( $\pm 0.2$  db).

No corrections were made for temperature changes or static-pressure changes from standard conditions. As reference 45 points out, the piezoelectric transducer having a high mechanical impedance is unaffected by changes in static pressure. While the same statement cannot be specifically made for the condenser transducers, from figure 2 of reference 46, which shows the pressure effect on a W. E. 640AA microphone (similar to the 21BR series), the effect of a change in pressure from 30 to 22 inches of mercury is a change of about 0.2 decibel in response over most of the range of frequencies.

## APPENDIX D

### HOT-WIRE ANEMOMETER MEASUREMENTS

The hot-wire element used to sense the flow fluctuations was a tungsten wire with a diameter of  $2 \times 10^{-4}$  inch and an unplated or sensitive length of 0.080 inch. The hot-wire anemometer used herein is the constant-temperature anemometer described in references 24 to 26. The amplifier used in the present experiments is the improved version with regard to frequency response (see ref. 47). The frequency response of the entire system including amplifier, bridge, wire, and cables is flat within 1 decibel from 0 to 100,000 cps.

The measurements taken with the hot-wire anemometer were analyzed using the empirical relation between heat loss and mass flow for small electrically heated cylinders:

$$\frac{i^2 R}{R - R_a} = A + B \sqrt{\rho U} \quad (D1)$$

where  $i$  and  $R$  (in this appendix only) are the wire current and resistance, respectively, for the mass flow  $\rho U$ ,  $R_a$  is the resistance of the wire at some reference temperature, that is, temperature of the surrounding airflow, and  $A$  and  $B$  are experimental constants to be determined for each wire. An equation of the form of (D1) was first theoretically derived by King (ref. 48) as the heat loss from small circular cylinders in potential flows. This empirical relation, while obviously not accounting for the viscous effects in the flow about cylinders, has been justified in general by the experimental results. The exceptions to its validity generally arise in rarefied-gas flows where the mean-free path becomes of the same order as the wire diameter (Knudsen number effects) or at supersonic speeds (Mach number effects). The hot-wire measurements are for Knudsen numbers greater than 0.01 and Reynolds numbers (referring to the wire diameter) greater than 25. According to figure 2(a) of reference 49, for this range of parameters it is permissible to say that the slip-flow problem is negligible. In addition, the small deviation from 0.5 of the exponent of the King's equation (referred to in ref. 50) does not have any real significance for this range of parameters providing that essentially the constants  $A$  and  $B$  are obtained experimentally for each wire. This was the procedure used. The development of the sensitivity equations is presented in appendix F of reference 24. The fluctuating mass flow is shown to be given by

$$\frac{\Delta(\rho U)}{\bar{\rho U}} = \frac{4 \frac{\Delta e}{e}}{\left[1 - \left(\frac{e_0}{e}\right)\right]^2} \quad (D2)$$

where

$$\frac{\Delta(\rho U)}{\bar{\rho U}} = \frac{(\rho U) - (\bar{\rho U})}{(\bar{\rho U})}$$



$e$  is the instantaneous electrical voltage, and  $e_o$  is the voltage across the wire at no flow. From  $\frac{d(\rho U)}{\rho U} = \frac{d\rho}{\rho} + \frac{dU}{U}$ ,

$$\frac{\Delta(\rho U)}{\rho U} \approx \frac{\Delta U}{U} \quad (D3)$$

provided that the density fluctuations can be safely assumed to be negligible (in comparison with the velocity fluctuations). This is certainly the case in the present experiments since maximum Mach numbers encountered are approximately 0.60 (as the free stream is approached) and also since the look of any heated boundaries in the flow suggests that the temperature fluctuations are negligible.

The ratio of fluctuating velocity to the stream velocity  $\bar{U}_\infty$  was determined by the relation

$$\frac{\Delta U}{\bar{U}_\infty} = \frac{\bar{U}}{\bar{U}_\infty} \frac{\Delta U}{\bar{U}} \quad (D4)$$

where  $\bar{U}/\bar{U}_\infty$  was determined from the boundary-layer pitot-tube measurements or from the hot-wire measurements and the free-stream aerodynamic measurements as

$$\frac{(\bar{\rho U})}{(\bar{\rho U})_\infty} = \frac{\left[ \left( \frac{\bar{e}}{e_o} \right)^2 - 1 \right]^2}{\left[ \left( \frac{\bar{e}_\infty}{e_o} \right)^2 - 1 \right]^2} \quad (D5)$$

and

$$\frac{\bar{U}}{\bar{U}_\infty} = \frac{\frac{(\bar{\rho U})}{(\bar{\rho U})_\infty}}{\frac{\rho}{\rho_\infty}} \quad (D6)$$

where  $\rho/\rho_\infty$  can be readily calculated from a knowledge of the free-stream Mach number  $M_\infty$  and aerodynamic flow tables such as those in reference 51.

Equations (D5) and (D6) were used to calculate the data of figures 36(e) to (i), which give representative values of  $\sqrt{u^2}/U_\infty$  and  $z$  obtained during the experiments designed to measure the correlations of the wall-pressure fluctuations with the velocity fluctuations in the boundary layer.

The wires were calibrated by noting the direct-current bridge voltage under free-stream airflow conditions and zero-flow conditions. The direct-current voltages were measured by reading the voltage drop across a known wire-wound resistor. The fluctuating voltage was measured in terms of its root-mean-square value by using a true-root-mean-square meter.

The positions of the hot-wire probe were indicated automatically by the electrically operated probe actuator and also with a dial indicator used to measure positions near the wall to within  $\pm 0.005$  inch. The reference position of the hot-wire probe was determined by allowing the probe to be slowly actuated toward the wall until one or both of the prong tips actually touched the wall and made electrical contact with it. Electrical contact with the wall was determined from the meters indicating the direct-current component of bridge voltage. Usually the current supplied to the wire would suddenly increase, and the anemometer system would automatically switch off current delivery to the wire; then the anemometer controls were reset (after moving the hot wire away from wall) to admit electrical current to the wire.

## APPENDIX E

### SPACE-TIME CORRELATION MEASUREMENTS

The space-time correlation measurements are concerned with the determination of a coefficient that can be mathematically expressed as

$$R(\underline{x}_g - \underline{x}_h, \tau) = \frac{1}{\{[e_1(\underline{x}_g, t)]^2 [e_2(\underline{x}_h, t + \tau)]^2\}^{1/2}} \lim_{T \rightarrow \infty} \left[ \frac{1}{T} \int_0^T e_1(\underline{x}_g, t) e_2(\underline{x}_h, t + \tau) dt \right]$$

where  $e_1$  and  $e_2$  are the fluctuating electrical voltages recorded (at a tape speed of 15 in./sec) on channels 1 and 2, respectively, of the tape recorder and where  $\underline{x}_g$  and  $\underline{x}_h$  are, respectively, the position vectors of the points at which these measurements are taken. In all the correlation measurements  $e_1$  was obtained from a transducer sensing wall-pressure fluctuations; for the space-time correlations of wall-pressure fluctuations,  $e_2$  also represented a wall-pressure fluctuation. For the correlations of the wall-pressure fluctuations with the velocity fluctuations,  $e_2$  represents the velocity fluctuation. When an auto-correlation measurement was made,  $e_1$  and  $e_2$  originated from the same transducer ( $e_1 \equiv e_2$  and  $\underline{x}_g \equiv \underline{x}_h$ ). The time delay  $\tau$  to which the electrical voltage  $e_2$  is subjected is obtained upon playback of the recorded signals. This was done by using a tape recorder fitted with a set of magnetic heads such that the head for channel 2 can be moved in translation parallel to the direction of tape motion (relative to the magnetic head for channel 1). The motion of the movable head was controlled and measured by a micrometer head with a maximum accuracy of  $1 \times 10^{-4}$  inch by means of the vernier of the micrometer.

The electrical voltages  $e_1$  and  $e_2$  were then amplified properly and multiplied electronically. The output of the analog electronic multiplier and the output of a linear, infinite resolution potentiometer attached to the movable magnetic head are connected to inputs of an X-Y recorder. The micrometer head was moved manually to ensure as careful as possible plotting of the particular correlation coefficient as a function of  $\tau$ . Whenever necessary, the curve was retraced as many times as required.

The correlation computer, which is described in greater detail in reference 52, is included in the block diagrams presented in figure 5. The amplitude response as a function of frequency of the entire tape recording system through correlation computer system was constantly calibrated and checked, and its response was flat  $\pm 2$  decibels (referenced to 1000 cps) from 30 to 15,000 cps. The maximum correlation coefficients obtained for a sine wave signal recorded on both channels of the magnetic tape (autocorrelation of sine waves) gave the results shown in the following brief table:

| f,<br>cps | R          | f,<br>cps | R          | f,<br>cps | R          |
|-----------|------------|-----------|------------|-----------|------------|
| 100       | $\pm 1.00$ | 1000      | $\pm 1.00$ | 10,000    | $\pm 0.96$ |
| 400       | $\pm 1.00$ | 4000      | $\pm .99$  | 12,000    | $\pm .94$  |
| 700       | $\pm 1.00$ | 7000      | $\pm .98$  | 15,000    | $\pm .93$  |

Variable high-pass and low-pass electronic filters were used to reject various portions of the spectrum for a limited number of the correlations to determine the effect of rejecting part of the frequency range of the fluctuating signals.

## REFERENCES

1. Lighthill, M. J.: On Sound Generated Aerodynamically. I - General Theory. Proc. Roy. Soc. (London), ser. A, vol. 211, no. 1107, Mar. 20, 1952, pp. 564-587.
2. Lighthill, M. J.: On Sound Generated Aerodynamically. II - Turbulence as a Source of Sound. Proc. Roy. Soc. (London), ser. A, vol. 222, no. 1148, Feb. 23, 1954, pp. 1-32.
3. Ribner, H. S.: A Theory of the Sound from Jets and Other Flows in Terms of Simple Sources. Rep. 67, Inst. Aerophys., Univ. Toronto, July 1960.
4. Proudman, I.: The Generation of Noise by Isotropic Turbulence. Proc. Roy. Soc. (London), ser. A, vol. 214, no. 1116, Aug. 7, 1952, pp. 119-132.
5. Mawardi, Osman K.: On the Spectrum of Noise from Turbulence. Jour. Acoustical Soc. Am., vol. 27, no. 3, May 1955, pp. 442-445.
6. Meecham, W. C., and Ford, G. W.: Acoustic Radiation from Isotropic Turbulence. Jour. Acoustical Soc. Am., vol. 30, no. 4, Apr. 1958, pp. 318-322.
7. Curle, N.: The Influence of Solid Boundaries Upon Aerodynamic Sound. Proc. Roy. Soc. (London), ser. A, vol. 231, no. 1187, Sept. 20, 1955, pp. 505-513.
8. Phillips, O. M.: On the Aerodynamic Surface Sound from a Plane Turbulent Boundary Layer. Proc. Roy. Soc. (London), ser. A, vol. 234, no. 1198, Feb. 21, 1956, pp. 327-335.
9. Doak, P. E.: Acoustic Radiation from a Turbulent Fluid Containing Foreign Bodies. Proc. Roy. Soc. (London), ser. A, vol. 254, no. 1276, Jan. 19, 1960, pp. 129-145.
10. Powell, Alan: On the Aerodynamic Noise of a Rigid Flat Plate Moving at Zero Incidence. Jour. Acoustical Soc. Am., vol. 31, no. 12, Dec. 1959, pp. 1649-1653.
11. Powell, Alan: Aerodynamic Noise and the Plane Boundary. Jour. Acoustical Soc. Am., vol. 32, no. 8, Aug. 1960, pp. 982-990.
12. Heisenberg, W.: Zur statistischen Theorie der turbulenz. Zs. f. Phys., bd. 124, heft 7/12, 1948, pp. 628-657.
13. Batchelor, G. K.: Pressure Fluctuations in Isotropic Turbulence. Proc. Cambridge Phil. Soc. pt. 2, vol. 47, Apr. 1951, pp. 359-374.
14. Kraichnan, Robert H.: Pressure Field Within Homogeneous Anisotropic Turbulence. Jour. Acoustical Soc. Am., vol. 28, no. 1, Jan. 1956, pp. 64-72.

15. Kraichnan, Robert H.: Pressure Fluctuations in Turbulent Flow Over a Flat Plate. Jour. Acoustical Soc. Am., vol. 28, no. 3, May 1956, pp. 378-390.
16. Lilley, G. M., and Hodgson, T. H.: On Surface Pressure Fluctuations in Turbulent Boundary Layers. Note 101, The College of Aero. (Cranfield), 1960. (See also Revised Rep. 276, AGARD, Apr. 1960.)
17. Lilley, G. M.: Pressure Fluctuations in an Incompressible Turbulent Boundary Layer. Rep. 133. The College of Aero. (Cranfield), June 1960.
18. Harrison, Mark: Pressure Fluctuations on the Wall Adjacent to a Turbulent Boundary Layer. Rep. 1260, David Taylor Model Basin, Dec. 1958.
19. Willmarth, W. W.: Space-Time Correlations and Spectra of Wall Pressure in a Turbulent Boundary Layer. NASA MEMO 3-17-59W, 1959.
20. Skudrzyk, E. J., and Haddle, G. P.: Noise Production in a Turbulent Boundary Layer by Smooth and Rough Surfaces. Jour. Acoustical Soc. Am., vol. 32, no. 1, Jan. 1960, pp. 19-34.
21. Tack, D. H., Smith, M. W., and Lambert, R. F.: Wall Pressure Correlations in Turbulent Airflow. Jour. Acoustical Soc. Am., vol. 33, no. 4, Apr. 1961, pp. 410-418.
22. Von Winkle, William Anton: Some Measurements of Longitudinal Space-Time Correlations of Wall Pressure Fluctuations in Turbulent Pipe Flow. Inst. Eng. Res., Univ. Calif., Sept. 1961.
23. Ludwig, H., and Tillmann, W.: Investigations of the Wall-Shearing Stress in Turbulent Boundary Layers. NACA TM 1285, 1950.
24. Laurence, James C., and Landes, L. Gene: Auxiliary Equipment and Techniques for Adapting the Constant-Temperature Hot-Wire Anemometer to Specific Problems in Air-Flow Measurements. NACA TN 2843, 1952.
25. Laurence, James C.: Intensity, Scale, and Spectra of Turbulence in Mixing Region of Free Subsonic Jet. NACA Rep. 1292, 1956. (Supersedes NACA TN's 3561 and 3576.)
26. Sandborn, Virgil A.: Experimental Evaluation of Momentum Terms in Turbulent Pipe Flow. NACA TN 3266, 1955.
27. Schlichting, Hermann: Boundary Layer Theory. McGraw-Hill Book Co., Inc., 1955.
28. Klebanoff, P. S.: Characteristics of Turbulence in a Boundary Layer with Zero Pressure Gradient. NACA Rep. 1247, 1955. (Supersedes NACA TN 3178.)
29. Corcos, G. M., Cuthbert, J. W., and Von Winkle, W. A.: On the Measurement of Turbulent Pressure Fluctuations with a Transducer of Finite Size. Inst. Res. Eng., Univ. Calif., Nov. 1959.

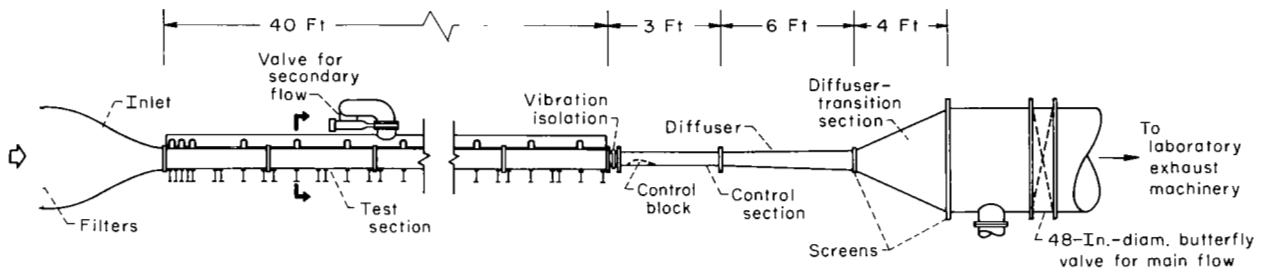
30. Townsend, A. A.: The Structure of Turbulent Shear Flow. Cambridge Univ. Press, 1956, p. 27.
31. Corrsin, Stanley, and Kistler, Alan L.: Free-Stream Boundaries of Turbulent Flows. NACA Rep. 1244, 1955. (Supersedes NACA TN 3133.)
32. Favre, A. J., Gaviglio, J. J., and Dumas, R.: Space-Time Double Correlations and Spectra in a Turbulent Boundary Layer. Jour. Fluid Mech., pt. 4, vol. 2, June 1957, pp. 313-342.
33. Richards, E. J., Bull, M. K., and Willis, J. L.: Boundary Layer Noise Research in the U.S.A. and Canada: A Critical Review. Rep. 21,766, British ARC, Feb. 1960.
34. Dryden, Hugh L., Schubauer, G. B., Mock, W. C., Jr., and Skramstad, H. K.: Measurements of Intensity and Scale of Wind-Tunnel Turbulence and Their Relation to the Critical Reynolds Number of Spheres. NACA Rep. 581, 1937.
35. Limber, D. N.: Numerical Results for Pressure-Velocity Correlations in Homogeneous Isotropic Turbulence. Proc. Nat. Acad. Sci., vol. 37, 1951, p. 230.
36. Hinze, J. O.: Turbulence. McGraw-Hill Book Co., Inc., 1959, p. 252.
37. Batchelor, G. K.: The Theory of Homogeneous Turbulence. Cambridge Univ. Press, 1956.
38. MacColl, LeRoy A.: Fundamental Theory of Servomechanisms. D. Van Nostrand Co., Inc., 1945.
39. Favre, A. J., Gaviglio, J. J., and Dumas, R. J.: Further Space-Time Correlations of Velocity in a Turbulent Boundary Layer. Jour. Fluid Mech., pt. 4, vol. 3, Jan. 1958, pp. 344-356.
40. Smith, Richard H., and Wang, Chi-Teh: Contracting Cones Giving Uniform Throat Speeds. Jour. Aero. Sci., vol. 11, no. 4, Oct. 1944, pp. 356-361.
41. Hilliard, John K., and Fiala, Walter T.: Condenser Microphones for Measurement of High Sound Pressures. Jour. Acoustical Soc. Am., vol. 29, no. 2, Feb. 1957, pp. 254-260.
42. Willmarth, W. W.: Small Barium Titanate Transducer for Aerodynamic or Acoustic Pressure Measurements. Rev. Sci. Instr., vol. 29, no. 3, Mar. 1958, pp. 218-222.
43. Willmarth, William W.: Wall-Pressure Fluctuations in a Turbulent Boundary Layer. Jour. Acoustical Soc. Am., vol. 28, no. 6, Nov. 1956, pp. 1048-1053.
44. Beranek, Leo L.: Acoustics. McGraw-Hill Book Co., Inc., 1954.

45. Massa, Frank: Comments on "Pressure Response of Condenser Microphones at Low Ambient Pressures." Jour. Acoustical Soc. Am., vol. 33, no. 6, June 1961, p. 810.
46. Chalupnik, James D., Rule, Eric, and Suellentrop, Fred J.: Pressure Response of Condenser Microphones at Low Ambient Pressures. Jour. Acoustical Soc. Am., vol. 33, no. 2, Feb. 1961, pp. 177-178.
47. Sandborn, Virgil A., and Slogar, Raymond J.: Study of the Momentum Distribution of Turbulent Boundary Layers in Adverse Pressure Gradients. NACA TN 3264, 1955.
48. King, Louis Vessot: On the Convection of Heat from Small Cylinders in a Stream of Fluid: Determination of the Convection Constants of Small Platinum Wires with Applications to Hot-Wire Anemometry. Proc. Roy. Soc. (London), ser. A, vol. 214, no. 14, Nov. 1914, pp. 373-432.
49. Baldwin, L. V., Sandborn, V. A., and Laurence, J. C.: Heat Transfer from Transverse and Yawed Cylinders in Continuum, Slip, and Free Molecule Air Flows. Jour. Heat Transfer, ser. C, vol. 82, no. 2, May 1960, pp. 77-86.
50. Baldwin, Lionel V.: Turbulent Diffusion in the Core of Fully Developed Pipe Flow. Ph.D. Thesis, Case Inst. Tech., 1959.
51. Ames Research Staff: Equations, Tables, and Charts for Compressible Flow. NACA Rep. 1135, 1953. (Supersedes NACA TN 1428.)
52. Carlson, E. R., et al.: Special Electronic Equipment for the Analysis of Statistical Data. Proc. IRE, vol. 47, no. 5, May 1959, pp. 956-962.

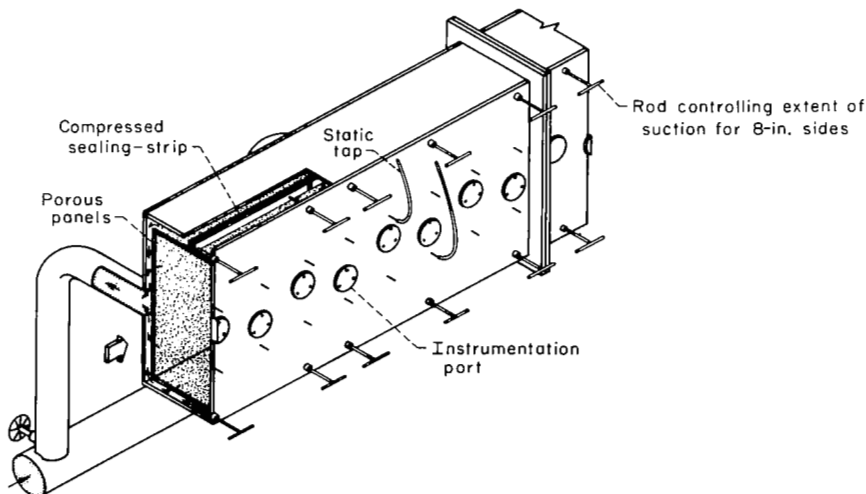


TABLE I. - LIST OF PRESSURE TRANSDUCERS

| Type of transducer | Diameter of sensing area, in. | Commercial designation | Alpha-betic designation | Type of measurement        |
|--------------------|-------------------------------|------------------------|-------------------------|----------------------------|
| Condenser          | 0.43                          | Altec-Lansing BR 150-5 | CA                      | Wall-pressure fluctuations |
| Condenser          | .040                          | Altec-Lansing BR 150-6 | CB                      |                            |
| Piezoelectric      | .0625                         | -----                  | ZR                      |                            |
|                    | .125                          | -----                  | ZS                      |                            |
|                    | .250                          | -----                  | ZT                      |                            |
|                    | .125                          | -----                  | ZD                      |                            |
|                    |                               | -----                  | ZG                      |                            |
|                    |                               | -----                  | ZH                      |                            |
|                    |                               | -----                  | ZI                      |                            |
|                    |                               | -----                  | ZJ                      |                            |
|                    |                               | -----                  | ZN                      |                            |
|                    |                               | -----                  | ZP                      |                            |

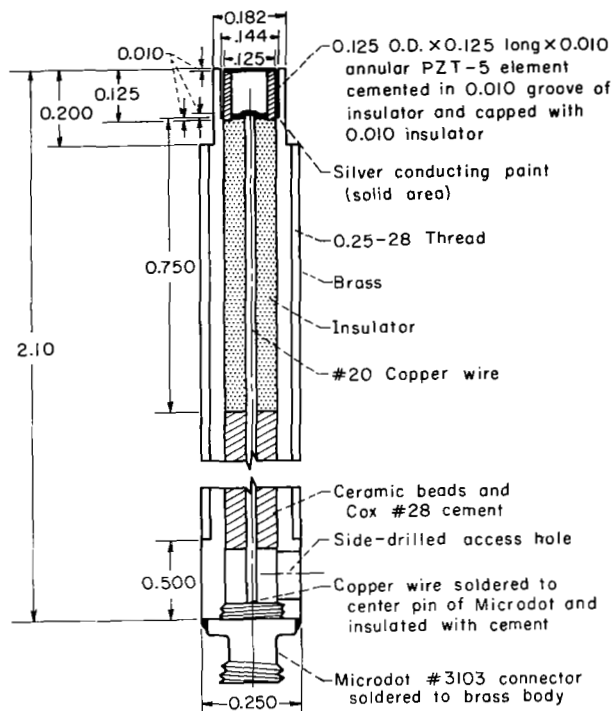


(a) Complete wind tunnel.

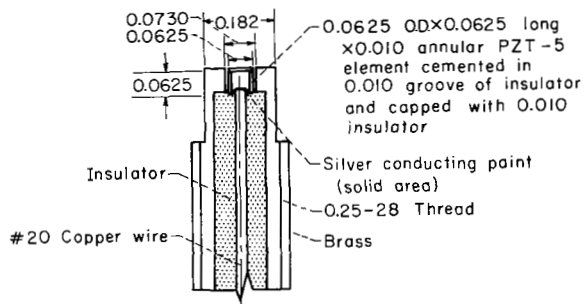


(b) Test-section detail.

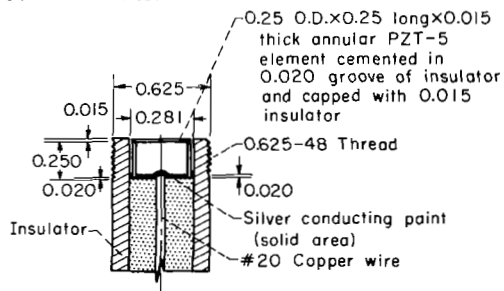
Figure 1. - Wind-tunnel facility.



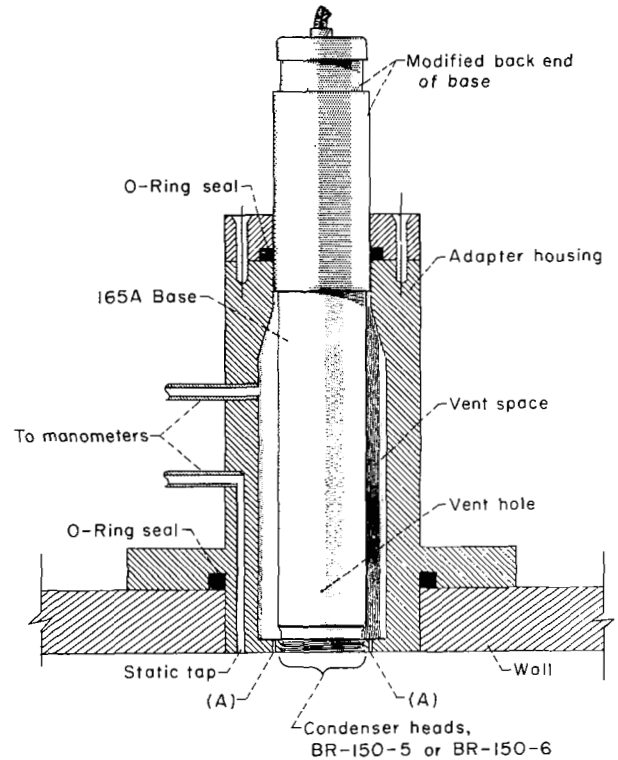
(a) Piezoelectric transducer with 0.125-inch PZT-5 element for wall-pressure fluctuations. (Dimensions are in inches.)



(b) Piezoelectric transducer with 0.0625-inch PZT-5 element for wall-pressure fluctuations. (Dimensions are in inches.)



(c) Piezoelectric transducer with 0.25-inch PZT-5 element for wall-pressure fluctuations. (Dimensions are in inches.)



(d) Condenser transducer installed for wall-pressure fluctuations.

Figure 2. - Transducers used to measure fluctuating pressures.

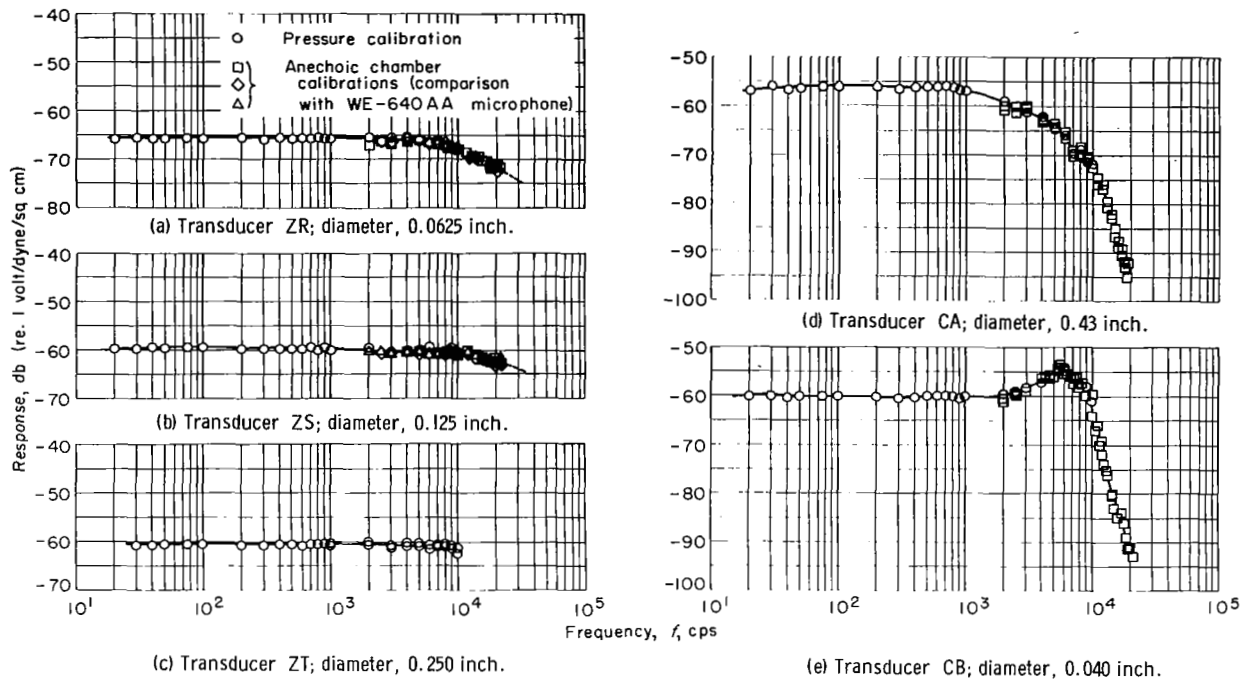


Figure 3. - Measured response of transducers used in experiments.

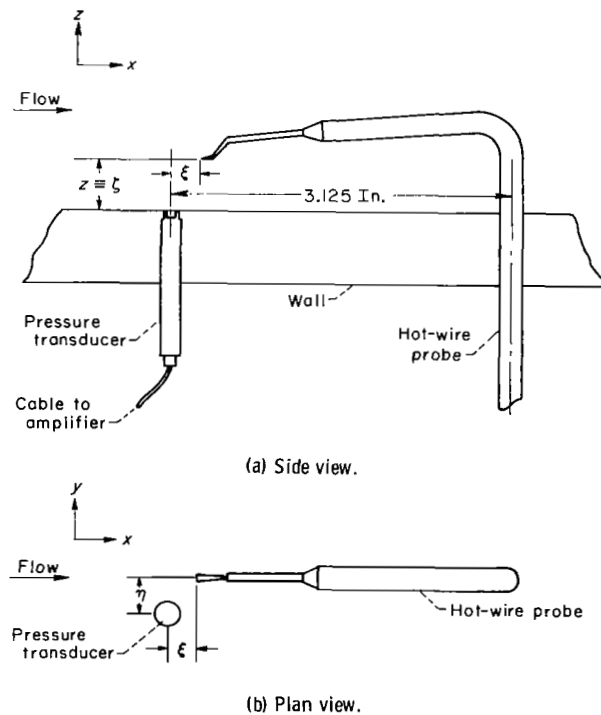
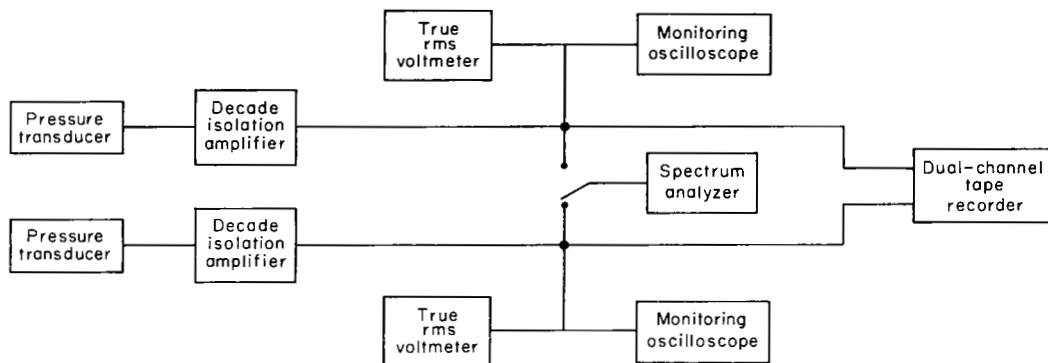
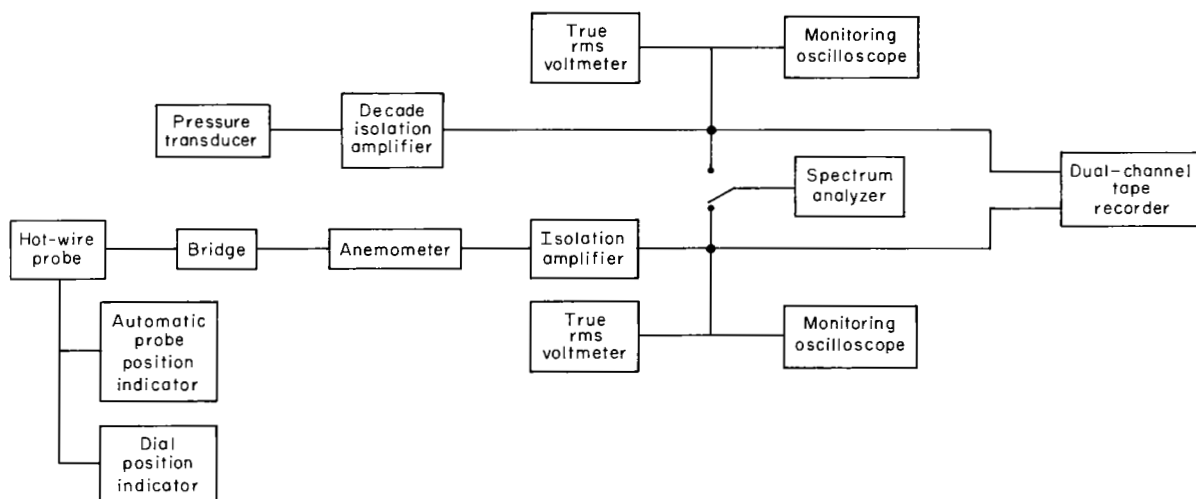


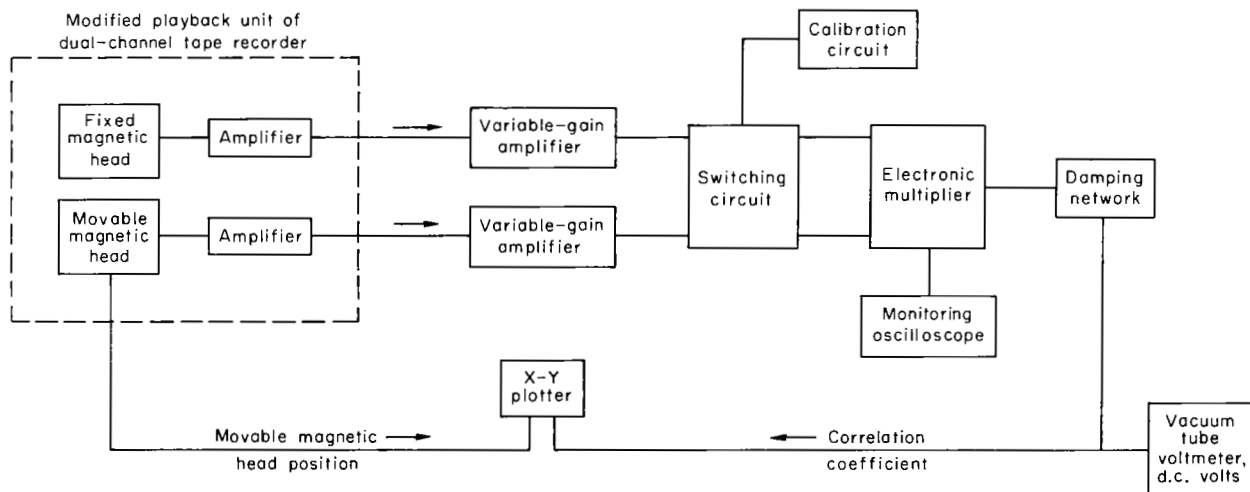
Figure 4. - Sketch of a hot-wire probe and a pressure transducer used in measuring correlation of velocity fluctuations with wall-pressure fluctuations.



(a) In taking data for correlations of wall-pressure fluctuations.



(b) In taking data for correlations of velocity fluctuations with wall-pressure fluctuations.



(c) Correlation computer.

Figure 5. - Block diagrams of instrumentation.

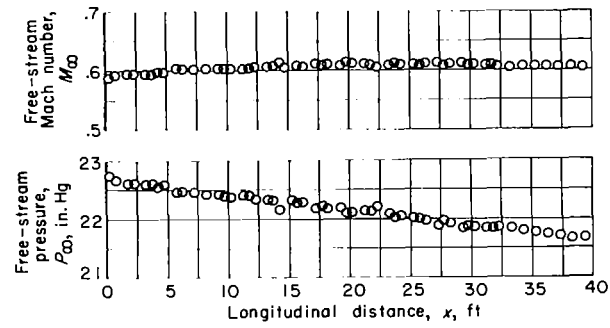
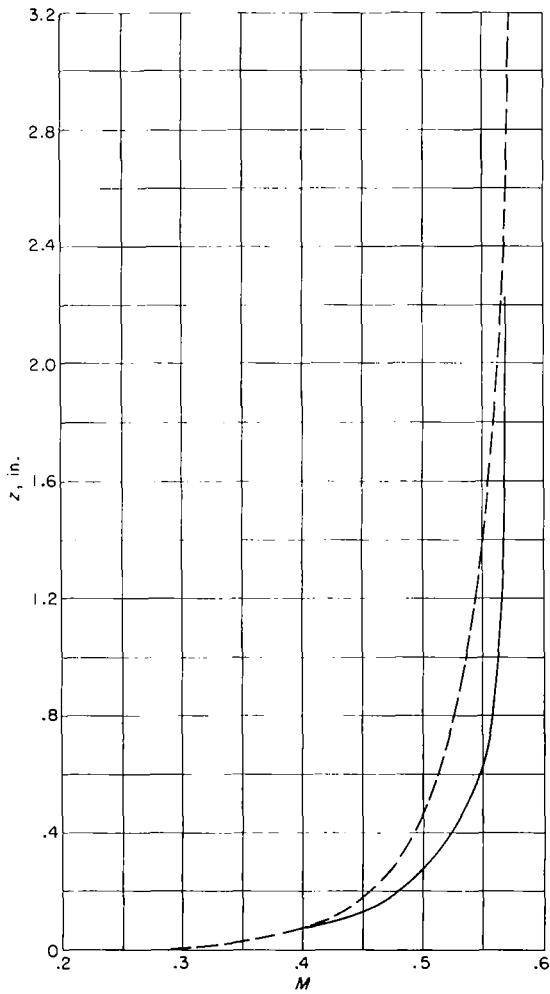
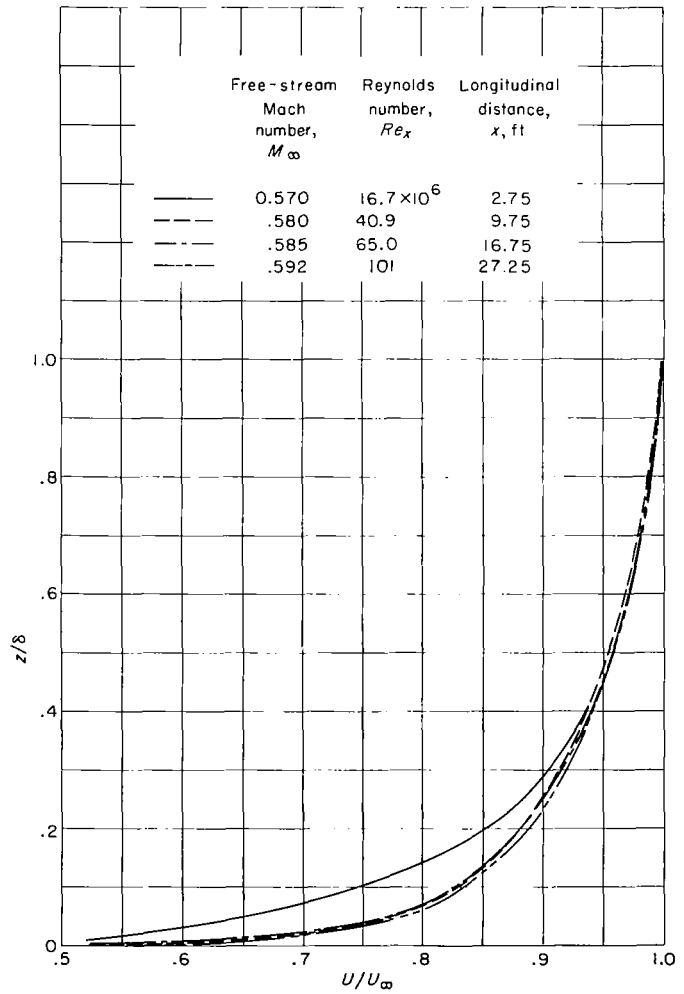


Figure 6. - Longitudinal variation of free-stream pressure and Mach number at centerline of wind tunnel.



(a) Mach number as a function of distance from wall.



(b) Dimensionless velocity as a function of dimensionless distance from wall.

Figure 7. - Typical boundary-layer mean velocity profiles.

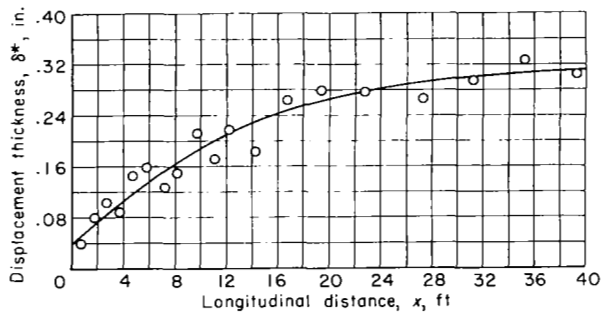


Figure 8. - Variation of displacement thickness with longitudinal distance. Free-stream Mach number, 0.60; Reynolds number per foot,  $3.56 \times 10^6$ .

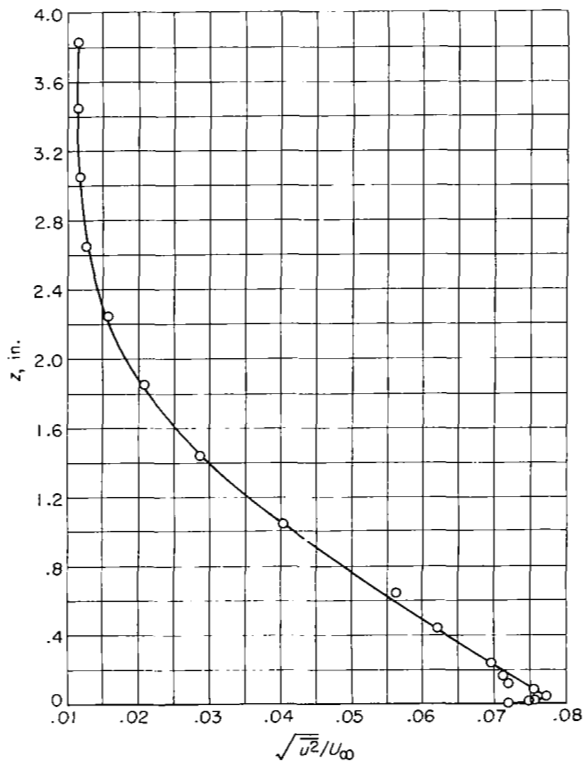


Figure 10. - Boundary-layer profile of ratio of longitudinal intensity to free-stream velocity. Longitudinal distance, 9.25 feet; free-stream Mach number, 0.605; Reynolds number,  $3.98 \times 10^7$ .

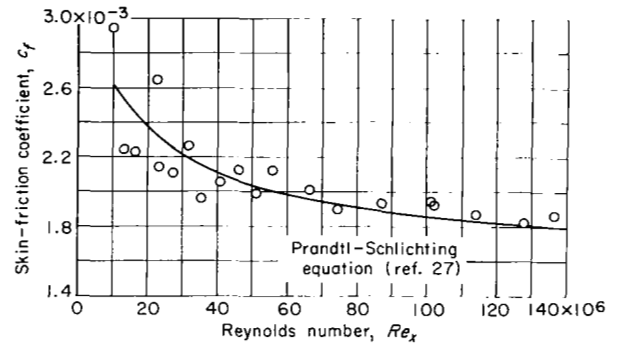


Figure 9. - Local skin-friction coefficient as a function of Reynolds number.

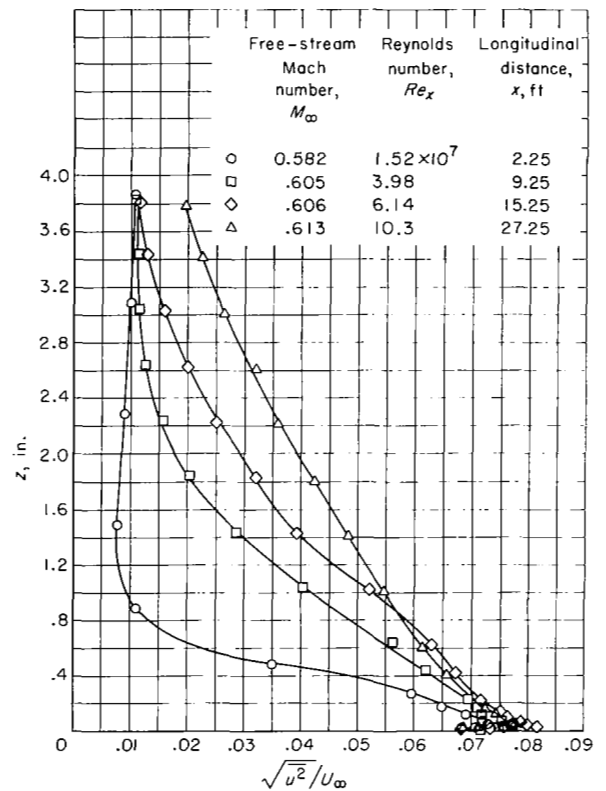


Figure 11. - Comparison of several boundary-layer profiles of longitudinal turbulent intensity divided by free-stream velocity.

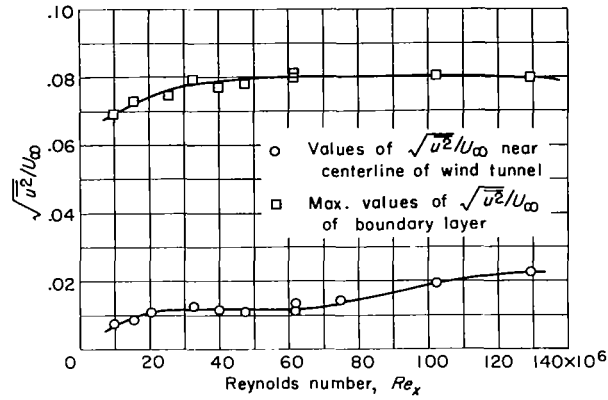
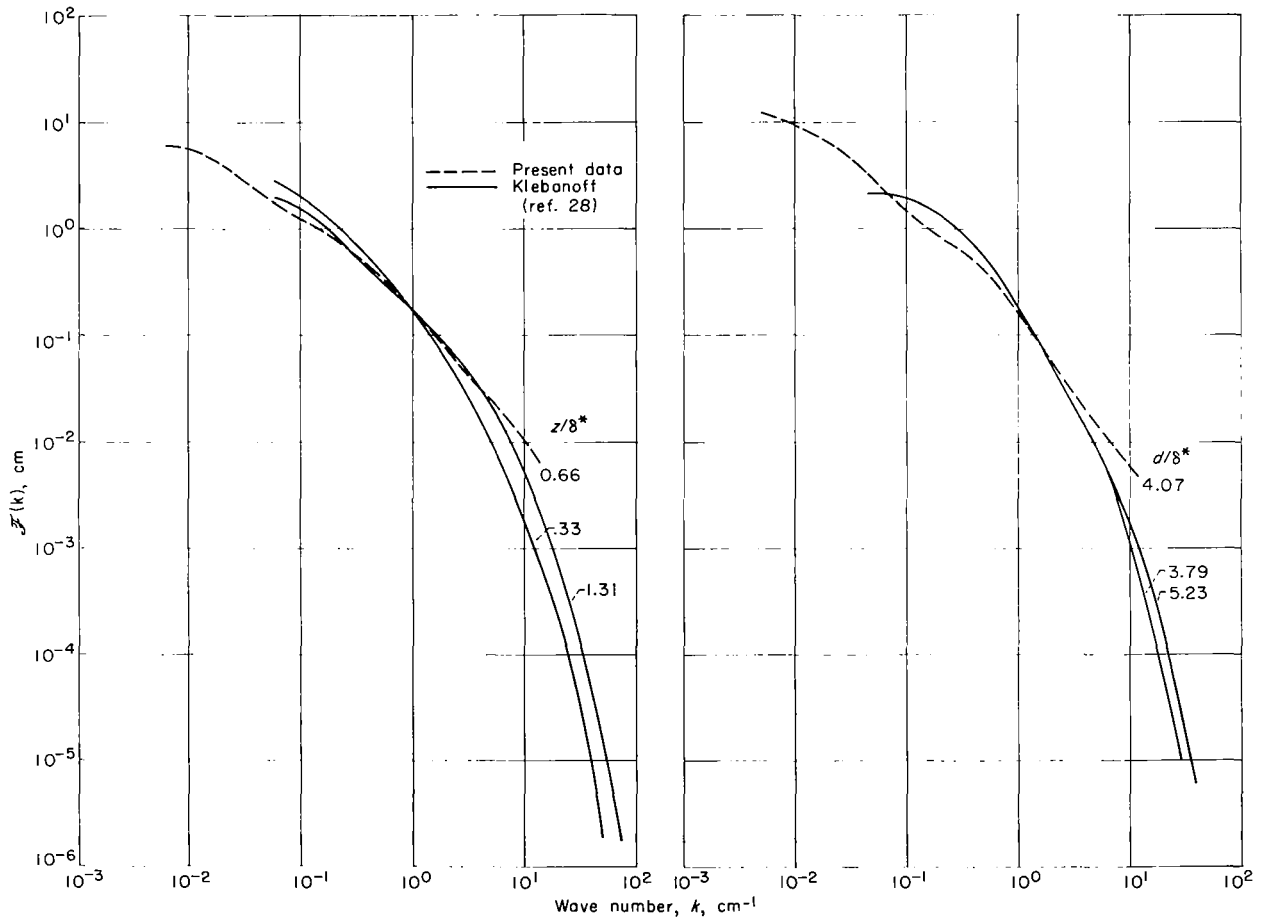


Figure 12. - Variation of turbulent intensity with Reynolds number based on effective turbulent length  $(x - x_0)$ .



(a) Inner region of boundary layer.

(b) Outer region of boundary layer.

Figure 13. - Comparison of u-fluctuation spectra with Klebanoff data (ref. 28).

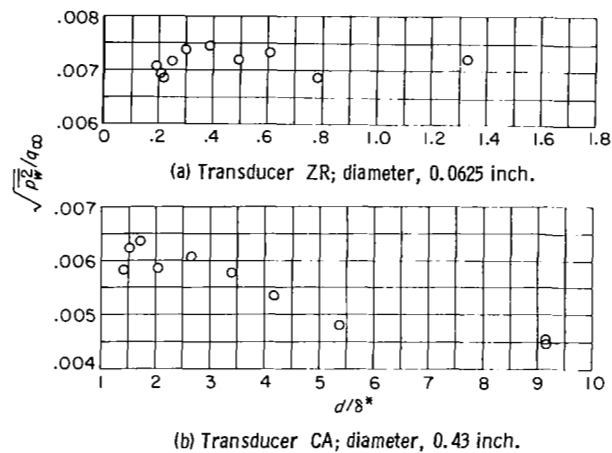


Figure 14. - Dimensionless root-mean-square pressure fluctuations as a function of  $d/\delta^*$ .

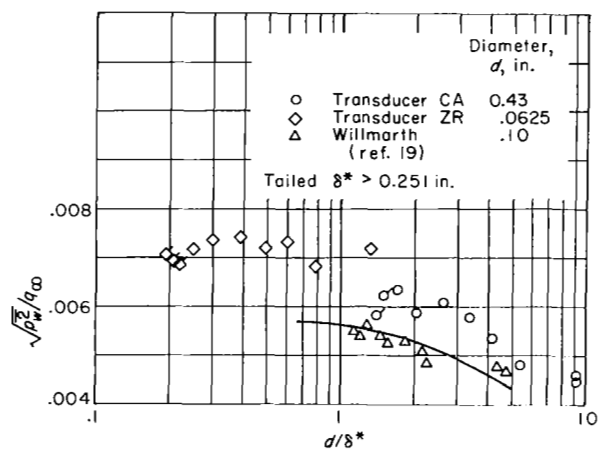
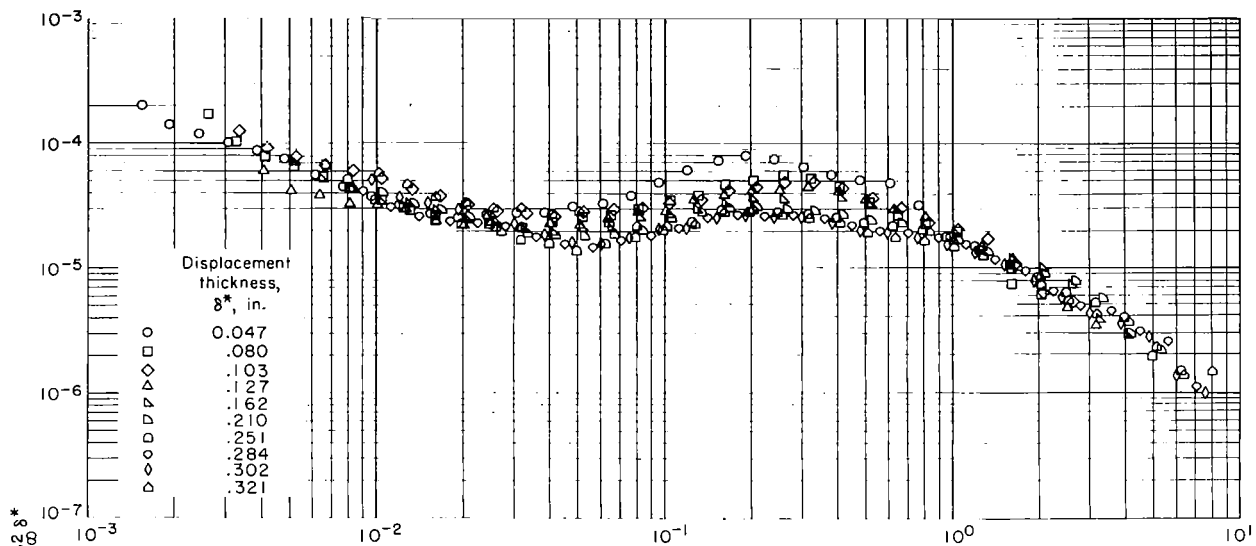
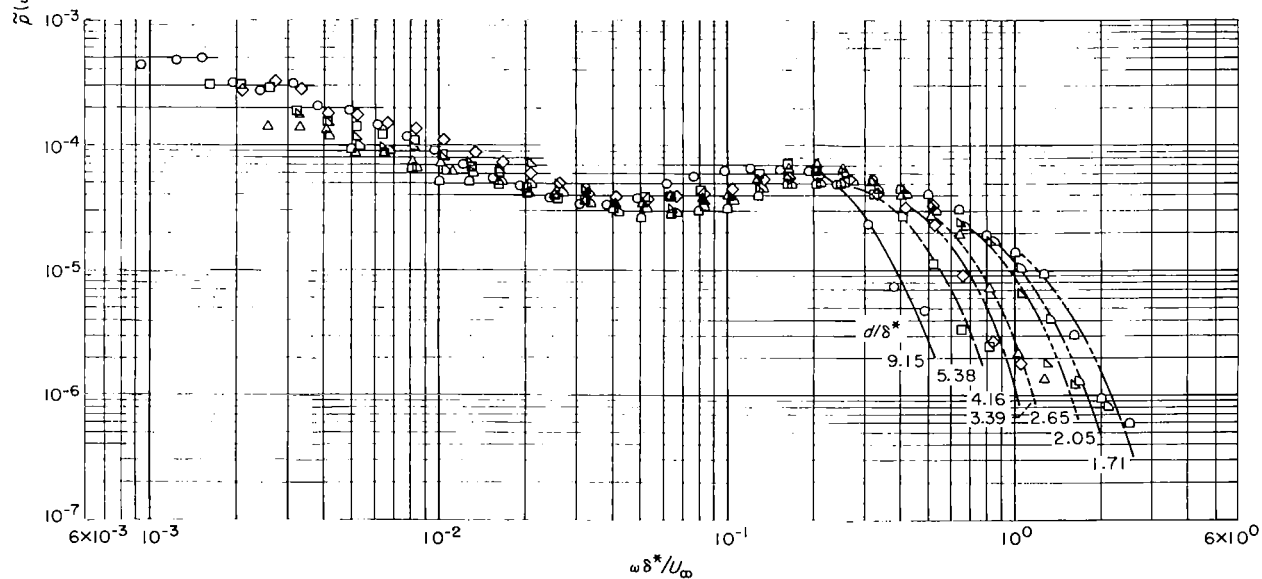


Figure 15. - Comparison of root-mean-square wall-pressure fluctuations with Willmarth data (ref. 19).





(a) Transducer ZR; diameter, 0.0625 inch.



(b) Transducer CA; diameter, 0.43 inch.

Figure 16. - Mean-square spectra of wall-pressure fluctuations. Free-stream Mach number, 0.60; Reynolds number per foot,  $3.45 \times 10^6$ .

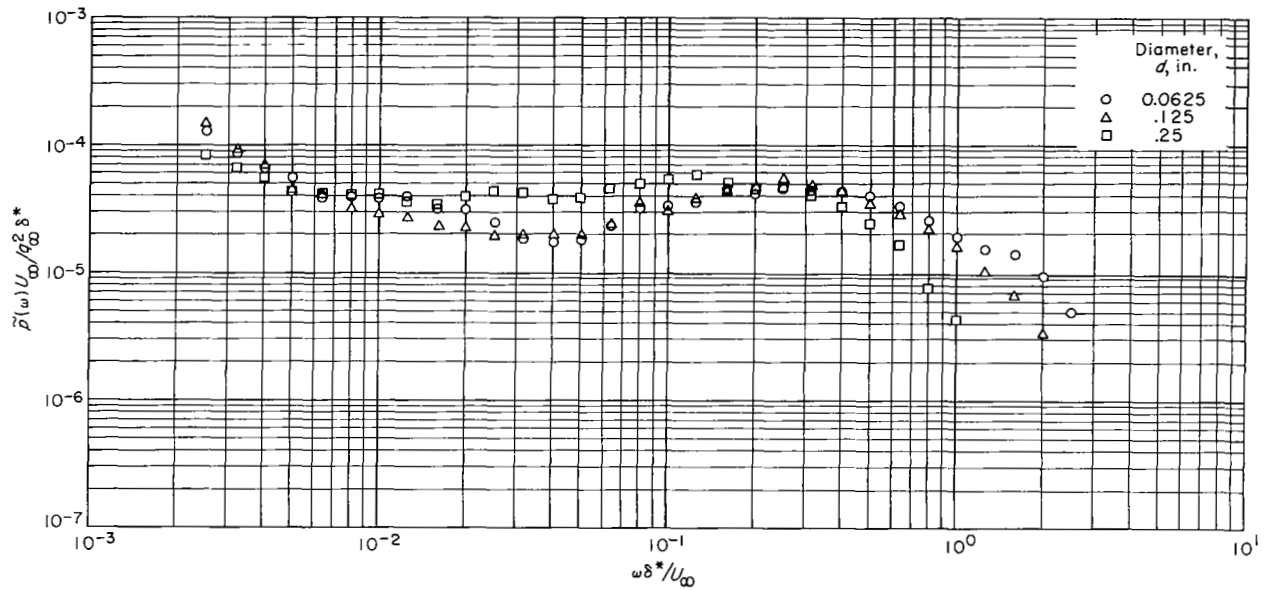


Figure 17. - Mean-square spectra of wall-pressure fluctuations measured at one value of  $\delta^*$  with three piezoelectric transducers of different diameters. Displacement thickness, 0.127 inch; free-stream Mach number, 0.60; Reynolds number per foot,  $3.45 \times 10^6$ .

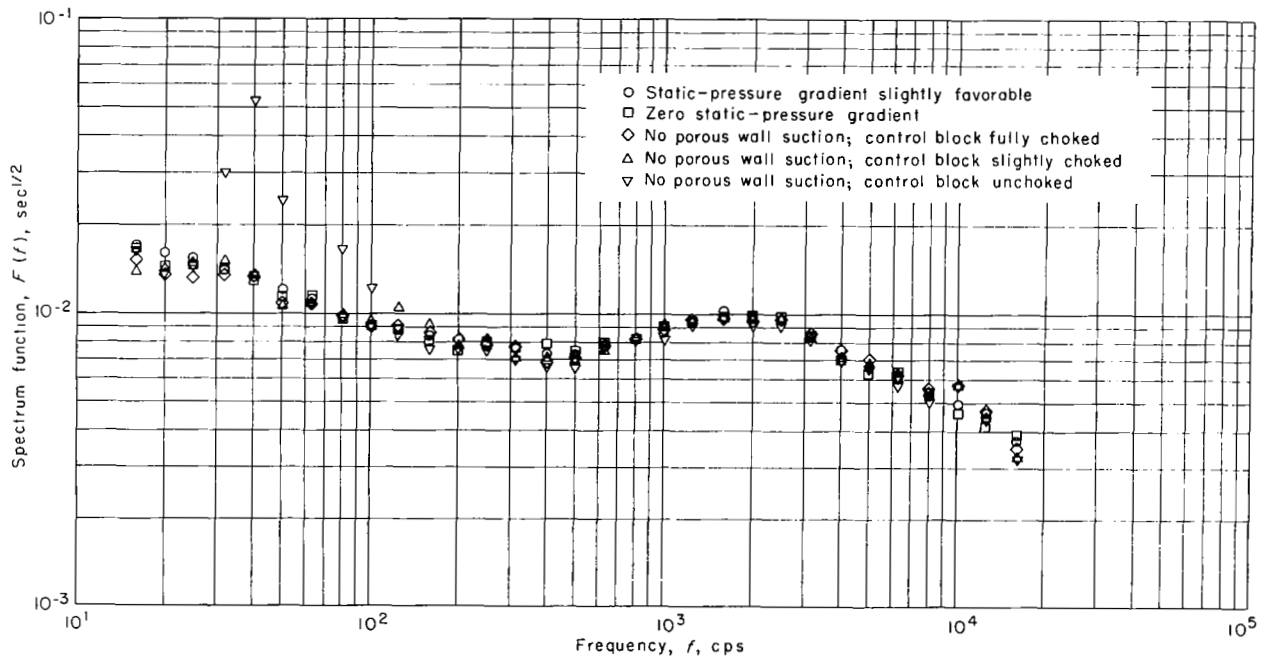


Figure 18. - Comparison of spectra of wall-pressure fluctuations for various flow conditions in test section. Transducer CB; diameter, 0.040 inch; free-stream Mach number, 0.60; Reynolds number per foot,  $3.45 \times 10^6$ .

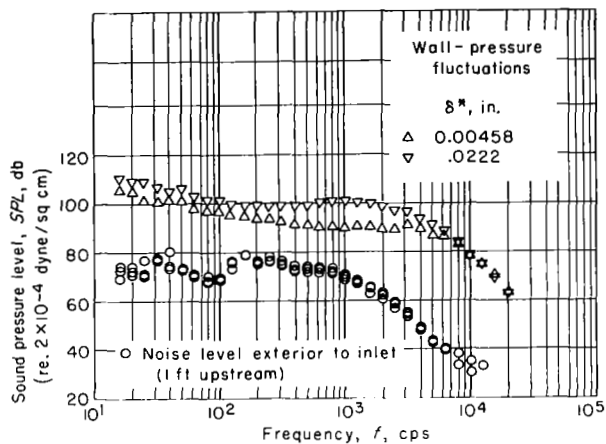


Figure 19. - Comparison of spectra of noise levels measured at inlet of wind tunnel with spectra of wall-pressure fluctuations. Transducer CA; diameter, 0.43 inch. (For external noise measurements microphone faced upward and downstream.)

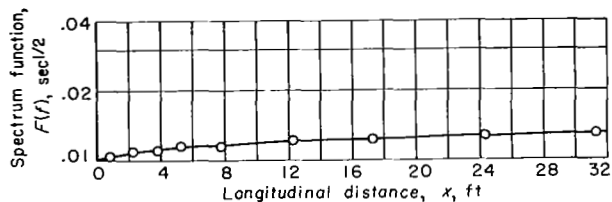


Figure 20. - Spectral value of relative peak at each measuring station plotted against station  $x$ . Transducer ZR; diameter, 0.0625 inch.

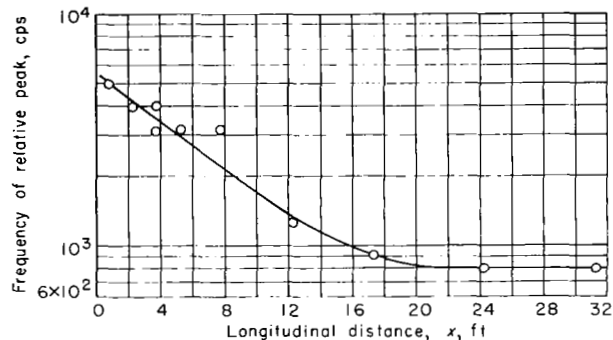


Figure 21. - Frequency at which the relative peak occurs plotted against station  $x$ . Transducer ZR; diameter, 0.0625 inch.

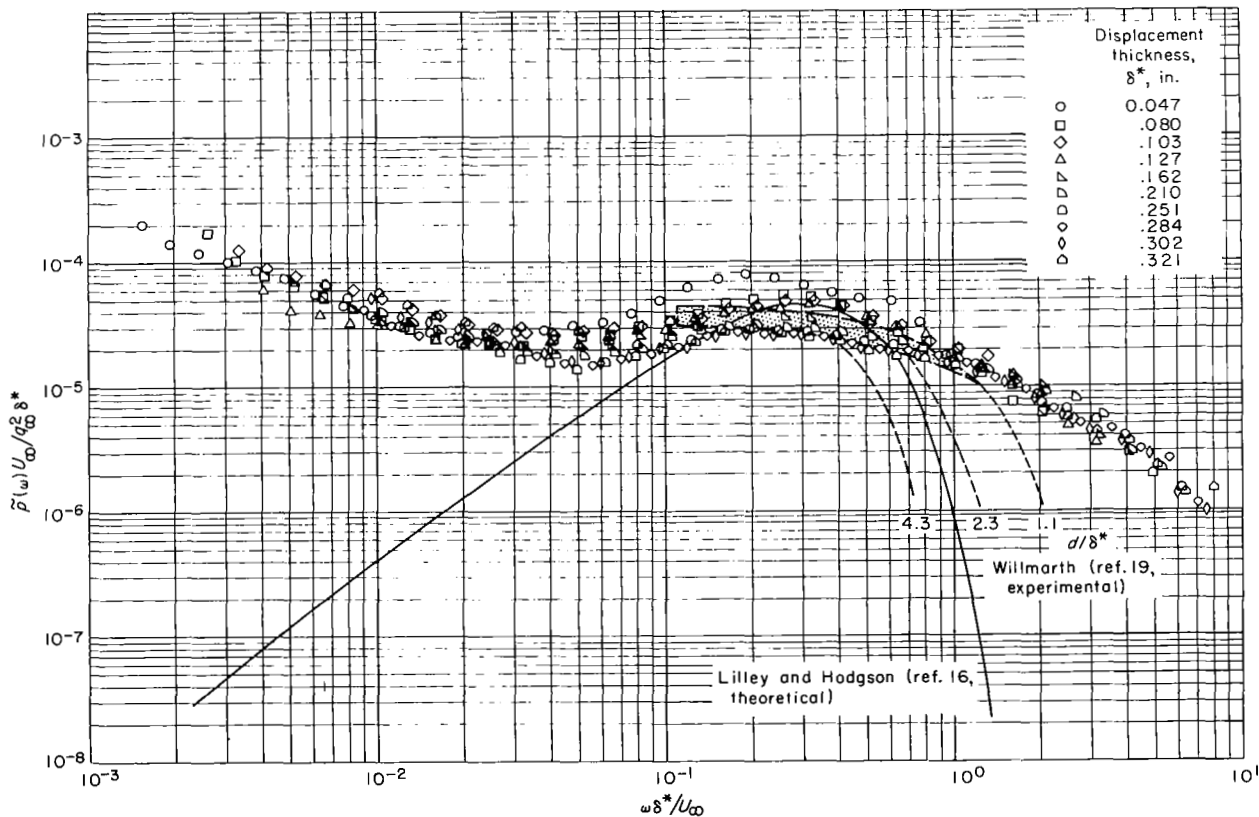


Figure 22. - Comparison of dimensionless mean-square spectra with results of other investigations. Free-stream Mach number, 0.60; Reynolds number per foot,  $3.45 \times 10^6$ .

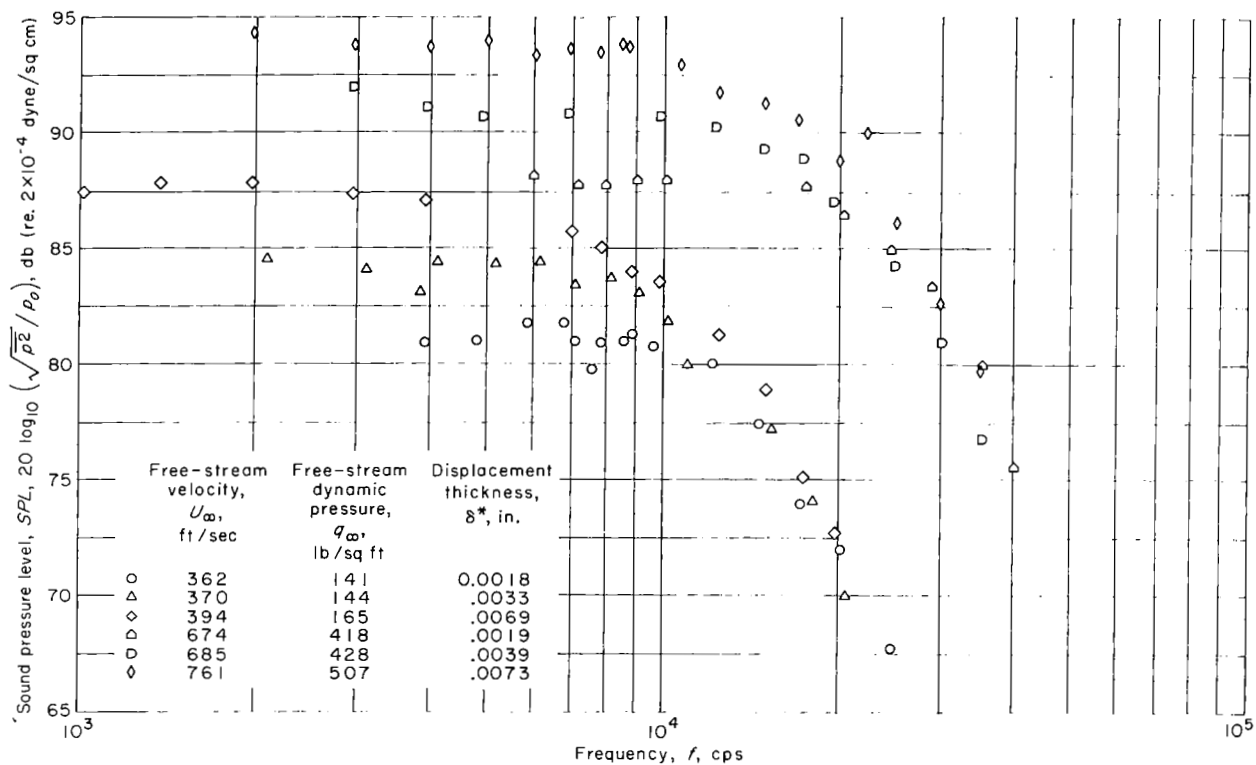


Figure 23. - Replot of Willmarth's spectra (ref. 19) of wall-pressure fluctuations as a function of frequency.

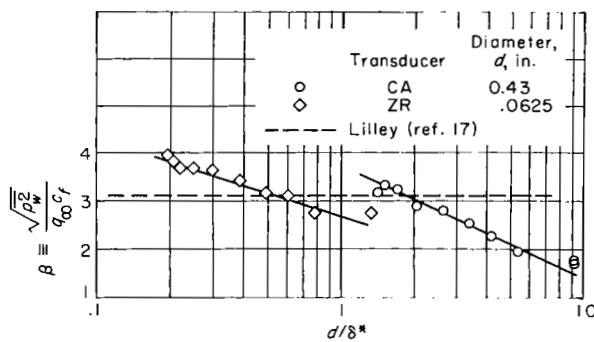
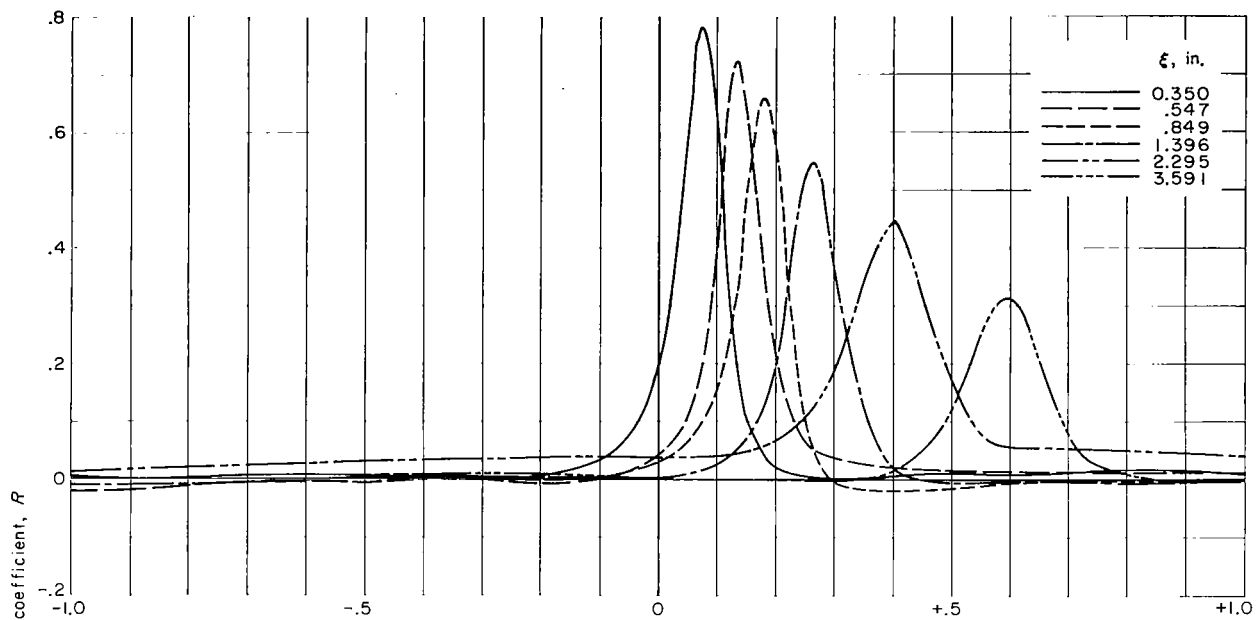
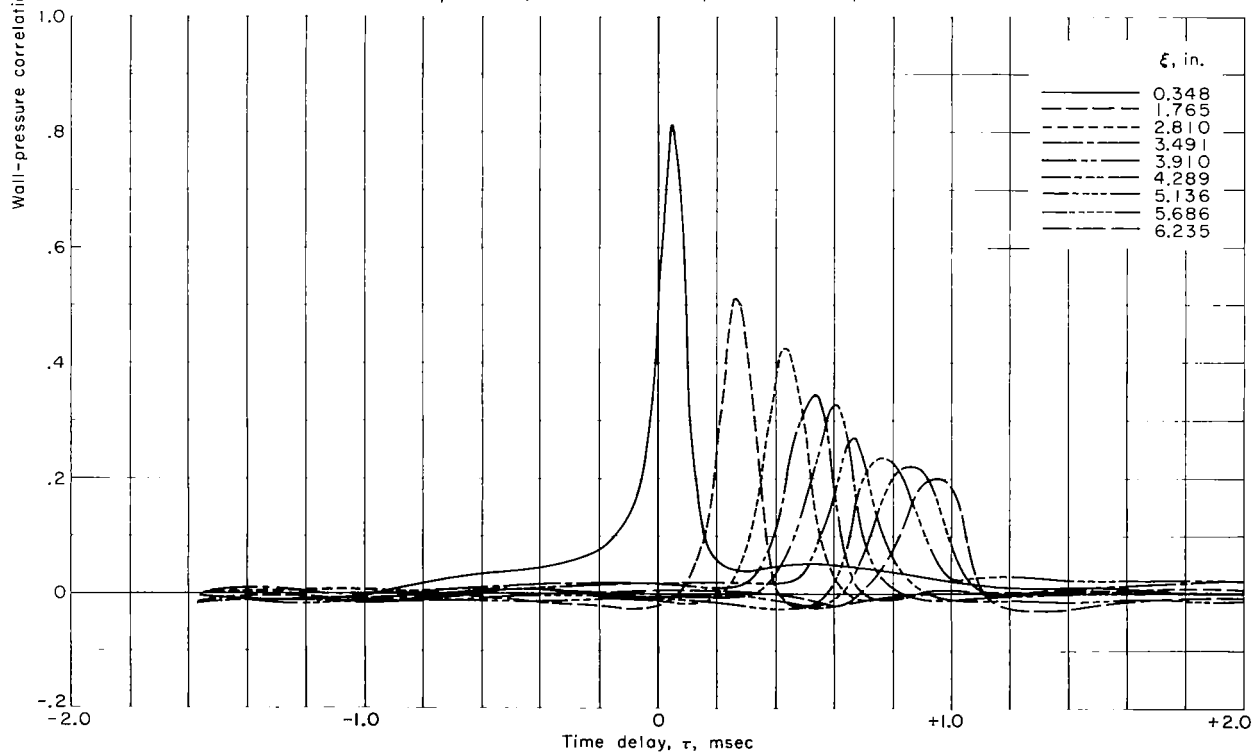


Figure 24. - Comparison of experimental values of root-mean-square magnitude of wall-pressure fluctuations with Lilley theory (ref. 17).



(a)  $\eta = 0$ ; X-Y plotter abscissa scale, 0.2 millisecond per inch.



(b)  $\eta = 0$ ; X-Y plotter abscissa scale, 0.4 millisecond per inch.

Figure 25. - Correlation of wall-pressure fluctuations at two points as a function of time delay.

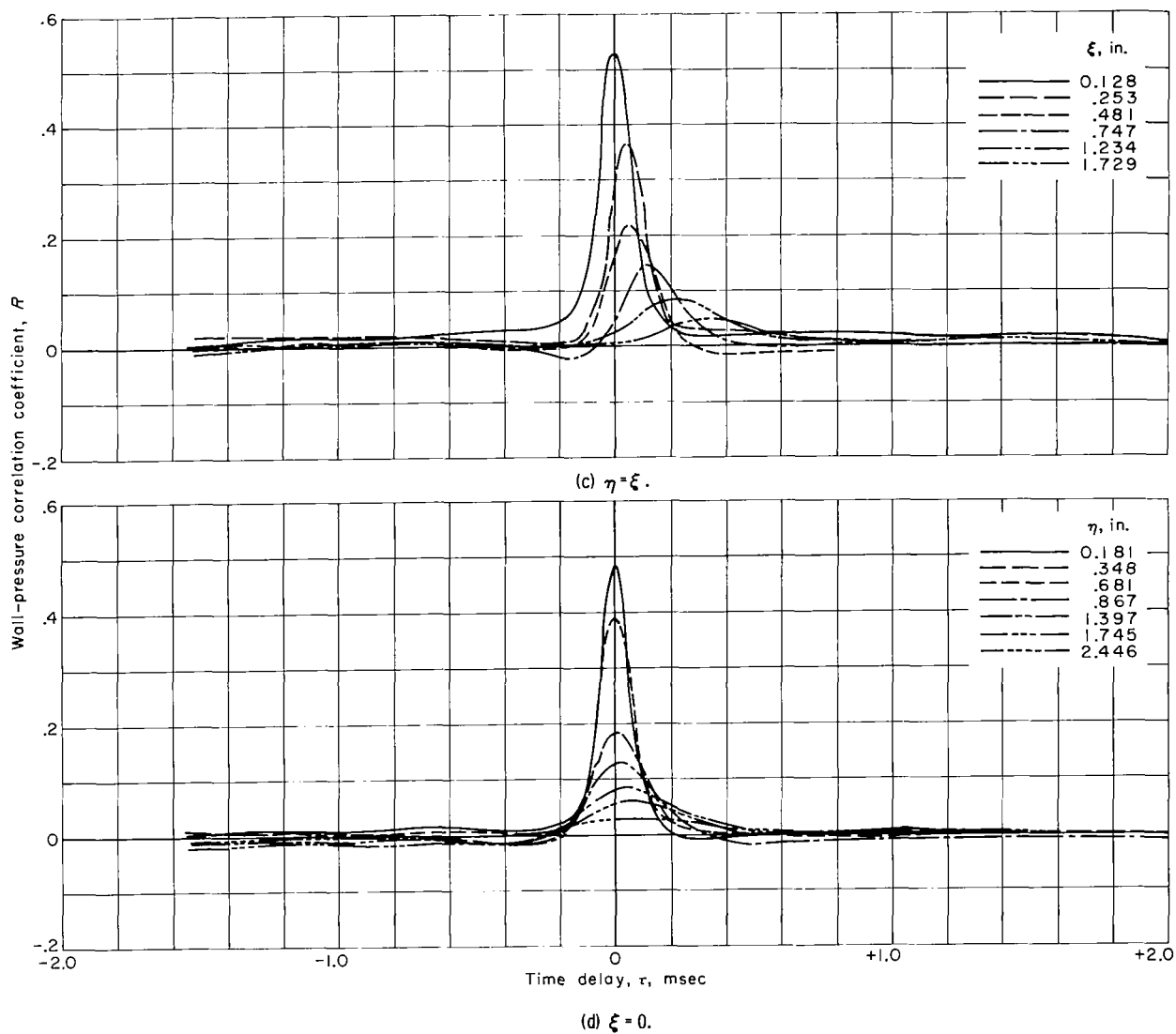


Figure 25. - Concluded. Correlation of wall-pressure fluctuations at two points as a function of time delay.

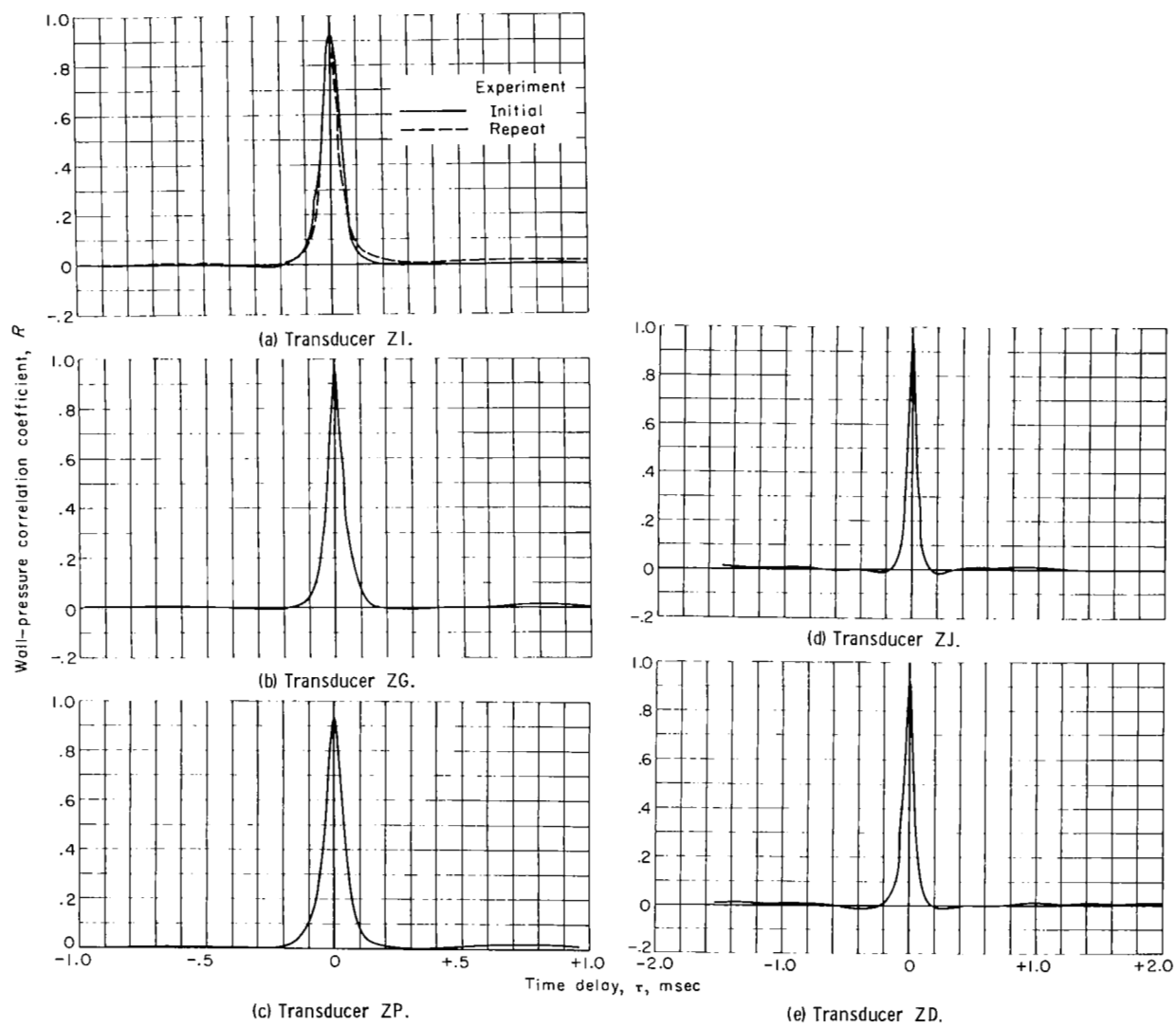


Figure 26. - Typical autocorrelations of wall-pressure fluctuations.

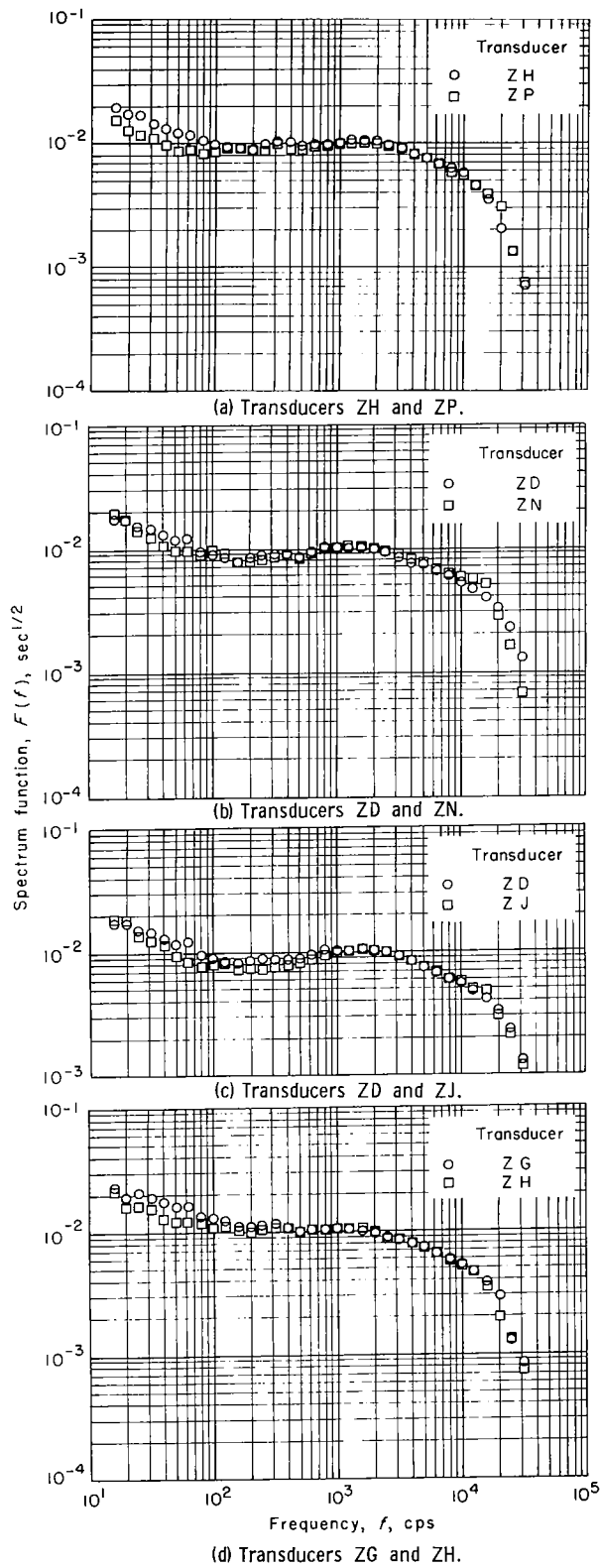


Figure 27. - Comparison of spectra measured by transducer pairs used in obtaining correlations of wall-pressure fluctuations.

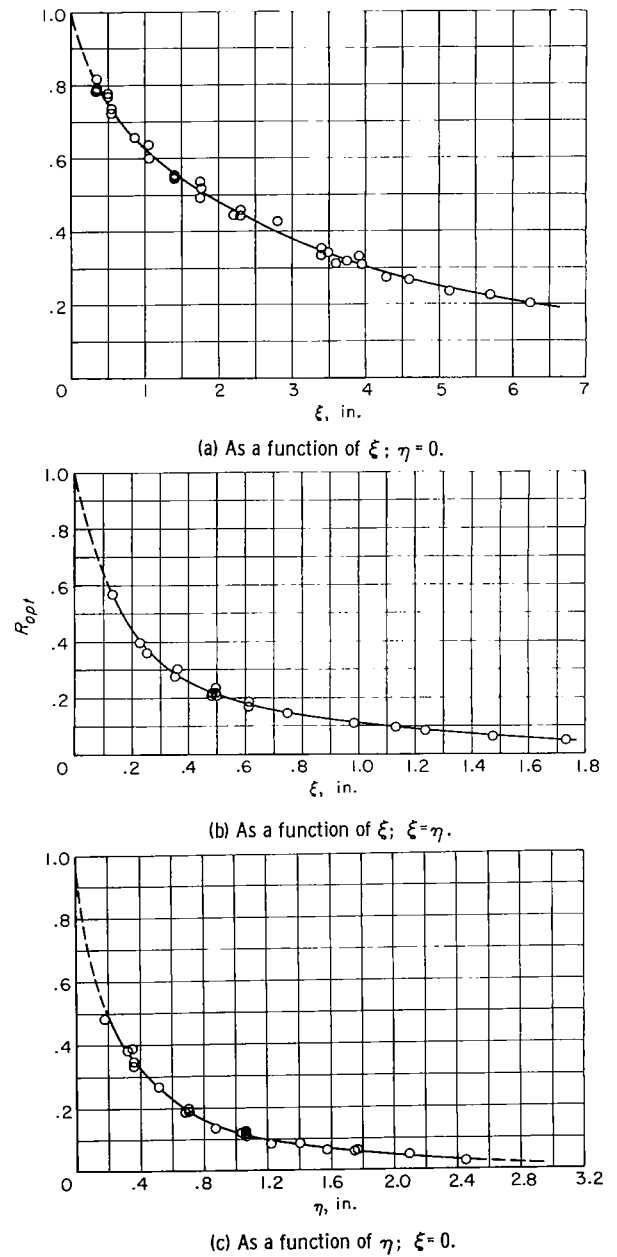


Figure 28. - Optimum correlation of wall-pressure fluctuations.



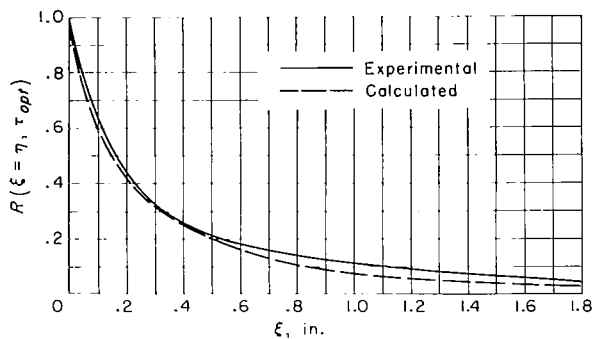


Figure 29. - Comparison for  $R_{opt}(\xi = \eta, \tau_{opt})$  of experimental curve with that calculated from optimum correlations obtained for  $\xi = 0$  and  $\eta = 0$ .

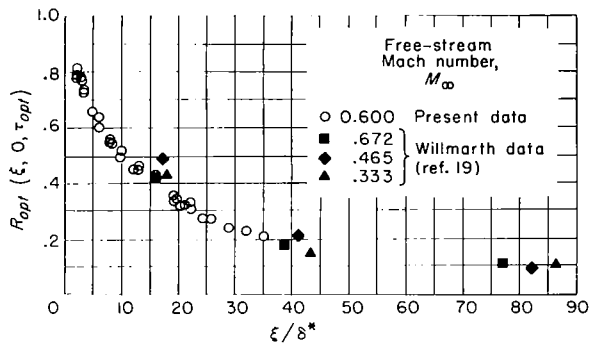


Figure 30. - Comparison of correlation coefficient  $R_{opt}(\xi, 0, \tau_{opt})$  with Willmarth data (ref. 19).  $\eta = 0$ .

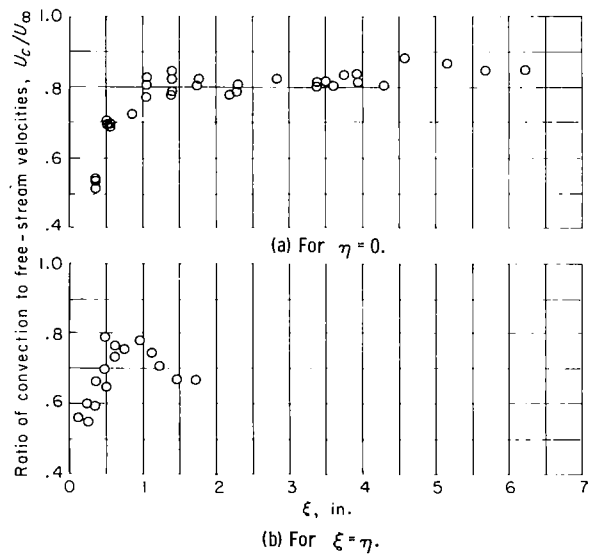


Figure 31. - Ratio of convection to free-stream velocities as a function of  $\xi$ -component of separation distance.

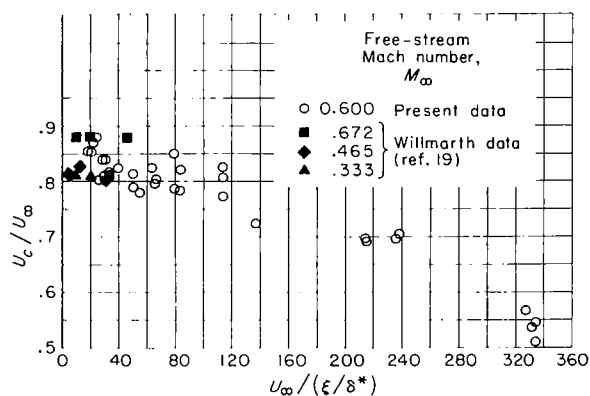
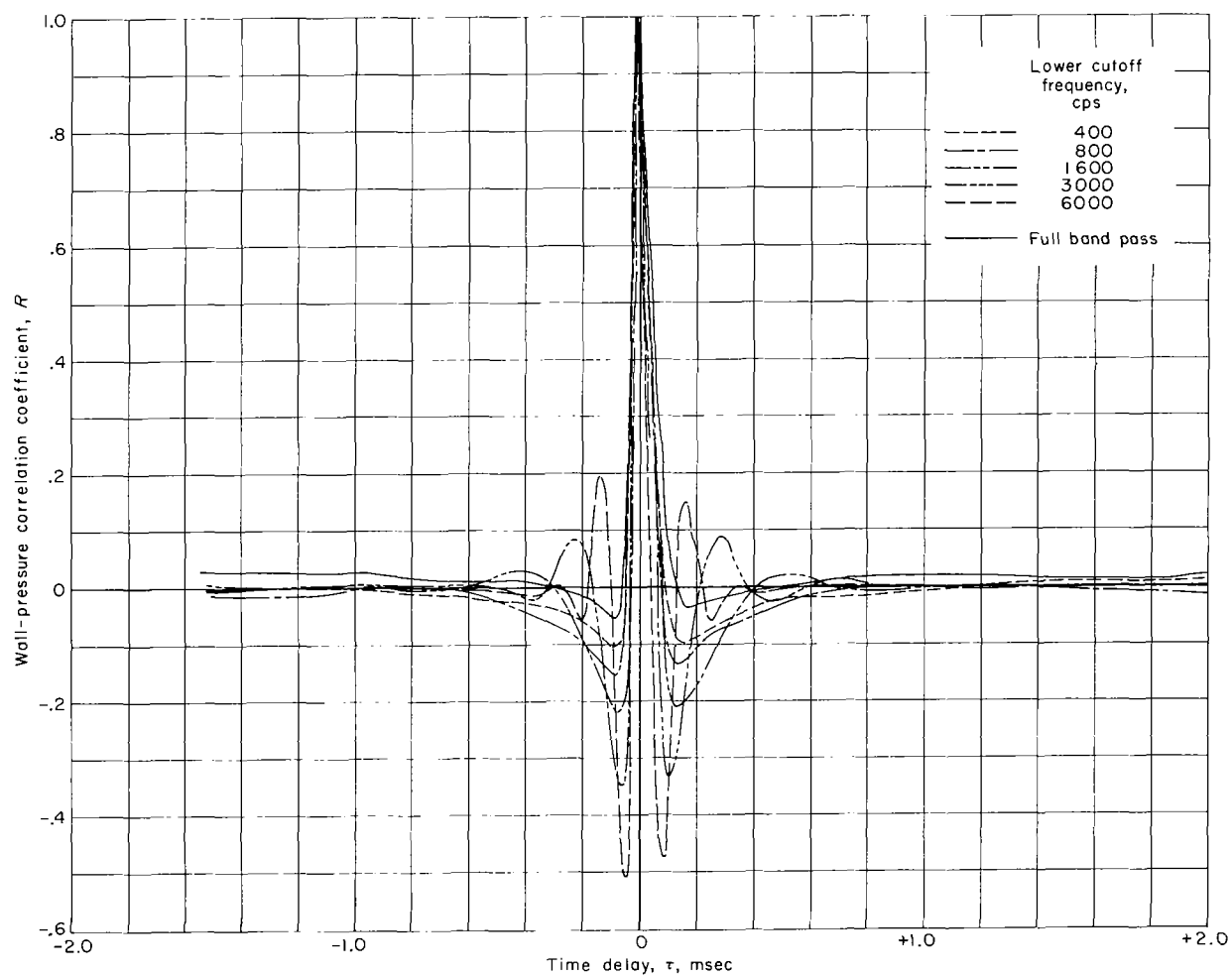


Figure 32. - Comparison of ratio of convection to free-stream velocities with Willmarth data (ref. 19).  $\eta = 0$ .



(a) Autocorrelation with transducer ZF.

Figure 33. - Effect of high-pass-band filtering on correlation of wall-pressure fluctuations as a function of time delay.

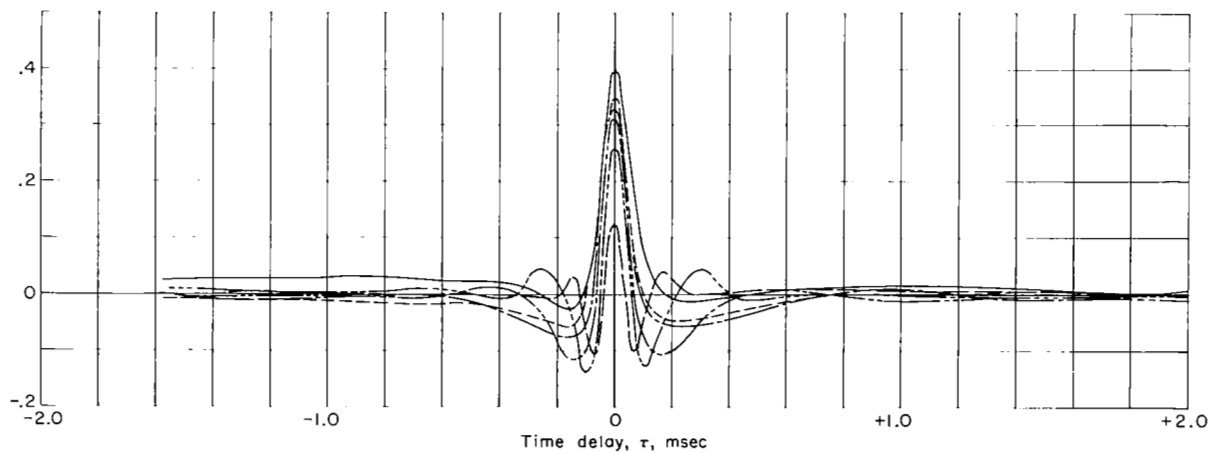
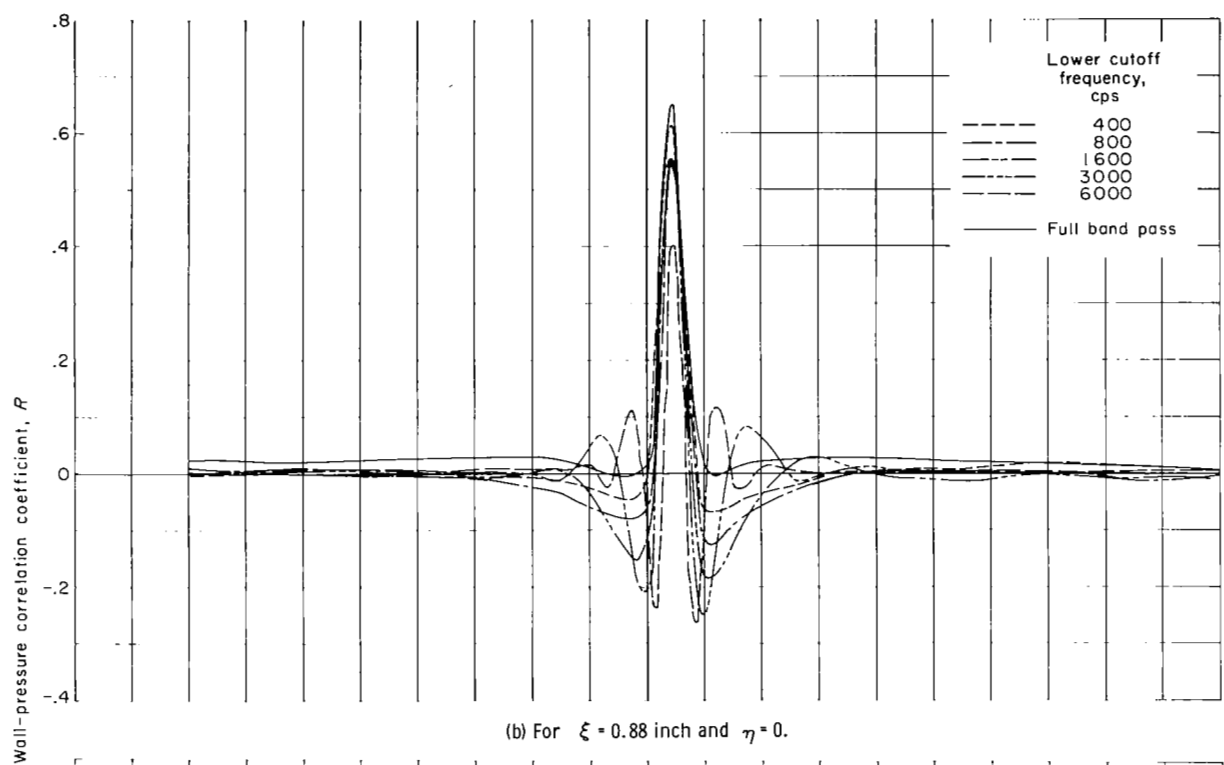
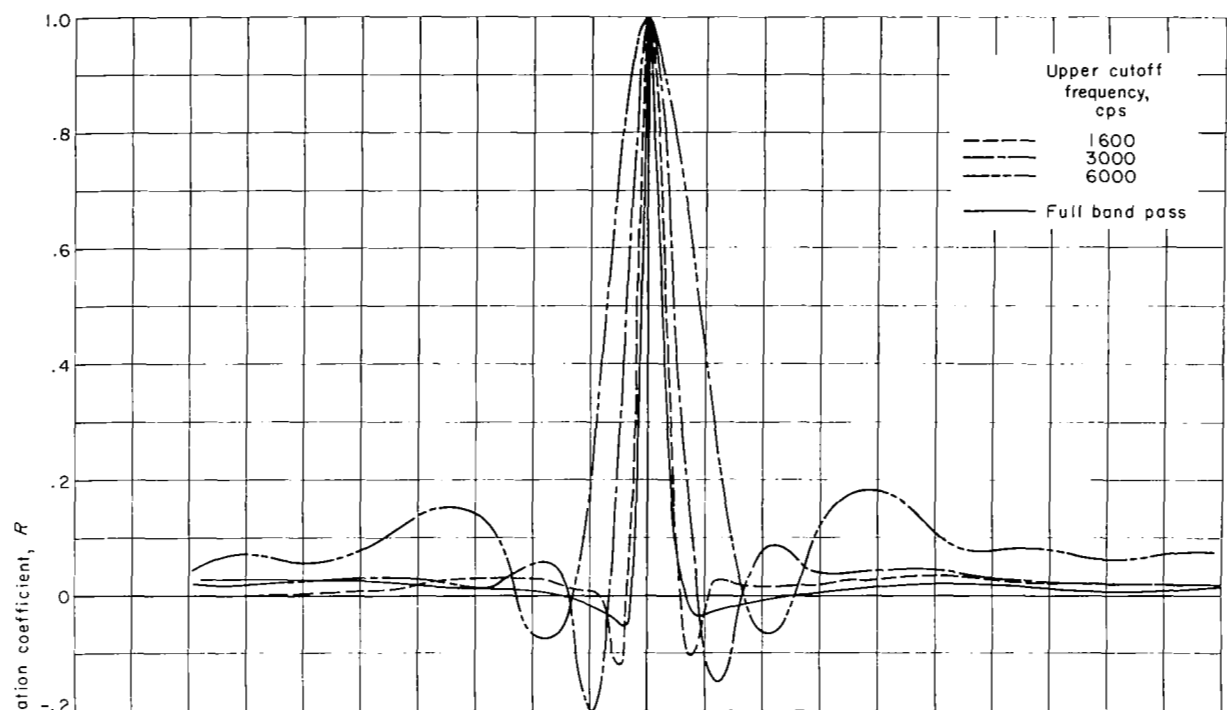
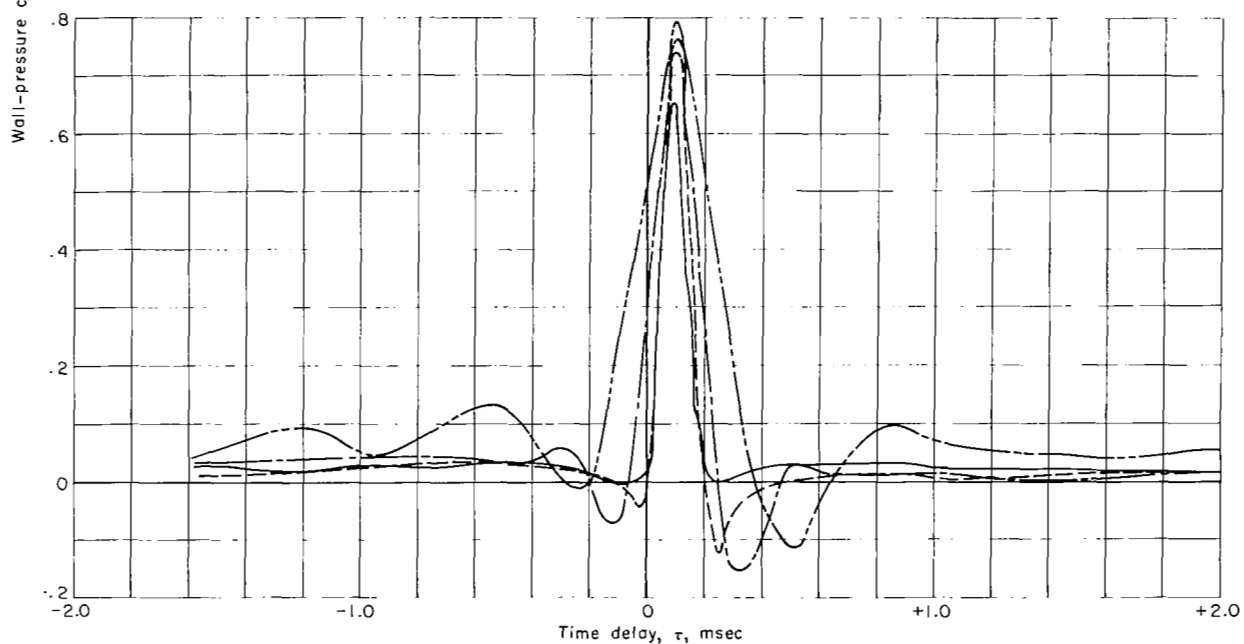


Figure 33. - Concluded. Effect of high-pass-band filtering on correlation of wall-pressure fluctuations as a function of time delay.

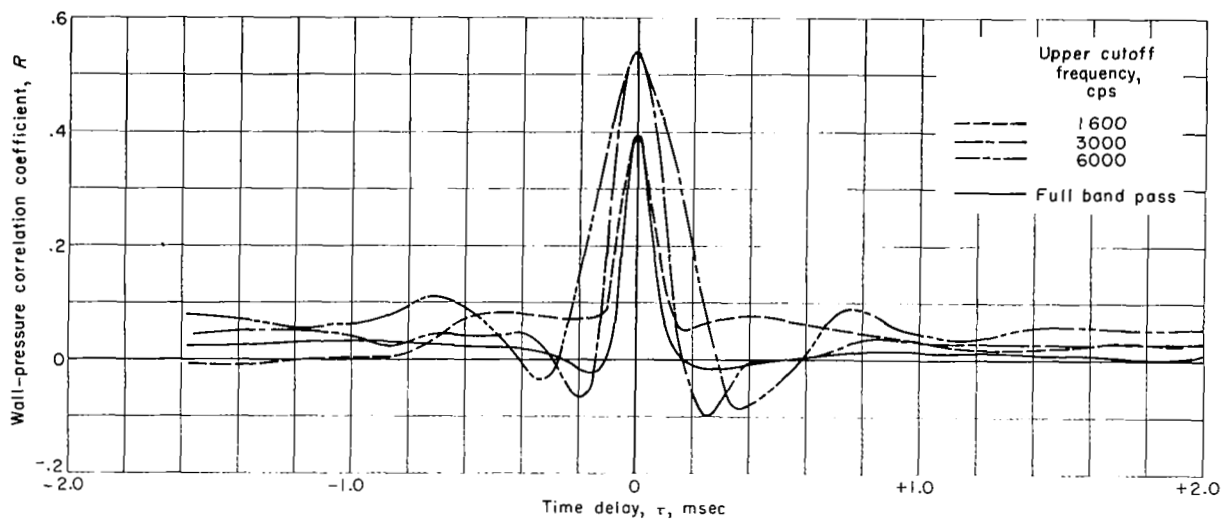


(a) Autocorrelation with transducer ZF.



(b) For  $\xi = 0.88$  inch and  $\eta = 0$ .

Figure 34. - Effect of low-pass-band filtering on correlation of wall-pressure fluctuations as a function of time delay.



(c) For  $\xi = 0$  and  $\eta = 0.325$  inch.

Figure 34. - Concluded. Effect of low-pass-band filtering on correlation of wall-pressure fluctuations as a function of time delay.

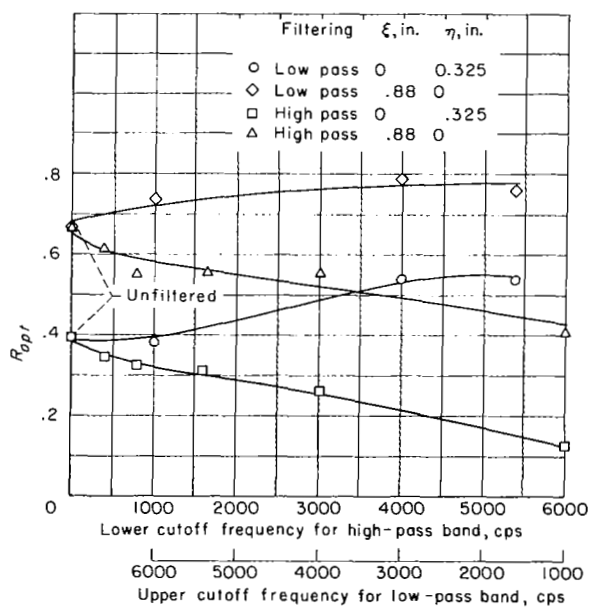


Figure 35. - Effect of high- and low-pass-band filtering on optimum correlation of wall-pressure fluctuations.

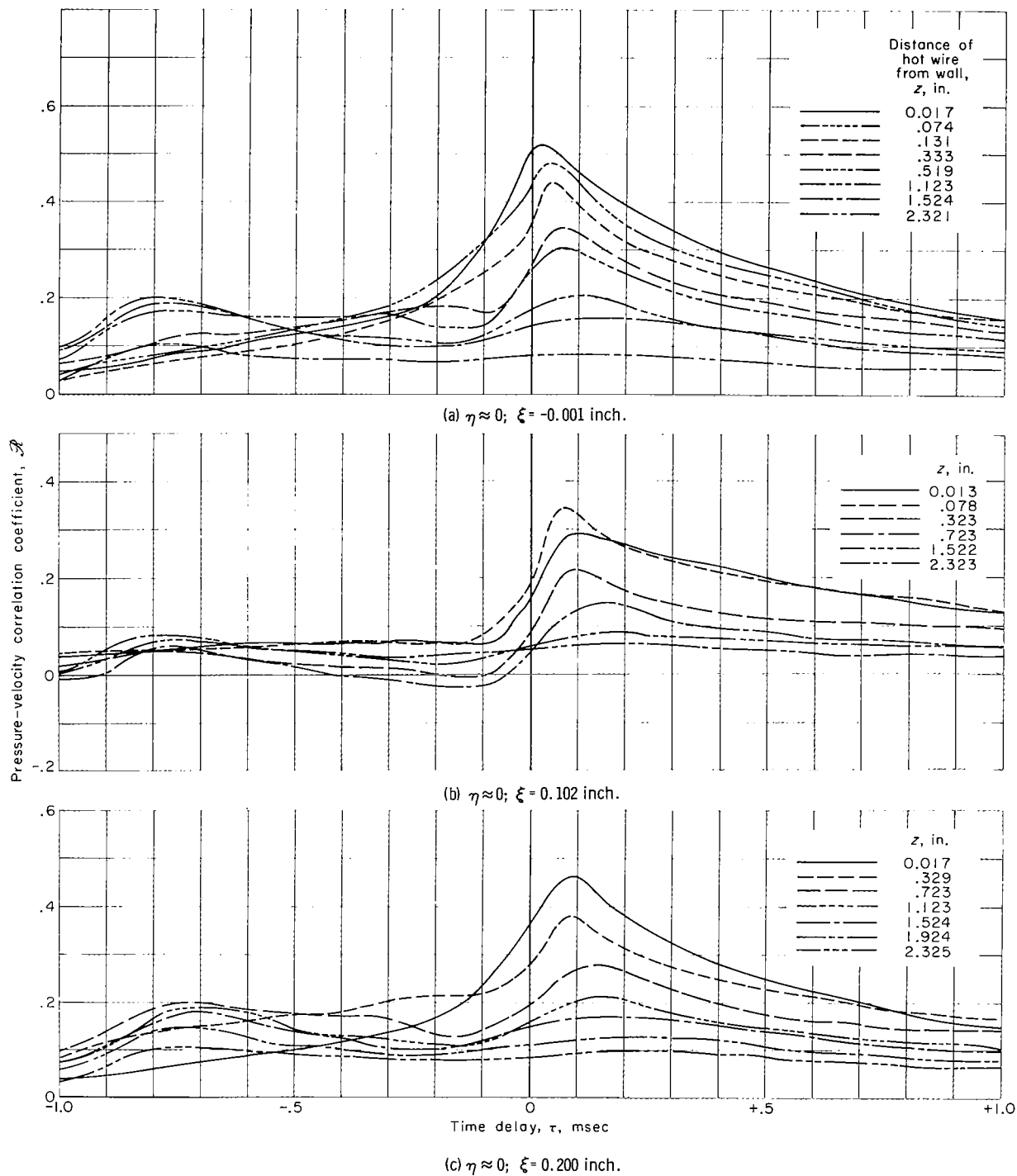


Figure 36. - Correlation of velocity fluctuations with wall-pressure fluctuations, measured with transducer ZS.

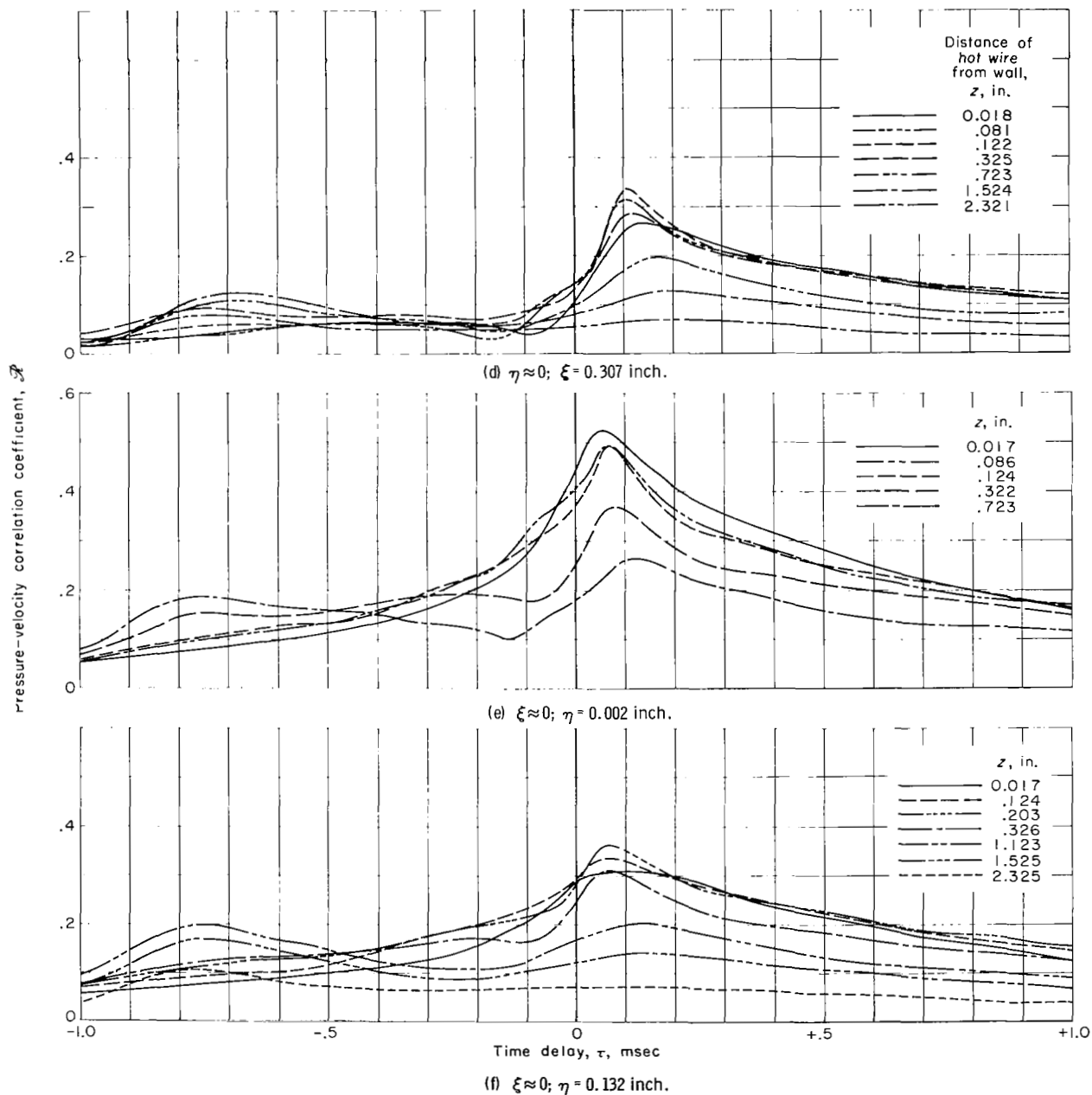


Figure 36. - Continued. Correlation of velocity fluctuations with wall-pressure fluctuations, measured with transducer ZS.

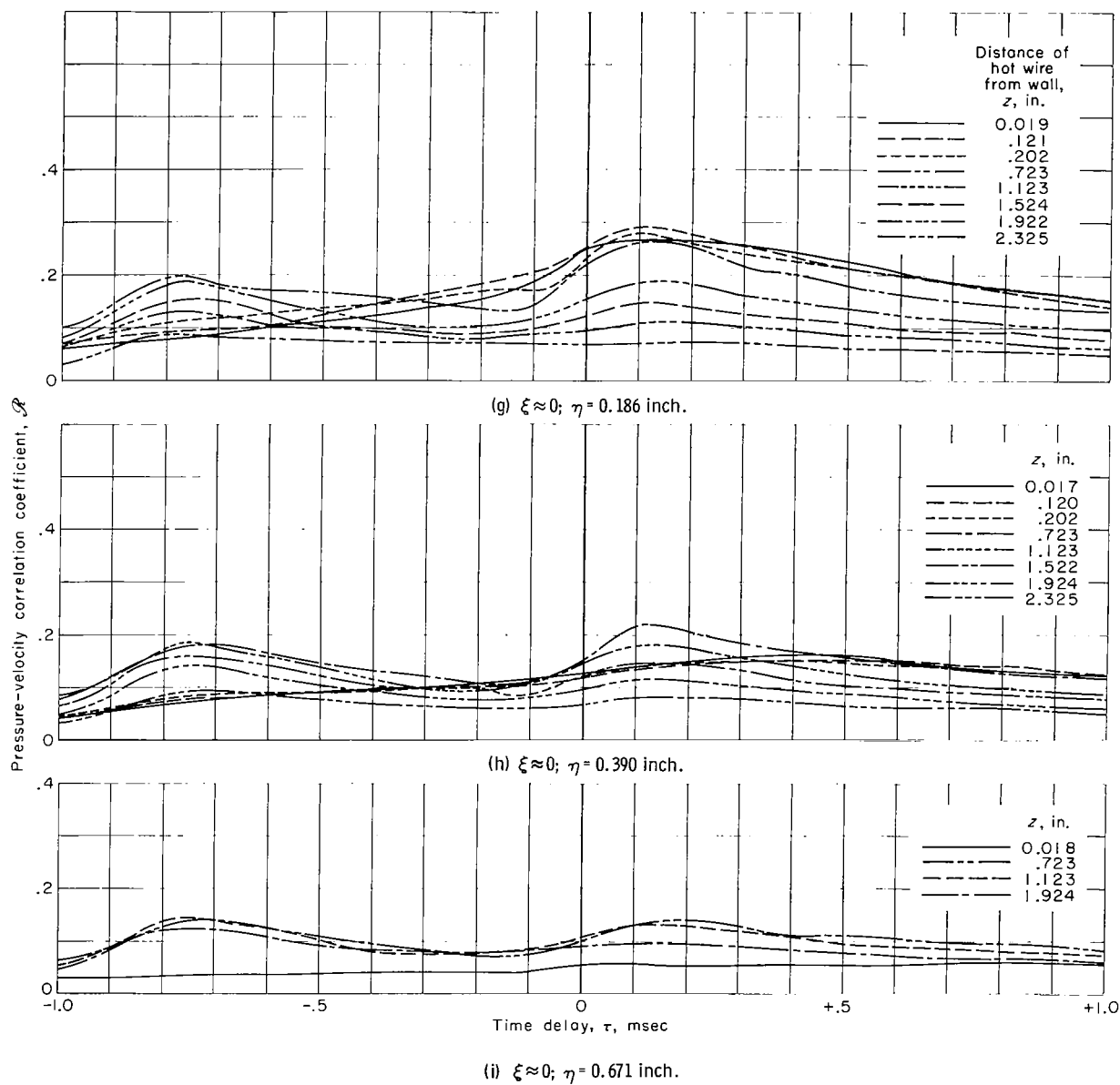


Figure 36. - Concluded. Correlation of velocity fluctuations with wall-pressure fluctuations, measured with transducer ZS.



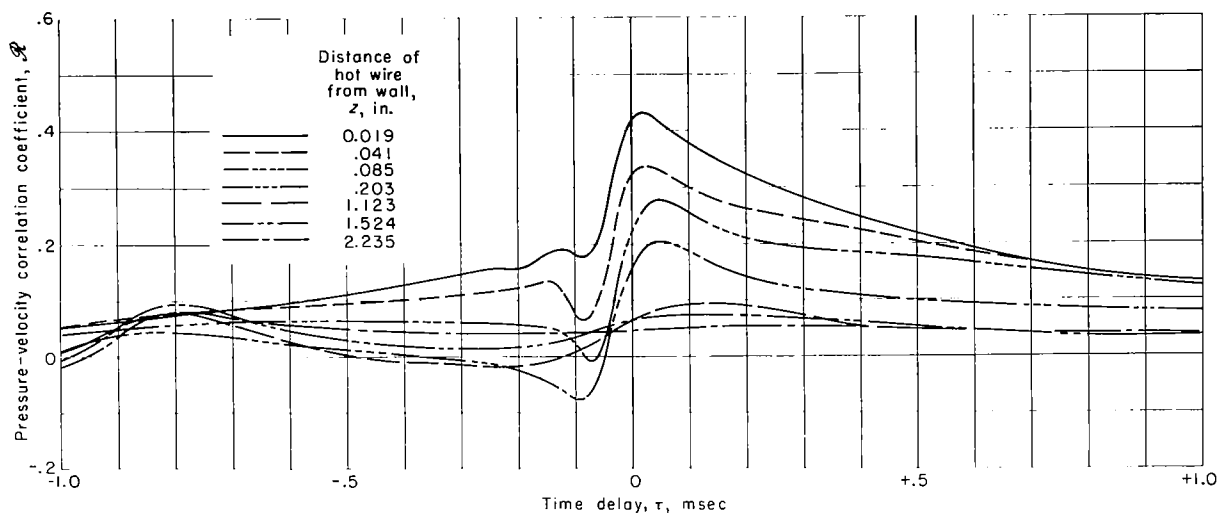


Figure 37. - Correlation of velocity fluctuations with wall-pressure fluctuations, measured with transducer CB.  $\xi \approx 0$ ;  $\eta = 0.003$  inch.

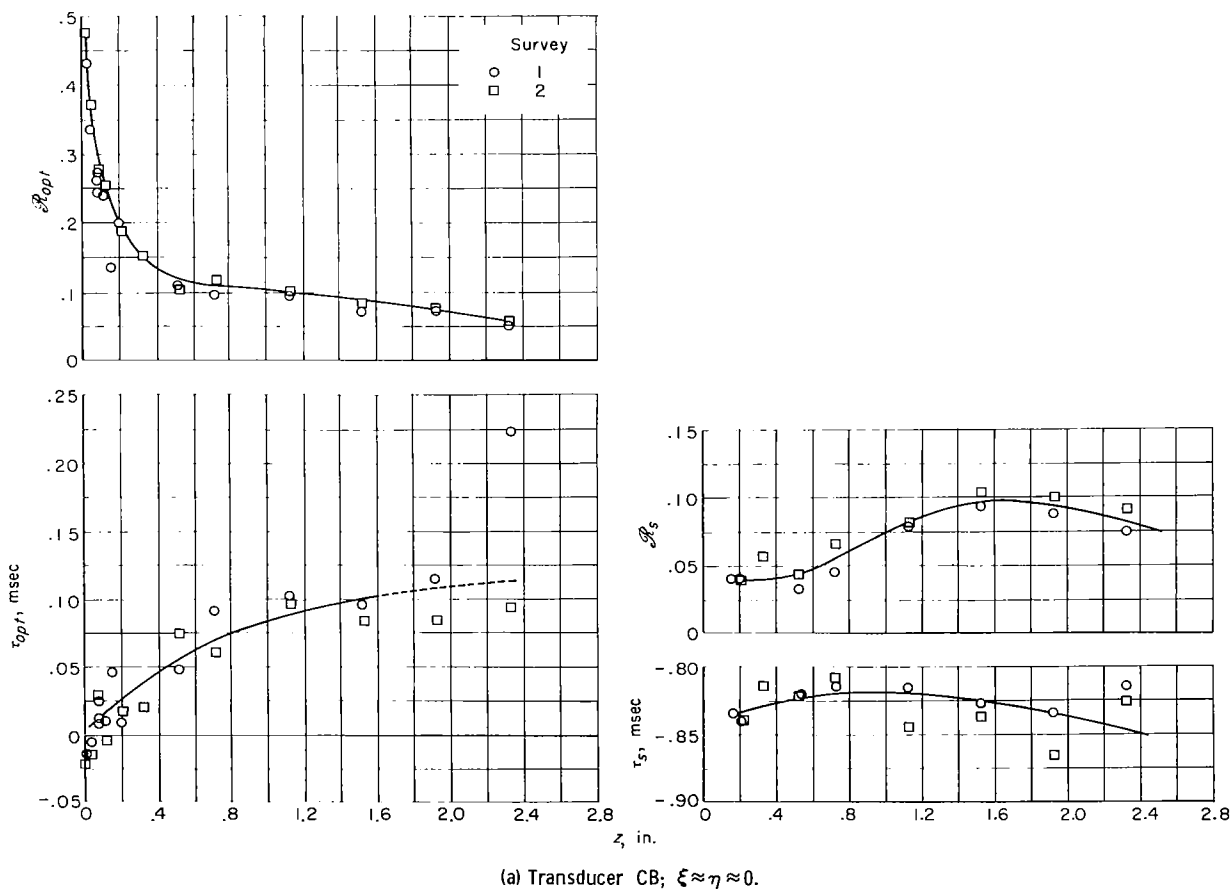
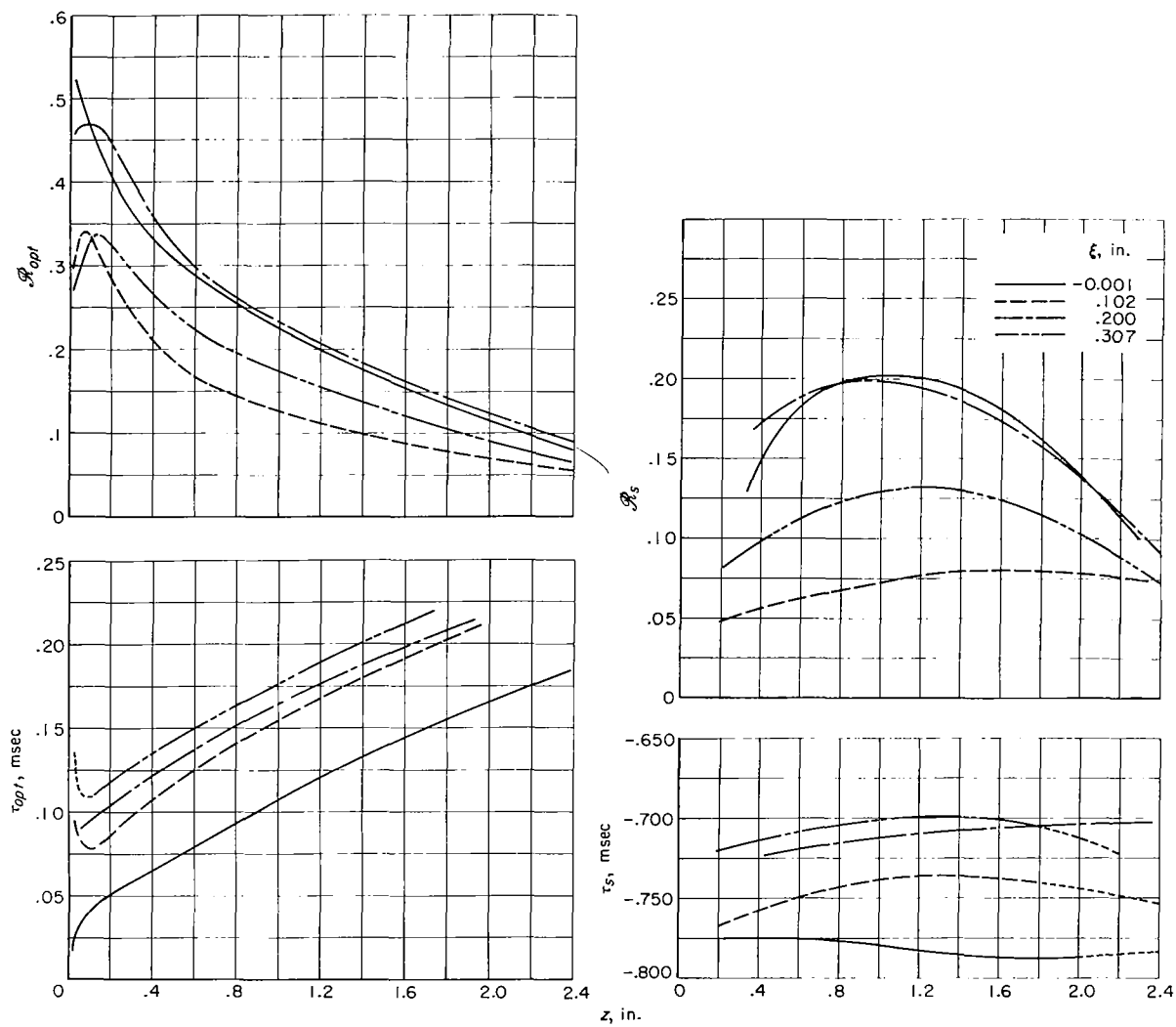
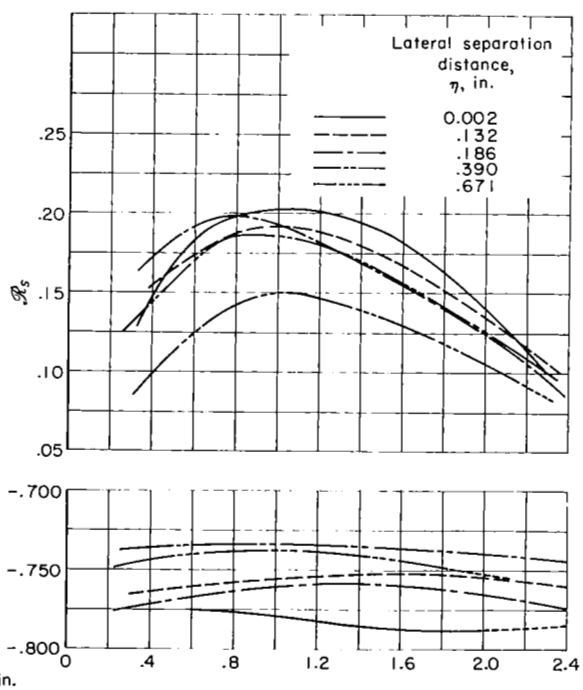
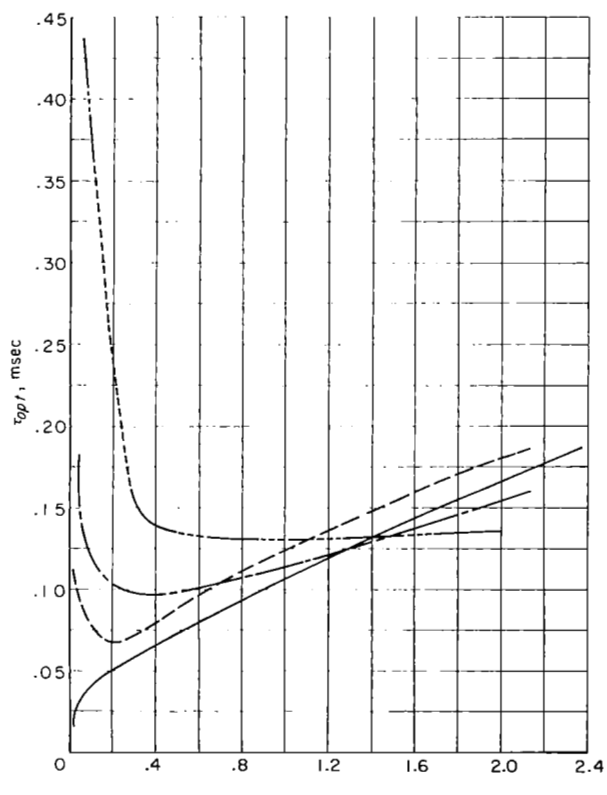
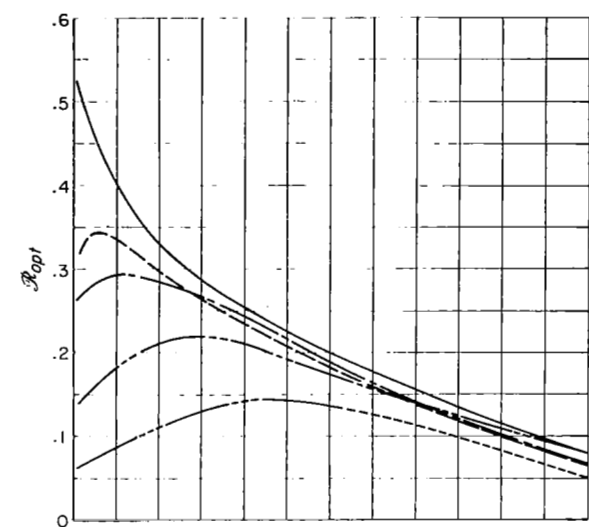


Figure 38. - Significant characteristics obtained from correlation of velocity fluctuations with wall-pressure fluctuations.



(b) Transducer ZS;  $\eta \approx 0$ .

Figure 38. - Continued. Significant characteristics obtained from correlation of velocity fluctuations with wall-pressure fluctuations.



(c) Transducer ZS;  $\xi \approx 0$ .

Figure 38. - Continued. Significant characteristics obtained from correlation of velocity fluctuations with wall-pressure fluctuations.

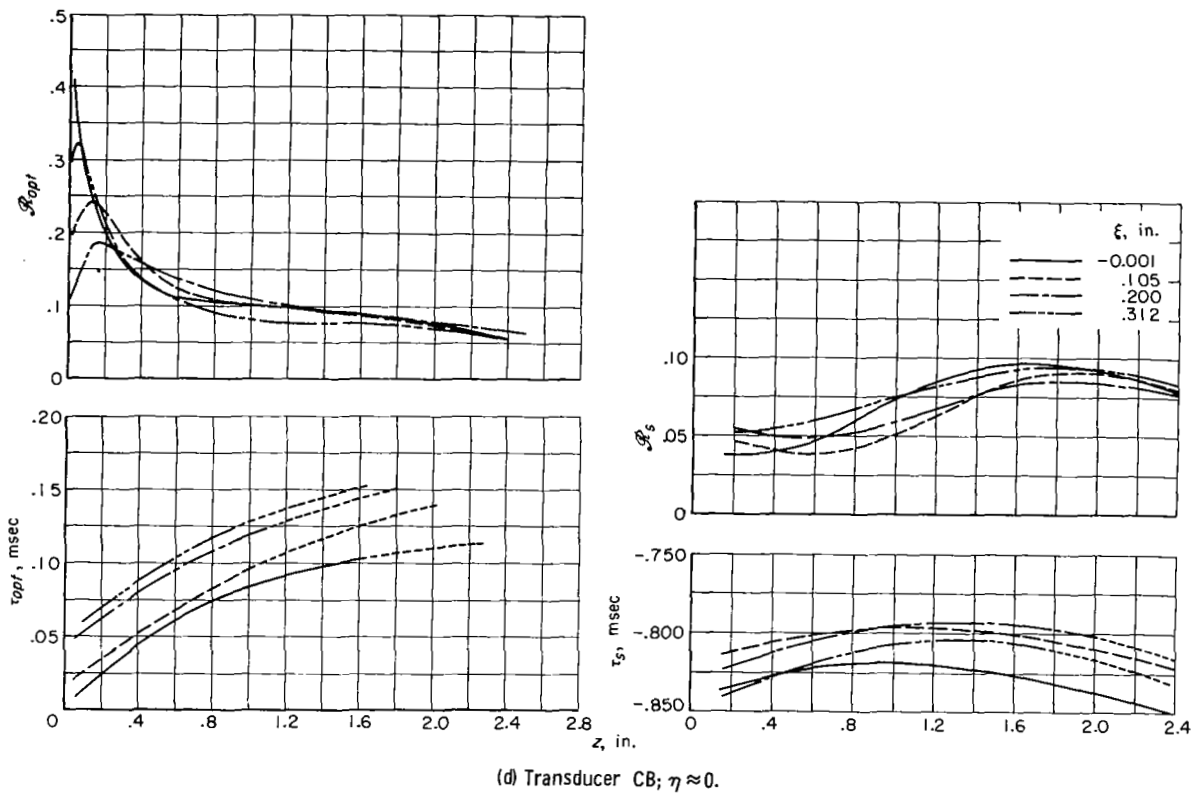


Figure 38. - Concluded. Significant characteristics obtained from correlation of velocity fluctuations with wall-pressure fluctuations.

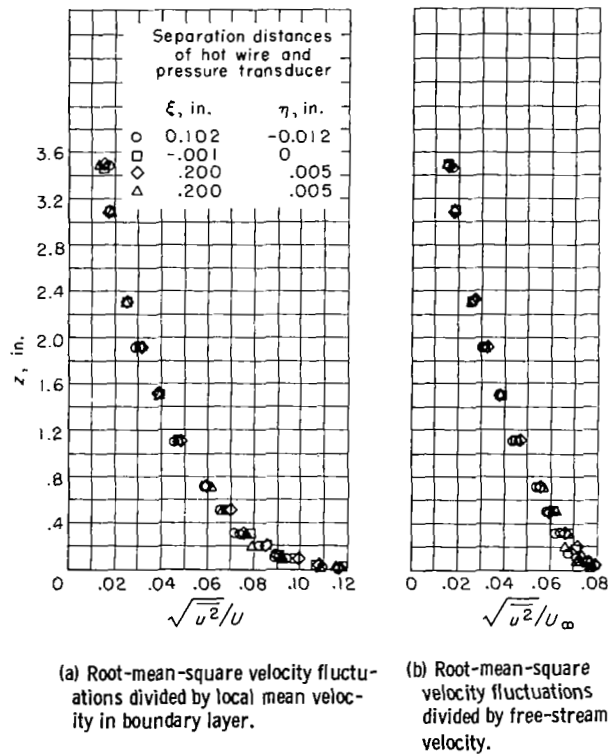


Figure 39. - Typical profiles of turbulent longitudinal velocities in boundary layer (measured during surveys for correlation data).

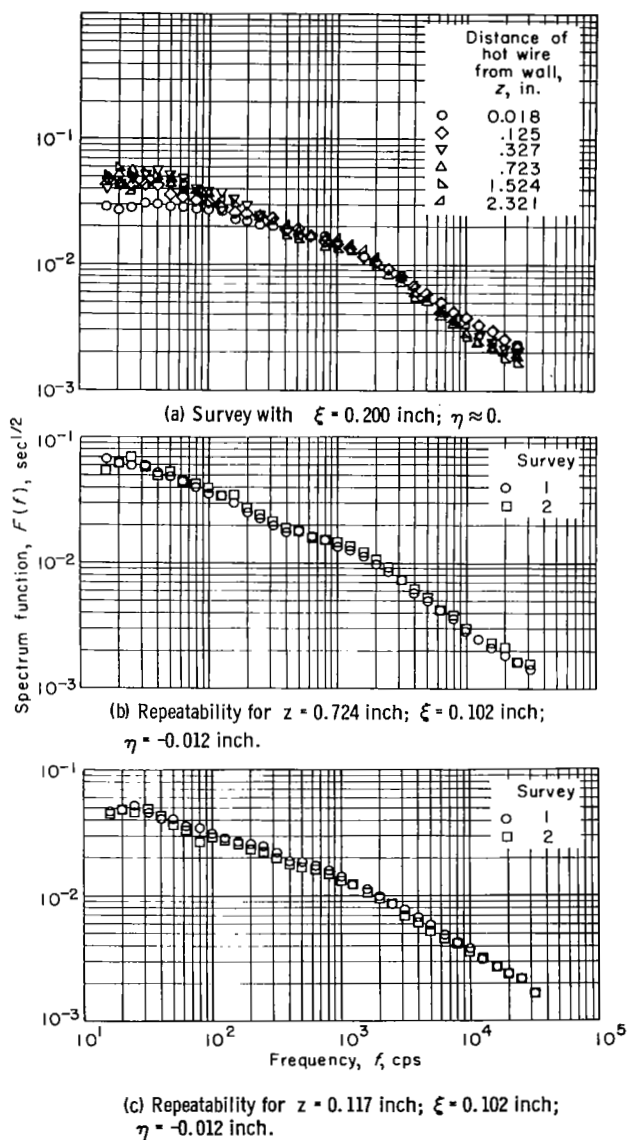


Figure 40. - Typical spectra of longitudinal turbulent fluctuations (measured during surveys for correlation data).

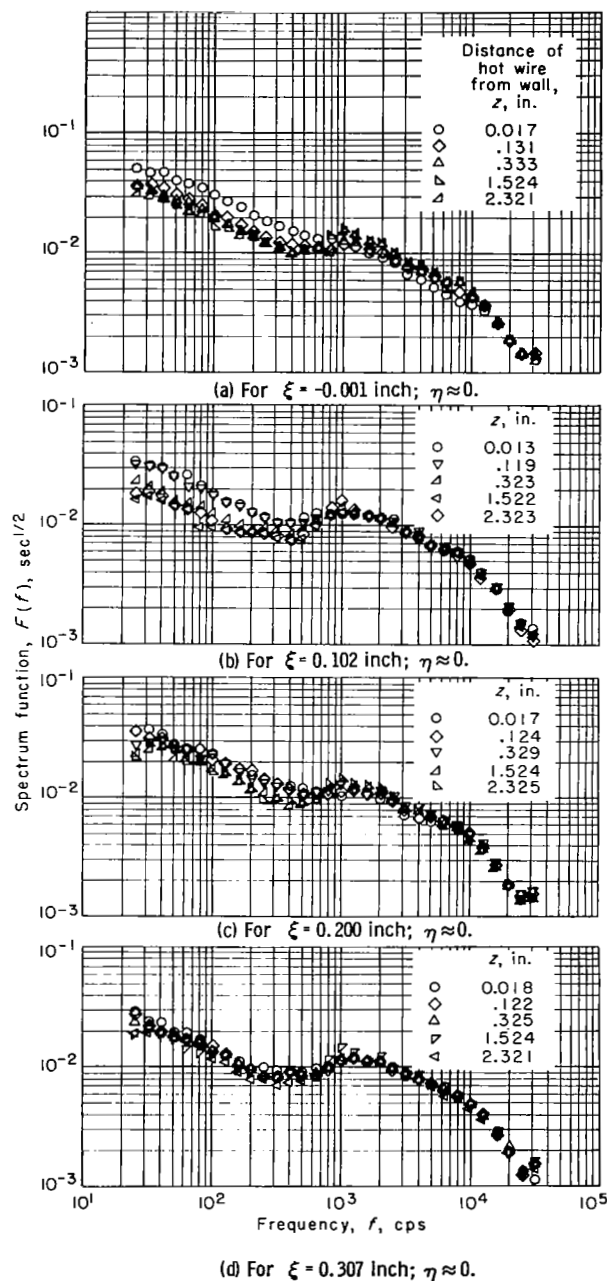


Figure 41. - Spectra of wall-pressure fluctuations, measured by transducer ZS during surveys for correlation data and showing interference effect of hot-wire probe.

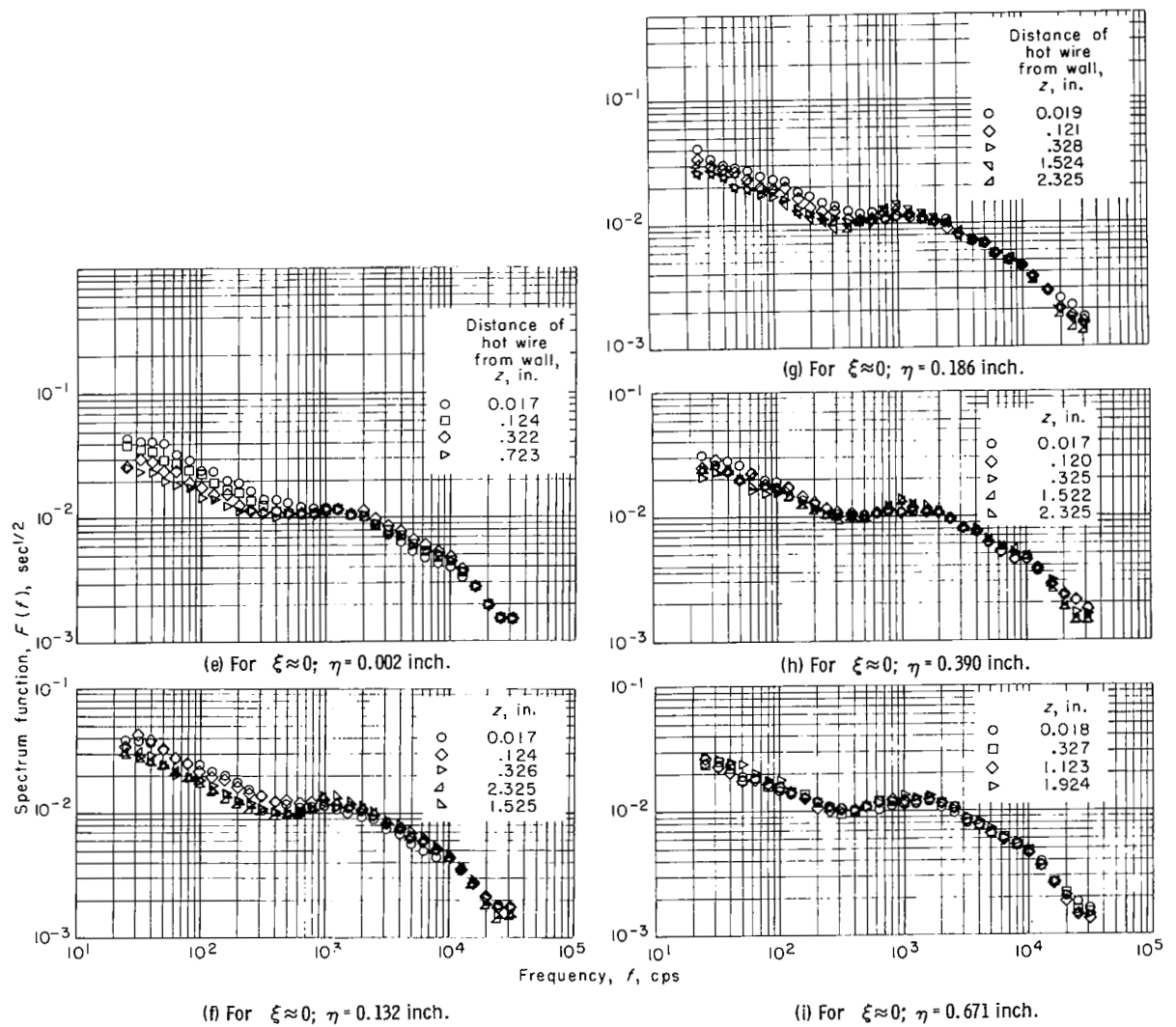


Figure 41. - Concluded. Spectra of wall-pressure fluctuations, measured by transducer ZS during surveys for correlation data and showing interference effect of hot-wire probe.

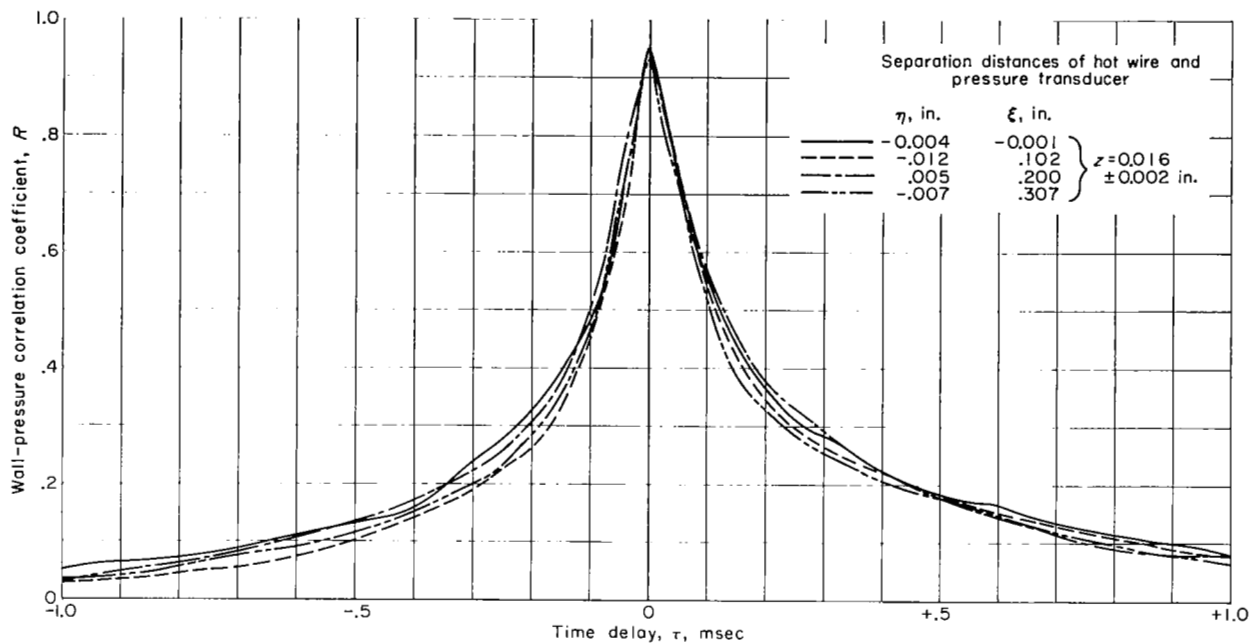


Figure 42. - Typical autocorrelation curves for velocity fluctuations, measured during surveys for obtaining their correlation with wall-pressure fluctuations.

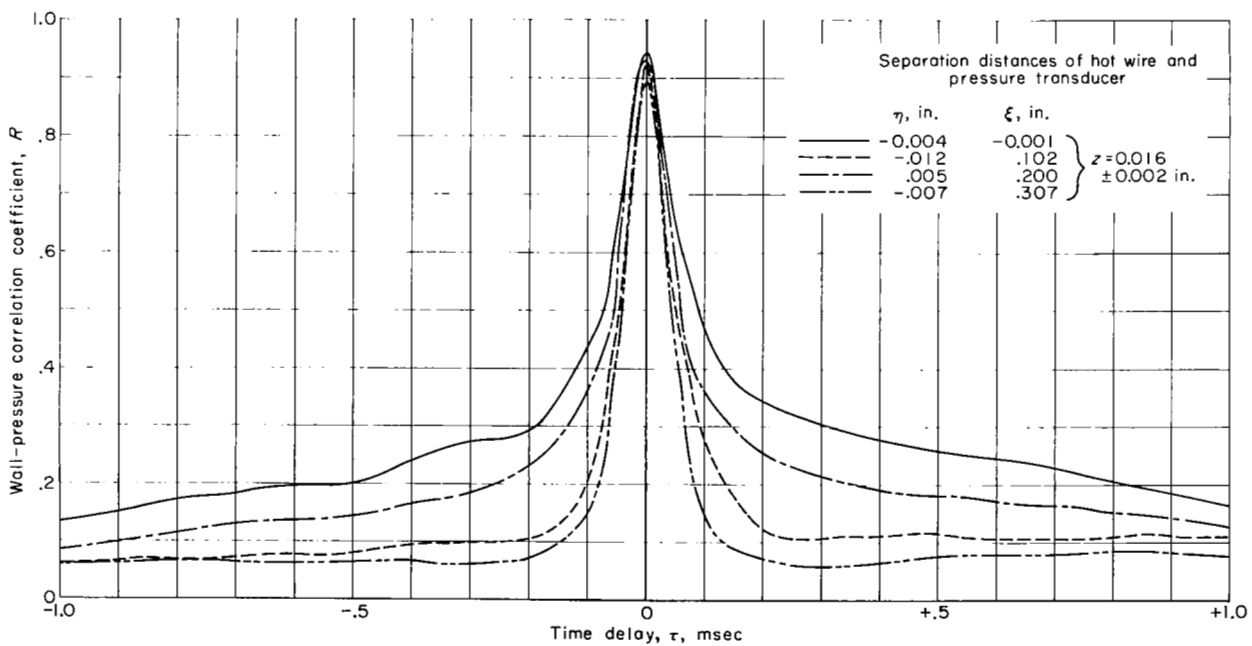


Figure 43. - Typical autocorrelation curves for wall-pressure fluctuations, measured during surveys for obtaining their correlation with velocity fluctuations.

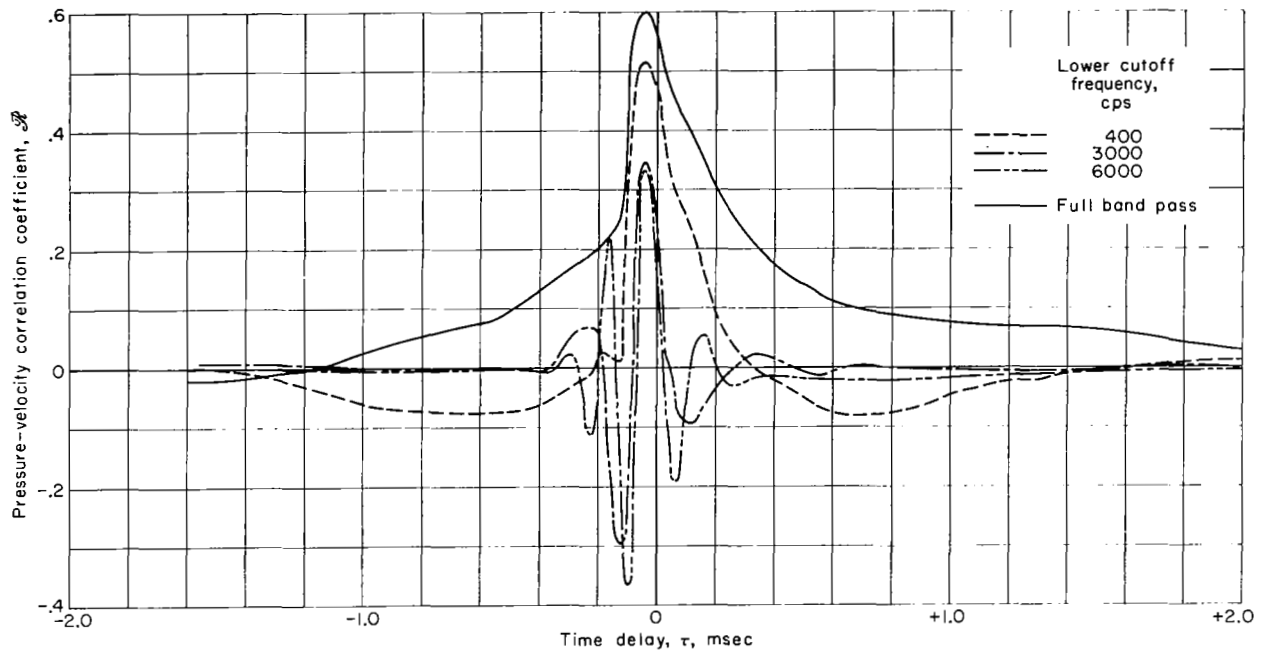


Figure 44. - Effect of high-pass-band filtering on correlation of velocity fluctuations with wall-pressure fluctuations, measured by transducer CB.  $z = 0.012$  inch;  $\xi \approx \eta \approx 0$ .

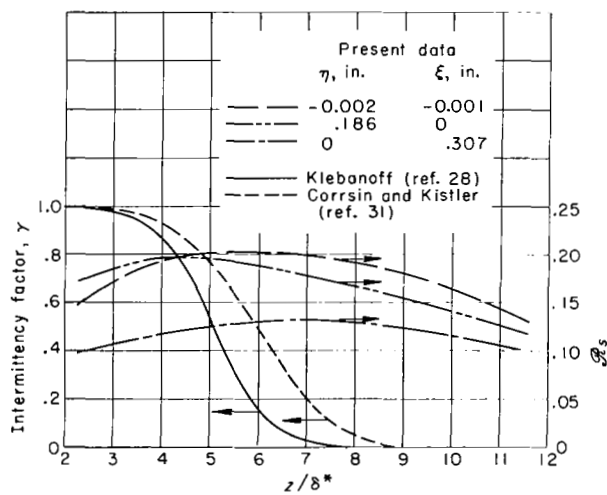


Figure 45. - Comparison of  $\mathcal{R}_s$  with the intermittency data of Klebanoff (ref. 28) and Corrsin and Kistler (ref. 31).